SYNTHESIS OF POROUS POLYSACCHARIDE PARTICLE AND THEIR ADSORPTION PROPERTIES

（ポーラス構造を持つ多糖類微粒子の合成と吸着特性）

A Thesis submitted to
The Chemical Engineering Program
Graduate School of Advanced Science and Engineering
Hiroshima University

Presented by

NGUYEN TRI TUE

In Partial Fulfillment of the Requirements for the Degree of
Doctor of Engineering

Hiroshima University
September 2024

Approved by
Professor Takashi Ogi
Adviser

SYNTHESIS OF POROUS POLYSACCHARIDE PARTICLE AND THEIR ADSORPTION PROPERTIES

Nguyen Tri Tue

September 2024

SYNTHESIS OF POROUS POLYSACCHARIDE PARTICLE AND THEIR ADSORPTION PROPERTIES

Abstract

This dissertation presents a comprehensive study on the development of porous pectin particles for drug delivery applications, encompassing the synthesis method, characterization, and functional evaluation across three research papers. Pectin, a natural polymer, was utilized to fabricate meso-/macroporous particles through a template-assisted spray-drying method, followed by chemical etching. These particles showcased significantly higher surface areas and improved drug release rates compared to nonporous counterparts, demonstrating their potential as efficient drug delivery systems. This dissertation is divided into five chapters, the content of which is briefly described below.

Chapter 1 introduced the recent advancements and the motivation of developments in nanostructured particles, particularly those with porous structures. These particles, with their large surface area and high porosity, offer enhanced performance in various applications including catalysis, adsorption, and drug delivery. The synthesis of porous pectin particles using a template-assisted spray drying method represents a novel approach in this field, addressing the need for efficient and environmentally friendly drug delivery systems.

Chapter 2 focused on the preparation of porous pectin. Porous pectin particles were developed using poly(methyl methacrylate) (PMMA) or calcium carbonate ($CaCO_3$) as templates. It highlighted the control over pore size and surface area through the variation of template concentration, showcasing a significant increase in specific surface area compared to nonporous counterparts. This study highlights the potential of porous pectin particles in applications requiring high adsorption efficiency.

Building on the foundation laid by the previous chapter, Chapter 3 focused on the protein adsorption capabilities of porous pectin particles. The particles exhibited rapid and high-capacity adsorption of lysozyme, a model protein, due to their macroporous structure and interconnected pore networks. The research underscores the importance of pore size and surface area in optimizing protein adsorption, positioning porous pectin particles as promising materials for biomedical applications.

Chapter 4 explored the use of porous pectin particles as a drug delivery system, with indomethacin as the model drug. The porous structure facilitated a faster drug

release rate compared to nonporous particles, demonstrating the potential of porous pectin particles in targeted drug delivery, especially to the colon. The study provided insights into the mechanisms of drug release from porous particles and highlighted the versatility of pectin as a biomaterial for pharmaceutical applications.

Chapter 5 summarized the synthesis of porous pectin particles represents a significant advancement in the use of nanostructured particles for adsorption and drug delivery applications. Through innovative synthesis methods and the utilization of natural polymers, these studies contribute to the development of efficient, sustainable, and biocompatible materials. Future research could explore the application of porous pectin particles across a broader range of substances and conditions, further enhancing their applicability in various fields.

Contents

Listing of figures

List of Tables

Acknowledgments

I would like to express our deep gratitude to Professor Takashi Ogi for his enthusiastic guidance in advancing this research. It was a long period of five years, and I am fortunate to have learned under Professor Takashi Ogi. I am deeply grateful to Assistant Professor Tomoyuki Hirano for his unwavering dedication and invaluable guidance over the past five years. As a teacher, friend, and mentor, he has profoundly shaped my personal and professional growth, and I cannot thank him enough. I would also like to express our sincere gratitude to Professor Satoshi Nakai, and Professor Atsushi Ikeda for their appropriate advice. I would like to express our sincere appreciation to Michiyo Tachibana, Junko Amazaki for their support. I am deeply grateful to Masato Miyauchi and the other researchers from Japan Tobacco Inc. for their excellent cooperation in investigating the joint research.

I would like to express my sincere gratitude to Annie Mufyda Rahmatika for her guidance and discussion as a senior. It is no exaggeration to say that my research was following Annie Mufyda Rahmatika. I would also like to thank all the seniors who have guided me so far. I would like to thank Yusuke Kitou and Youhei Toyoda, who supported and be a good friend when I came to join Ogi laboratory. I am deeply grateful to Shuhei Nakakura, Kazuki Kamikubo, Jun Kikkawa, Cao Le Anh Kiet, Wang Xinming, Takama Tsuboi, Yasuhiko Kitamoto, Shogo Kaseda, Eka Lutfi Septiani, Ryosuke Narui, Shunki Yamashita, Kazuki Yamamoto, Kodai Fusatani, Delyana Ratnasari, Duhaul Biqal Kautsar, Ridha Nurul Chamida, Ai Ando, Shota Imaoka, Naho Tokitsu, Hirofumi Seo, Cao Le Anh Khoa, and all other members for their company on my route.

During this period, Nur Syakirah Nabilah Saipul Bahri, despite being a “mischievous” junior, has helped me realize many lessons not just in research but also in life. Their playful spirit and insightful perspectives have added depth to my understanding and enriched my personal growth. I am profoundly thankful to Le Hoai Phong, Ho Thi Thanh Nguyen, and Pham Van Tung for their unwavering companionship and solidarity during the most delicate and challenging moments of this journey. Your support has not only comforted me but has also been a cornerstone of my resilience. In addition, I appreciate all of my friends in Sansiation Group for their encouragement when I meet challenges. I would like to express my deep gratitude to my parents and older sister for their long-term support. I wish you all a bright and successful journey ahead.

Thank you to Hiroshima University Graduate School Research Fellowship, Hosokawa Powder Technology Foundation for supporting my research funds and daily living expenses.

I would like to express my sincere gratitude and acknowledgment to everyone who has cooperated so far to complete this journey.

Tue Tri Nguyen
Hiroshima, Japan
June 2024

1

Overview of Porous Particles Prepared by Spray Drying

1.1 PROGRESS ON NANOSTRUCTURED PARTICLES SYNTHESIS BY SPRAY DRYING

1.1.1 Introduction of spray drying

Spray drying is a pivotal technology for producing powdered materials by instantaneously drying a liquid spray in a hot air flow. Its origins trace back to 1872, when Samuel Percy first patented a method related to this technology, underlining its long-standing significance in material processing. Over the years, spray drying has evolved significantly, initially aimed at enhancing the handling and preservation qualities of food products, such as powdered milk, soap, and coffee, by reducing their moisture content. This method quickly gained traction in Japan with the production of powdered milk in 1924 by the Hokkaido Condensed Milk Company, marking a dramatic improvement in production efficiency and quality of powdered milk in the country (Figure 1.1a).

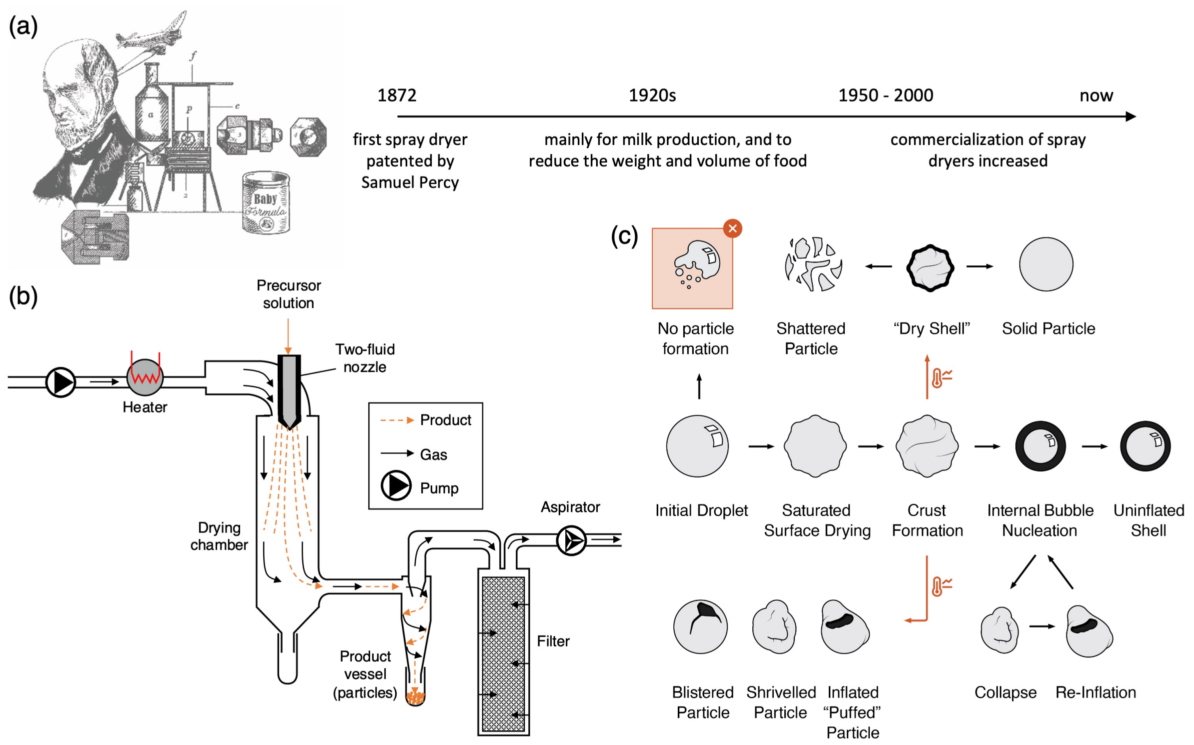

Figure 1.1: (a) History of spray drying. (b) An open-cycle spray dryer illustrates the main phases of atomization, drying, and collection. (c) Particle designs via spray drying

The process involves several key steps: atomization of the feed liquid into a spray, contact of the spray with hot air leading to rapid solvent evaporation, and collection of the dry particles. In detail, the methodology of spray drying is depicted schematically in Figure 1.1b, initiating with the atomization of a liquid feedstock, either a solution or suspension, into a fine spray within a drying chamber. This spray is then exposed to a substantial volume of hot drying gas, consisting of either nitrogen or dry air contingent on the solvent. The result is the rapid evaporation of the liquid phase, culminating in the formation of solid particulates. These particulates are subsequently extracted from the gas stream, predominantly through cyclonic separation techniques.[1] During the process, evaporative cooling ensures that the atomized droplets remain at a comparatively low temperature throughout the majority of their drying trajectory, thereby rendering this technique exceptionally suitable for the fabrication of powders sensitive to heat.[2]

The core advantage of spray drying lies in its ability to produce powders with a wide range of properties by manipulating processing conditions and formulations. These powders can have tailored particle sizes, morphologies, and compositions, catering to specific application requirements. For instance as shown in Figure 1.1c, the particle size distribution is primarily determined during the atomization step and can be controlled by adjusting the atomizer design and operating conditions. The morphology of the particles, such as their shape and surface characteristics, can be influenced by the feed composition and drying conditions. The composition of the final product can also be varied by using different feed formulations, allowing for the production of composite materials, encapsulated products, or functionalized particles.

1.1.2 Types of nanostructured particles and their application

The synthesis of nanostructured particles via spray drying has evolved significantly, with advancements enabling the tailored fabrication of aggregates, porous, hollow, and core-shell structures. This diversity in achievable morphologies underpins the technology's broad applicability across various scientific domains, from pharmaceuticals to materials science and energy storage. The following sections detail these structures, highlighting recent developments and exemplifying their utility in high-impact applications.

Nano-aggregates consist of primary particles that are physically bound together, offering increased particle stability and altered physicochemical properties compared to individual nanoparticles. The formation of aggregates via spray drying is influenced by parameters such as solvent choice, feed concentration, and drying conditions. A notable study by Nani and Krishnaswamy focused on the synthesis of acid whey/millet flour aggregates for food industry applications.[3] These aggregates demonstrate enhanced functionality, such as improved solubility and nutrient delivery, showcasing the potential of spray-dried aggregates in creating value-added products from industry waste, which is shown in Figure 1.2. Porous nanostructures synthesized through spray drying exhibit high surface areas and tunable pore sizes, making them particularly suited for applications requiring adsorption, catalysis, drug delivery, and filtration. The creation of such structures often involves the use of sacrificial templates that

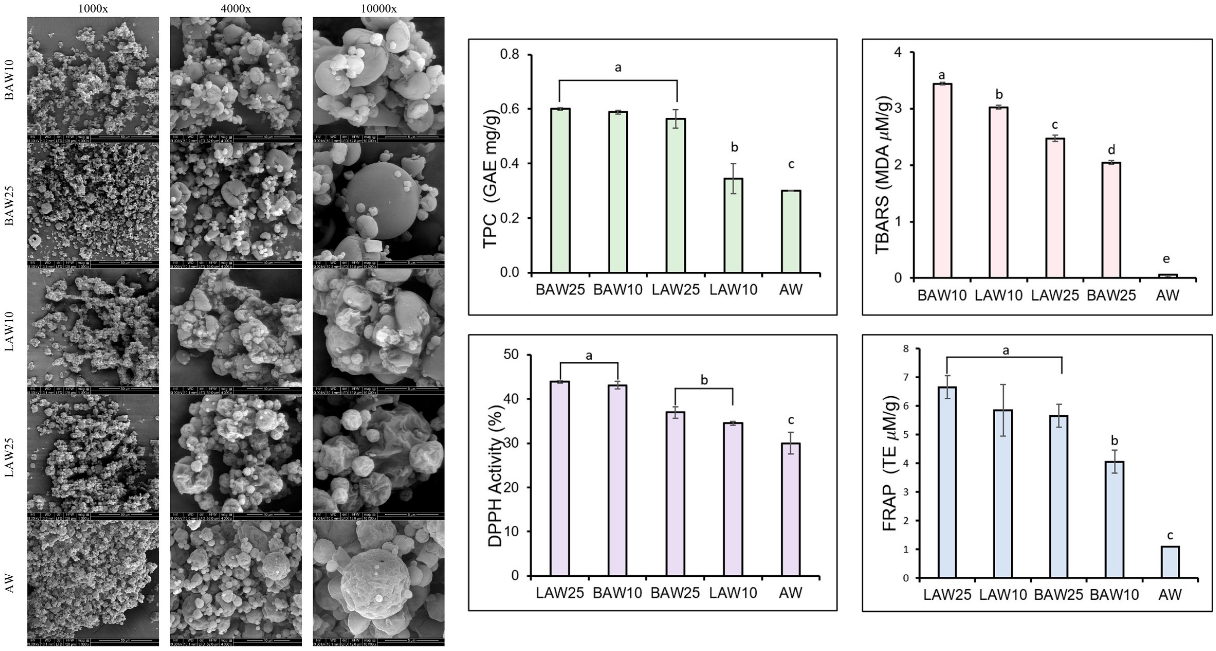

Figure 1.2: SEM images of spray-dried acid whey (AW) and different AW millet (AWM) powders at 1000×, 4000×, and 10000× magnification; and their antioxidant activity. Adapted from [3].

are removed post-drying, leaving behind voids. An exemplary application is in the development of carboxylated cellulose nanocrystal (cCNC) microbeads for wastewater treatment, where the porous structure facilitates the adsorption and removal of organic dyes in Figure 1.3.[4] This approach underscores the utility of spray drying in environmental remediation, leveraging the inherent properties of nanostructured porous particles for efficient pollutant capture.

Also, Hu et al. developed where Si/carboxymethyl chitosan (CMCS) composite spherical particles in Figure 1.4 as high-performance anodes for lithium-ion batteries.[5] These particles, synthesized through spray drying, demonstrated enhanced electrochemical performance attributed to their engineered porous structure, highlighting the role of porosity in facilitating ion transport and electrode stability. Hollow nanostructures offer unique advantages, including low density and high surface area, desirable for catalysis, drug delivery, and as fillers in composite materials. Spray drying enables the synthesis of hollow particles by careful control of the solvent evaporation rate and the use of core materials that can be leached out or decomposed after particle formation. The synthesis of hollow microspheres by Zhang et al., utilizing anatase/rutile/hematite heterojunctions, serves as a prime example.[6] These spray-dried particles in Figure 1.5

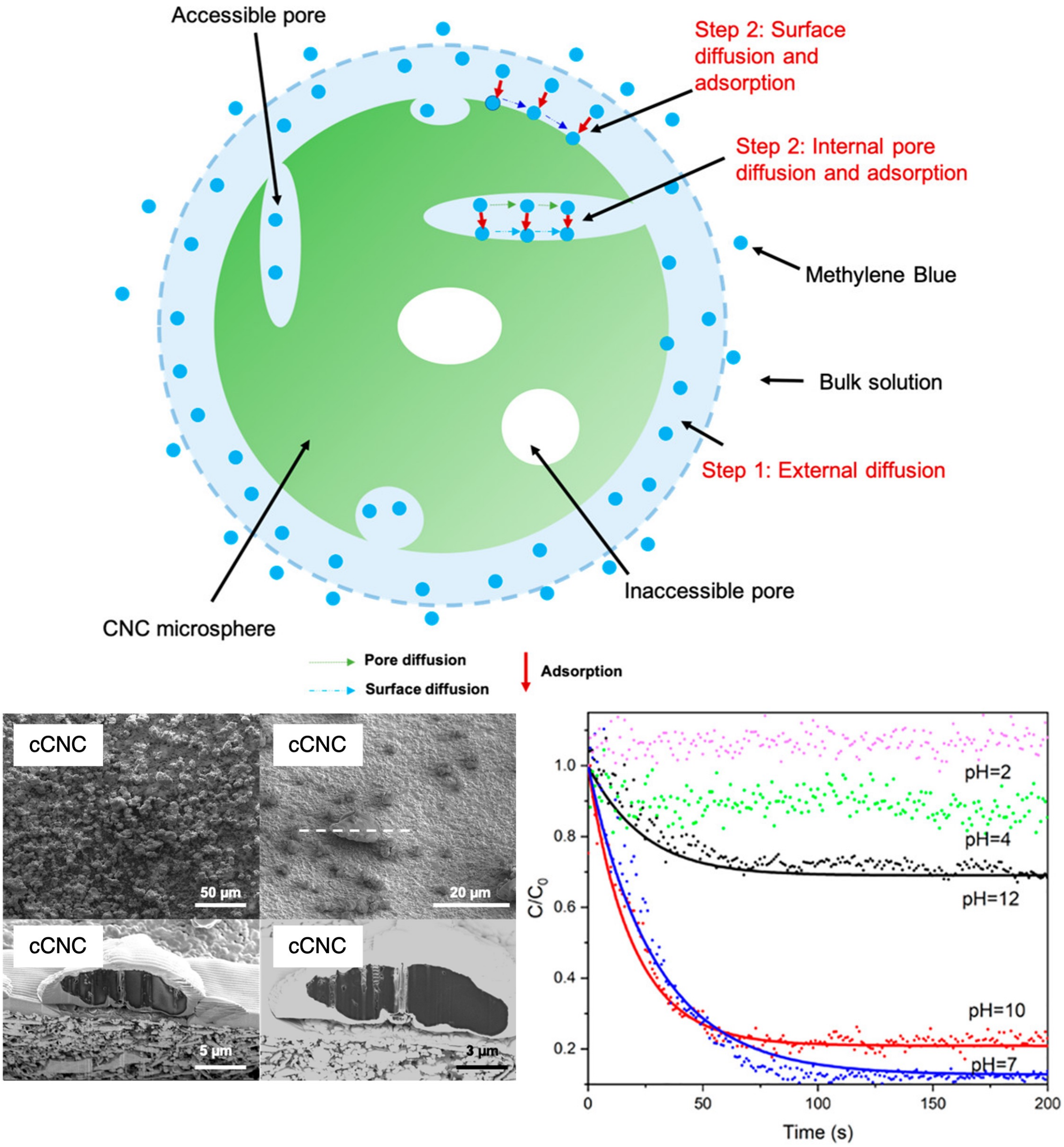

Figure 1.3: SEM and FIB cross-sectional images of cCNC; illustration of external and internal diffusion for methylene blue (MB) transport at the surface and within a cCNC microbead; MB dye uptake by cCNC microbeads at different pH fitted to film–pore diffusion model based on a Langmuir isotherm. Adapted from [4].

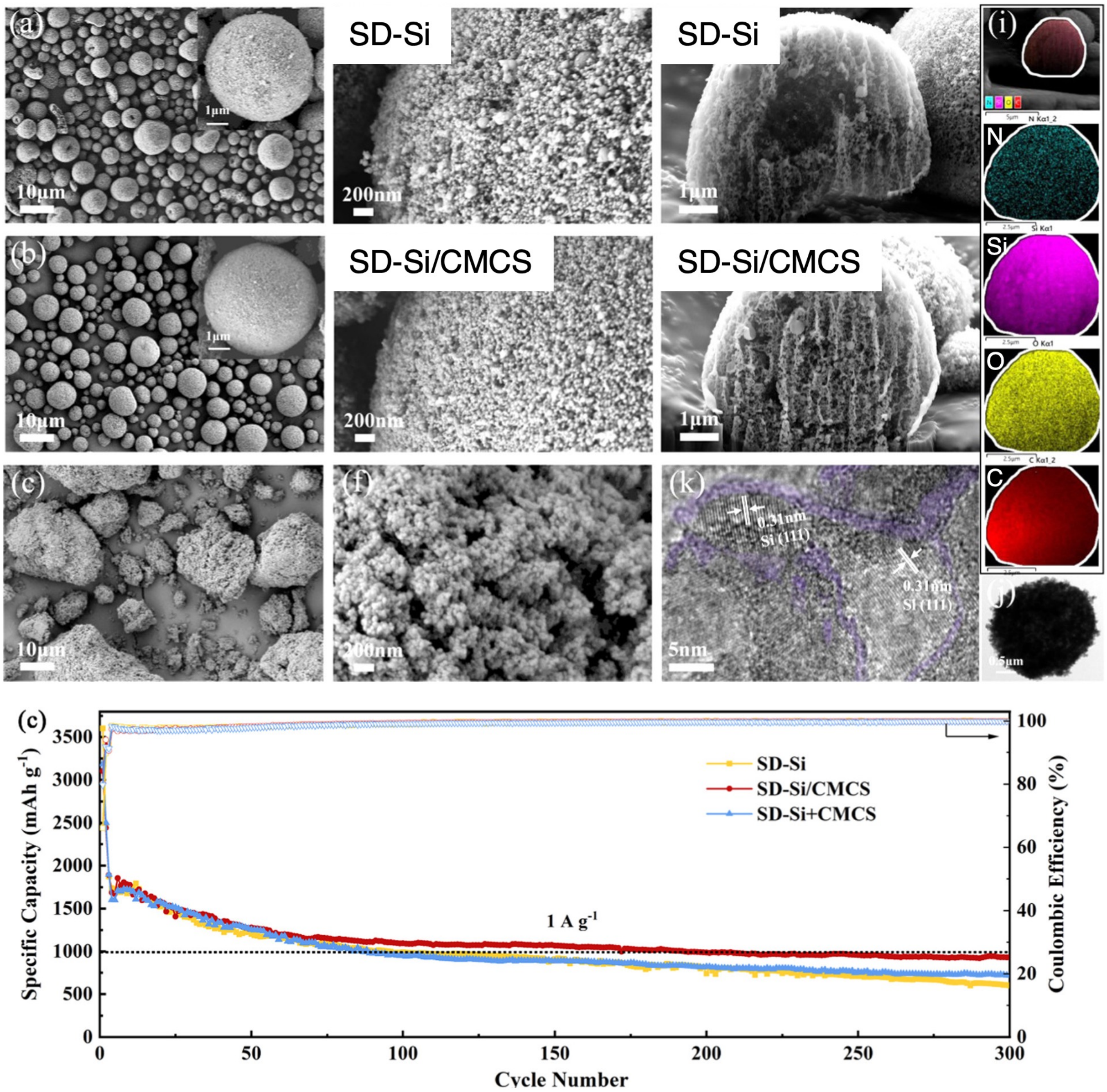

Figure 1.4: SEM, FIB cross-sectional, and high-resolution TEM images of SD-Si, SD-Si/CMCS, and M-Si/CMCS; cross-sectional elemental mapping of SD-Si/CMCS microspheres: N (blue), Si (purple), O (yellow), and C (red) elements. Adapted from [5].

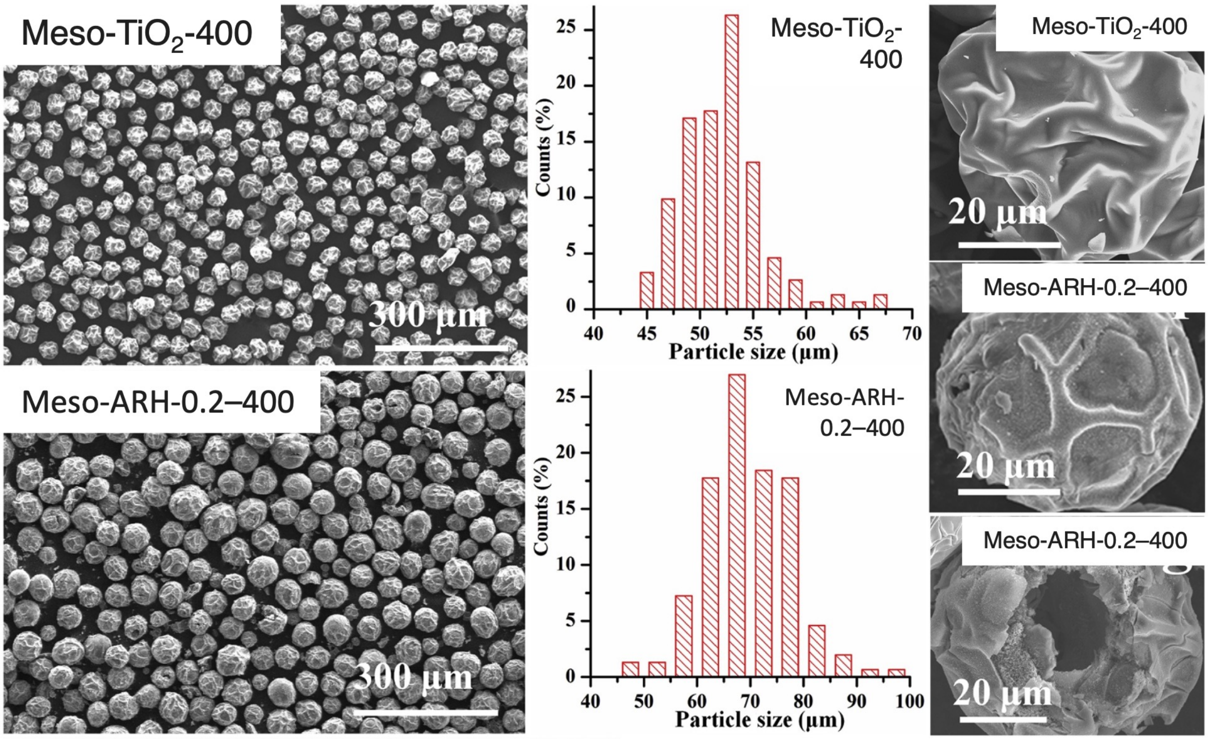

Figure 1.5: SEM images, and particle size distributions of Meso-TiO_2-400 and Meso-ARH-0.2–400. Adapted from [6].

exhibited superior photocatalytic performance for organic dye removal, leveraging the hollow structure to increase surface reactivity and light absorption efficiency. Core-shell structures feature a distinct core material encapsulated within a shell of another material, providing a means to combine different material properties into a single particle. This structure is advantageous for applications requiring controlled interaction between the core and its environment, such as in catalysis or targeted drug delivery. Spray drying facilitates the synthesis of core-shell particles by co-drying solutions containing both core and shell material precursors. The research by An et al. on Si/C@C porous spherical core-shell microspheres in Figure 1.6 illustrates the profound potential of these structures in energy storage applications.[7] Created through spray drying followed by carbon coating, these particles address silicon's volume expansion issue in lithium-ion batteries, offering improved lifecycle and performance. The core-shell design enhances electrical conductivity and provides mechanical support, underlining the method's capability to tailor electrochemical properties through nanostructural engineering. Table 1.1 summarize some nanostructured particles and their applications in recent years.

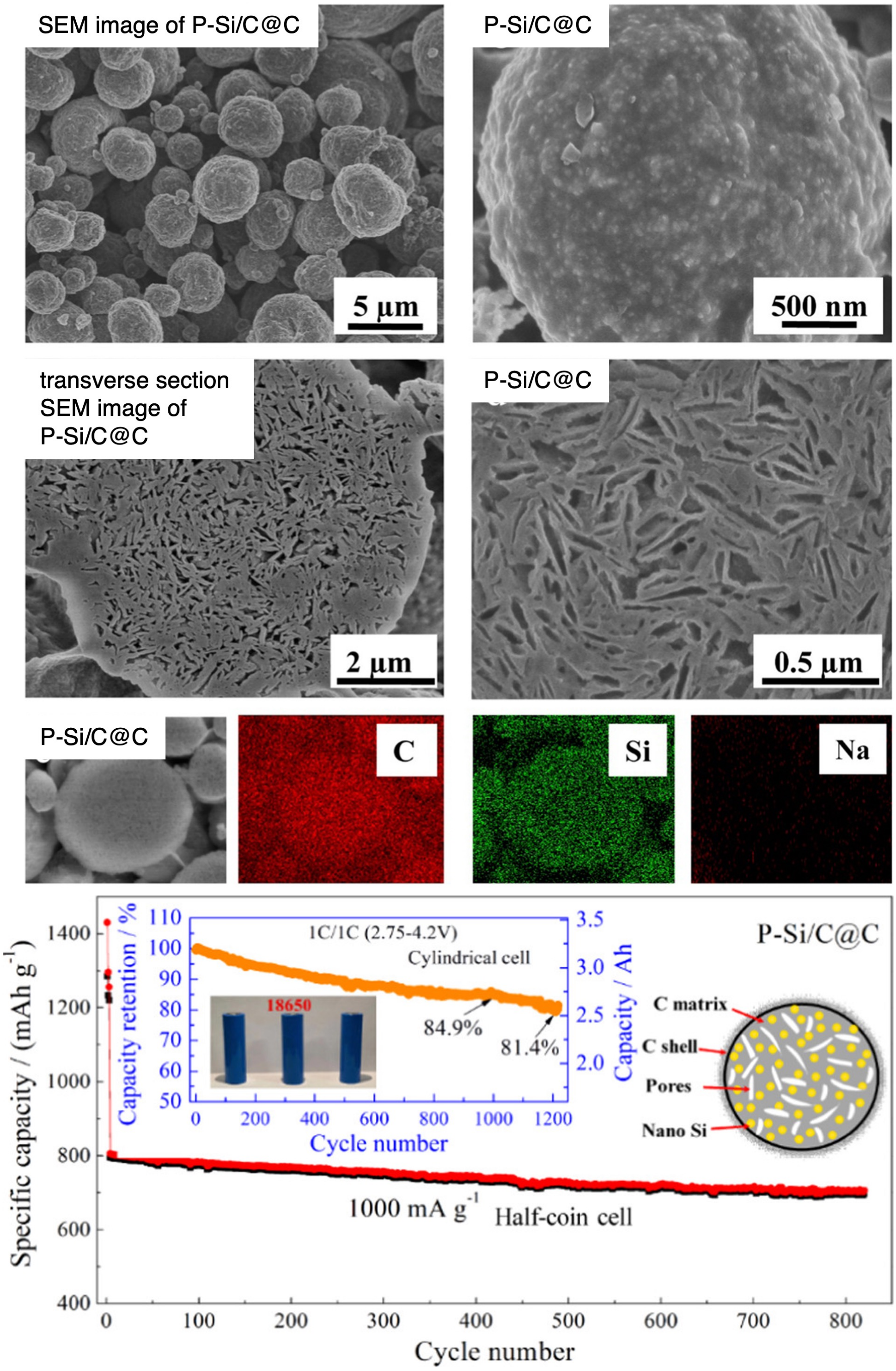

Figure 1.6: SEM image and magnified SEM image of P-Si/C@C; transverse section SEM image of P-Si/C@C; and the corresponding elemental mapping images; cycle stability with capacity retentions of 84.9 and 81.4% after 1000 and 1200 cycles at 1C. Adapted from [7].

Table 1.1: Nanostructured particles synthesized by spray drying and their application.

Material	Structure	Application	Reference
Lactoferrin and glycomacropeptide nanohydrogels	Spherical with agglomeration	Food (storage)	[8]
Gelatin, alginate, limonene, succinic acid	Microencapsulation	Food (preventing volatile loss and degradation)	[9]
Sodium alginate, $CaCO_3$, phytase (common enzyme in animal feed industry), succinic acid, and ammonia	Spherical relatively rough surfaces	Food (animal food stock)	[10]
Acid whey/millet flour	Aggregates	Food (Industry waste)	[11]
Konjac glucomannan, isoniazid, and rifabutin	Spherical	Antitubercular drug carriers in lung tuberculosis therapy	[12]
Chitosan - graphene oxide	Wrinkle, spherical	Treatment of solid cancer, in particular prostate cancer	[13]
Silica nanoparticles-sodium alginate loaded with doxorubicin	Doughnut shape	Drug carriers in cancer treatment	[14]
Indomethacin-loaded polymeric micelles	Microencapsulation	Intestinal drug	[15]
Si/C@C	Porous spherical core-shell	Anode for lithium-ion battery	[7]
Si/carboxymethyl chitosan composite	Spherical	Anode for lithium-ion battery	[5]
SiOx@C@CoO composite	Sponge-like	Anode for lithium-ion battery	[15]
Si/SiC/C composite	Spherical	Anode for lithium-ion battery	[16]
Si/C	Raspberry-like yolk-shell	Anode for lithium-ion battery	[17]
$V_2(PO_4)O$/C@CNT	Hollow spherical core-shell	Anode for lithium-ion battery	[18]
V_2O_5/LiV_3O_8 coated $LiNi_{0.88}Co_{0.07}Al_{0.05}O_2$	Spherical	Cathode for lithium-ion battery	[19]
$LiNi_{0.5}Mn_{1.5}O_4$	Octahedral	Cathode for lithium-ion battery	[20]
$LiNi_{0.8}Co_{0.1}Mn_{0.1}O_2$	Spherical	Cathode for lithium-ion battery	[21]
$LiFe_{0.25}Mn_{0.75}PO_4$/C@reduced graphene oxide (rGO)	Spherical	Cathode for lithium-ion battery	[22]
Ti-doped $LiFePO_4$/C	Spherical	Cathode for lithium-ion battery	[23]
$LiNi_{0.8}Co_{0.1}Mn_{0.1}O_2$	Spherical	Cathode for lithium-ion battery	[24]
Sulfur-doped hollow mesoporous carbon	Mesoporous-shell hollow	Anode for potassium-ion battery	[25]
Carbon-matrixed KVP_2O_7	Hollow wrinkled	Cathode for potassium-ion battery	[26]
Br-doped $Na_3V_2(PO_4)_2F_3$/C	Porous spherical	Cathode for sodium-ion battery	[27]
Polyetherimide/$LaNi_5$ composite	Wrinkled (some spherical)	Hydrogen storage	[28]
Cyanamide@graphene oxide (GO) composite	Porous spherical	Electrode for electrical double-layer capacitors	[29]
Polyaniline nanofibers/reduced graphene oxide (rGO)/cerium oxide nanorods composite	Porous	Electrodes for supercapacitor	[30]
Reduced graphene oxide (rGO)/activated carbon	Wrinkled core-shell	Electrodes for supercapacitor	[31]
CuO@γ-Al_2O_3	Rough and wrinkled	Organic pollutants removal from wastewater	[32]
Carboxylated cellulose nanocrystals	Dense agglomerate	Organic dyes removal from wastewater	[4]
Anatase/rutile (TiO_2)/hematite (Fe_2O_3) heterojunctions	Wrinkled	Organic dyes removal from wastewater	[6]
Ni/SiO_2 and Ni/γ-Al_2O_3	Spherical	CO_2 methanation	[33]

The development of nanostructured particles through spray drying is marked by significant scientific ingenuity, allowing for precise control over particle morphology, structure, and functional properties. From aggregates that enhance the physical stability of particulate systems to porous structures that maximize surface area for catalysis and adsorption, the versatility of spray drying caters to a wide range of high-impact applications. Hollow and core-shell structures further exemplify the method's adaptability, enabling the design of advanced materials with tailored properties for energy storage, environmental remediation, and biomedicine. These advancements underscore the pivotal role of spray drying in the current landscape of materials science and nanotechnology, highlighting its potential to drive future innovations across diverse scientific domains.

1.2 INTRODUCTION OF POROUS PARTICLES

1.2.1 Definition of porous particles

Porous particles are one type of nanostructured particles, which are low-density materials characterized by their open or closed pore structures affording them an extensive surface area for interaction.[34] Emerging in the twentieth century, these materials have found wide-ranging applications across various sectors. The International Union of Pure and Applied Chemistry (IUPAC) categorizes pores based on their size into three primary groups in Figure 1.7a: micropores, which are less than 2 nm in diameter; mesopores, ranging from 2 to 50 nm; and macropores, exceeding 50 nm. The concept of nanoporosity, while not precisely defined, generally refers to pores within the nanometer scale, approximately 0.1 to 100 nm, encompassing all three IUPAC-defined pore size categories.[35] Pores can be further differentiated based on their geometry and connectivity. Open pores are those that are accessible from the material's exterior (Figure 1.7b-e), including blind pores that are open at only one end (Figure 1.7c, e, h, (f)) and through pores that are accessible from two or more ends (Figure 1.7b and d). In contrast, closed pores are isolated from the external environment, preventing mass exchange. This isolation may be due to the pore being entirely encapsulated within the material (Figure 1.7g) or the pore opening being too small for molecules to pass through (Figure 1.7f). The size of these pores can be precisely controlled through the conditions under which the porous particles are prepared, a factor that significantly influences their characteristics. In comparison to standard particles, porous particles exhibit several unique attributes, including a large surface area, high porosity, a uniform and adjustable pore structure, and well-defined surface properties both internally and externally.[36,37]

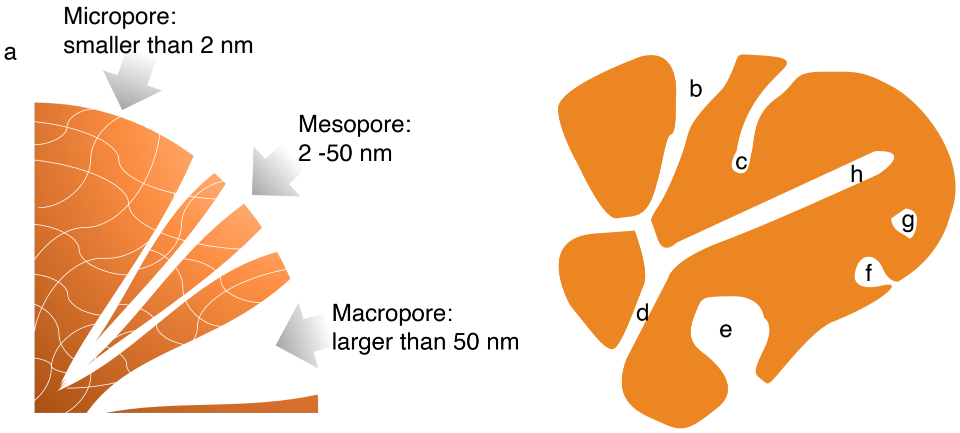

Figure 1.7: (a) Pore nomenclature according to IUPAC. Schematic drawing of different types of pores in two dimensions. (b) open pore with a ratio between a pore's body and its throat smaller than 1, (c) blind open cylindrical pore, (d) open-through cylindrical pore, (e) blind open pore with a ratio between a pore's body and its throat larger than 1, (f) closed pore with an opening that is smaller than the drug molecule, making it practically impenetrable, (g) closed isolated pore, (h) blind open cylindrical pore.

1.2.2 Approaches to prepare porous particles

Porous particles are engineered from base materials through the incorporation and subsequent removal of specific substances or the application of particular techniques to create voids within the material structure. The methodologies employed for the fabrication of porous particles are varied and multifaceted, encompassing several distinct approaches as elucidated below.

The primary and most widely recognized strategy involves the incorporation of porogens or templating agents into the base material. This is followed by their removal, which results in the formation of pores (Figure 1.8a). Specifically, porogens typically induce pore formation through gas generation or volatilization during the fabrication process. For instance, Bae et al. utilized hydrogen peroxide as a porogen to produce porous poly(lactic-co-glycolic acid) microspheres, where an enzymatic reaction with catalase yielded oxygen bubbles, thereby creating internal pores.[38] The physicochemical characteristics of the porogen significantly influence the final microsphere's pore size and distribution. Alternatively, templating agents are removed post-fabrication through solvent washing or heat treatment, offering a different mechanism for pore creation. Various materials, ranging from food-grade acids to polymers and inorganic salts, serve as templates, each facilitating distinct pore sizes and structures. Despite their effectiveness, the necessity for post-fabrication removal of porogens or templates introduces complexity and potential scalability and safety challenges. A second approach eschews the use of porogens or templates altogether. Amphiphilic polymers were used to fabricate porous microspheres with a narrow size distribution utilizing a double emulsion-premix membrane emulsification technique.[39,40] This method inherently forms pores without additional agents, governed by the evaporation of water absorbed by hydrophilic segments and the rapid solvent evaporation (Figure 1.8b). The synthesis of porous particles, particularly silicon-based varieties, represents a third methodology. Techniques such as electrochemical dissolution of silicon in HF-based solutions or the reaction of silica sources with surfactants to form mesoporous silica nanoparticles illustrate the synthesis-based approach.[41] These methods allow for precise control over porosity and pore structure through the reaction conditions and the removal of structure-directing agents. Beyond these primary strategies, specialized methods exist for fabricating specific types of porous particles, such as porous $CaCO_3$ through re-precipitation or porous starch via enzymatic reactions at sub-gelatinization temperatures. Moreover, certain preparation conditions like spray freeze drying or vacuum freeze drying can also yield porous particles without the need for porogens or templating agents.

In summation, the selection of a fabrication method for porous particles is contingent upon the desired characteristics of the final product, each method presenting its own set of advantages and limitations. Researchers are thus advised to meticulously select the most suitable technique based on their specific objectives and the inherent properties of the material being processed.

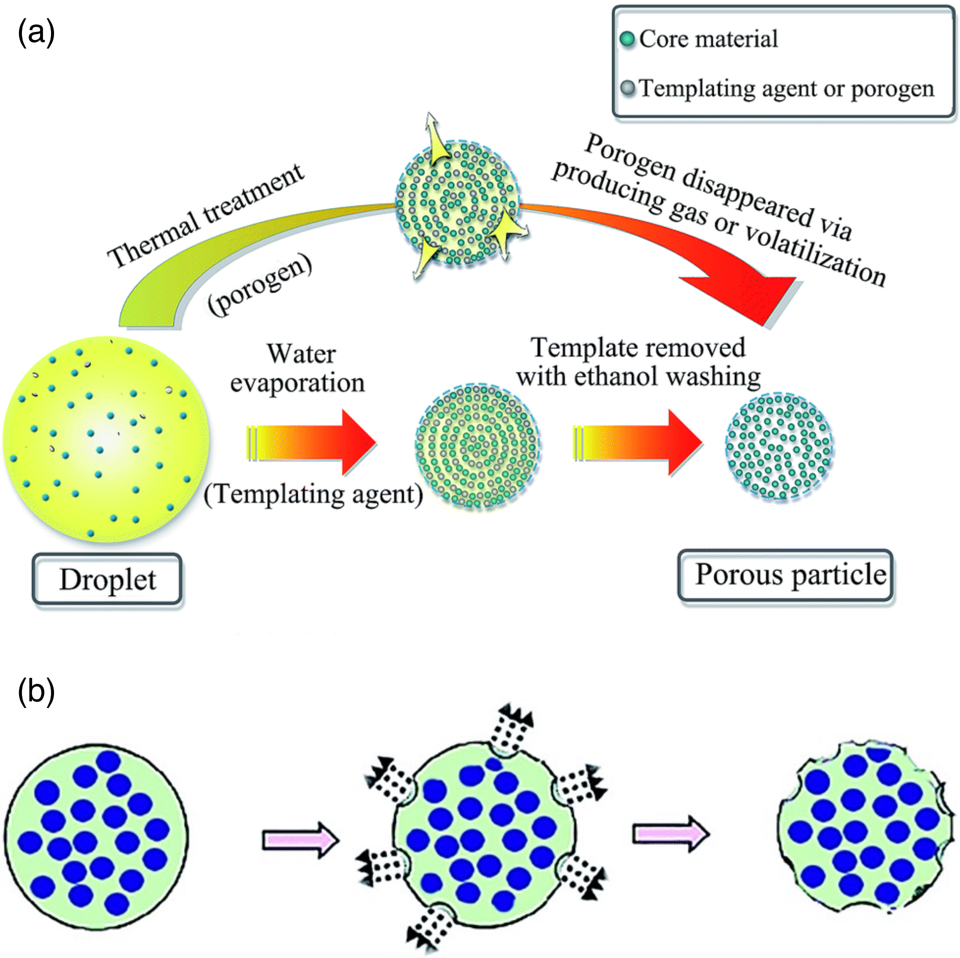

Figure 1.8: (a) The synthesis of porous particles involves employing porogens or templating agents to create pores within the structure. (b) The fabrication of porous particles is achieved through the utilization of amphiphilic polymers to form the particle's framework. Adapted from [40].

1.2.3 Template-assisted spray drying to prepare porous particles

Spray drying stands as the predominant and preferred technique for the creation of particles, offering superior capabilities for the production of particles whose sizes can be precisely adjusted from micrometers to sub-micrometer and even to the nanoscale by altering process parameters. Numerous strategies have been formulated for generating porous particles through the spray-drying approach.[42,43,44,45,46] Template-assisted spray drying is widely employed in this context, involving two primary steps in Figure 1.9: (i) the generation of composite particles that include both host materials and templates, and (ii) the synthesis of nanostructured particles through the removal of templates from these composite entities.[43] The resulting particle morphology is highly structured and adjustable, influenced by the composition of the precursor, properties of the droplets, and the processing conditions. A significant advantage of this technique is the simplicity of the template removal, which can be achieved through either heat treatment or etching. The choice of templates, based on their sizes and shapes, facilitates the control over the pore size, density, and arrangement in the final spray-dried product.

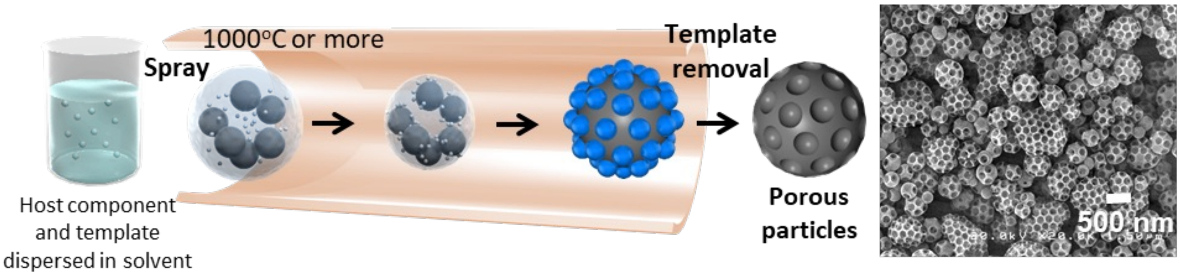

Figure 1.9: Schematic illustration for the porous particle formation. Adapted from [46].

1.3 ADVANTAGES OF MACROPORES OVER MICRO AND MESOPORES

Pore structure plays a crucial role in a variety of applications, including catalysis, gas adsorption, protein adsorption, and water filtration. Among the different pore types of micropores, mesopores, and macropores; macropores offer several distinct advantages in specific contexts. These benefits are particularly evident in terms of mass transfer and accessibility, which are critical factors in enhancing the efficiency and effectiveness of these processes. The primary advantage of macropores lies in their superior mass transfer capabilities. Larger pore sizes facilitate the movement of molecules within the pores, reducing diffusion limitations that are often encountered with micropores and mesopores, as shown in Figure 1.10. This increased accessibility ensures that active sites within the material are more readily available for interaction, thereby improving overall performance.

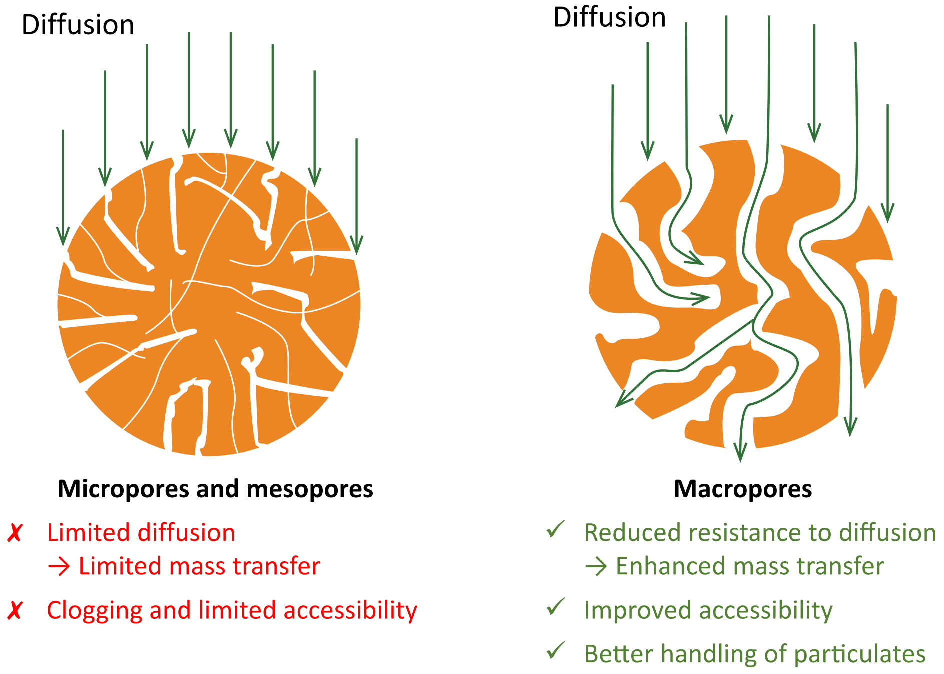

Figure 1.10: The advantages of macropores in mass transfer and accessibility.

In catalysis, the efficiency of the process is often dictated by the accessibility of active sites and the ease of diffusion of reactants and products. Macropores, defined as pores larger than 50 nanometers, provide superior accessibility compared to micropores (pores less than 2 nanometers) and mesopores (pores between 2 and 50 nanometers). The larger size of macropores reduces diffusion limitations, allowing for faster transport of reactants to active sites and products away from them. This can lead to enhanced catalytic performance, particularly in reactions involving bulky molecules. For example, Le et al.[47] synthesized three-way catalyst (TWC) particles with distinct structural configurations, including nanoparticles, aggregates, and macroporous structures, as illustrated in Figure 1.11. The catalytic performance evaluation reveals that the macroporous TWC particles exhibit superior catalytic activity for CO oxidation compared to the other investigated structures. At an operating temperature of 130 °C, the macroporous TWC particles achieve a CO conversion rate of 52 ± 1 mL min^{-1} $\mathrm{g}_{\mathrm{cat}}^{-1}$. This conversion rate is approximately 1.5 times higher than that of the aggregate TWC particles, which exhibit a conversion rate of 34 ± 5 mL min^{-1} $\mathrm{g}_{\mathrm{cat}}^{-1}$, and the TWC nanoparticles, which show a conversion rate of 35 ± 11 mL min^{-1} $\mathrm{g}_{\mathrm{cat}}^{-1}$. Gas adsorption is another field where macropores offer notable advantages. While micropores and mesopores are essential for high surface area and adsorbent capacity, macropores provide critical pathways for gas molecules to reach these smaller pores efficiently. This hierarchical pore structure can lead to faster adsorption kinetics and better performance under dynamic conditions. Liu et al. demonstrated that adsorbents with a combination of micro-, meso-, and macropores exhibited superior CO_2 capture performance compared to those with only micropores or mesopores. The macropores acted as highways for gas molecules, significantly reducing the time required to reach the adsorption sites within smaller pores.[48] In protein adsorption, the size and shape of the protein molecules necessitate the use of larger pores. Macropores are particularly beneficial for the adsorption of large biomolecules due to their ability to accommodate the size of these molecules without steric hindrance. This leads to higher adsorption capacities and faster adsorption rates. Qiao et al.[49] investigated the adsorption isotherms of four macroporous cellulose microspheres (MCMs), finding that all exhibited typical favorable adsorption equilibria, with adsorption capacity increasing in response to higher protein concentrations, as shown in Figure 1.12. The adsorption behavior of bovine serum albumin (BSA) on the four MCM samples was similar, indicating that macropore size had a negligible effect on adsorption equilibria. In contrast, γ-globulin adsorption displayed a different pattern compared to BSA adsorption. The MCMs4.5 sample, which has larger pore sizes, demonstrated a significantly higher q_c value of 340 mg/mL compared to the other three samples. This difference is likely due to the larger size of γ-globulin compared to BSA (Stokes radius: 5.9 nm for γ-globulin versus 3.9 nm for BSA). The larger size of γ-globulin can block smaller pores that are accessible to

BSA, rendering them unavailable for γ-globulin binding and entry. Consequently, this results in relatively lower adsorption capacities for MCM samples with smaller pores.

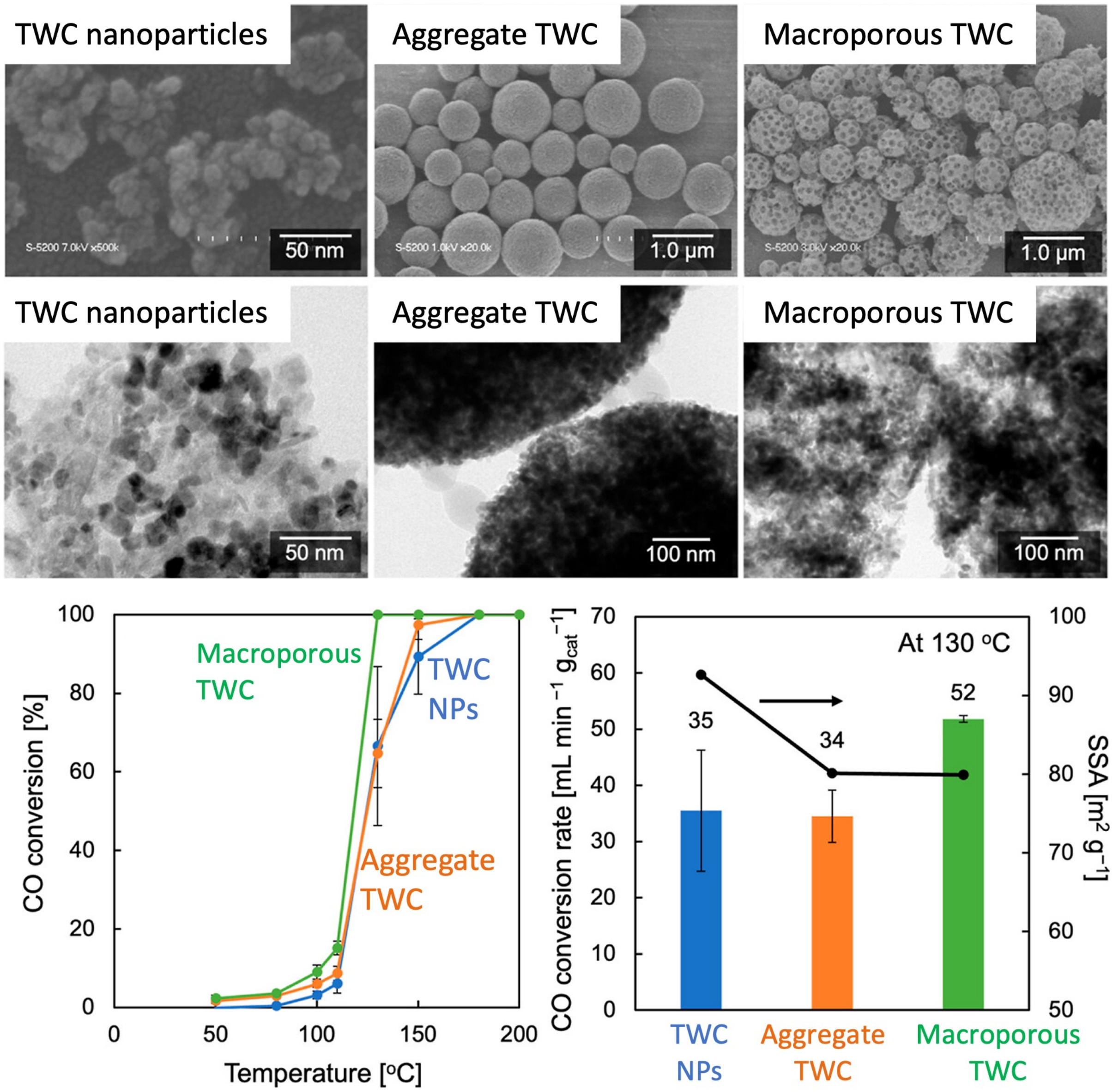

Figure 1.11: SEM and TEM images of the nanoparticles, aggregates, and macroporous three-way catalyst (TWC) samples, as well as their catalytic performances and CO conversion rates at 130 °C and an SV of 400 L h^{-1} g_{cat}^{-1}. Adapted from [47].

In conclusion, while micropores and mesopores are critical for achieving high surface areas and adsorption capacities, the inclusion of macropores provides significant advantages in catalysis, gas adsorption, protein adsorption, and water filtration. The larger pore size of macropores enhances accessibility, reduces diffusion limitations, and improves overall process efficiency. The benefits of macroporous structures are well-

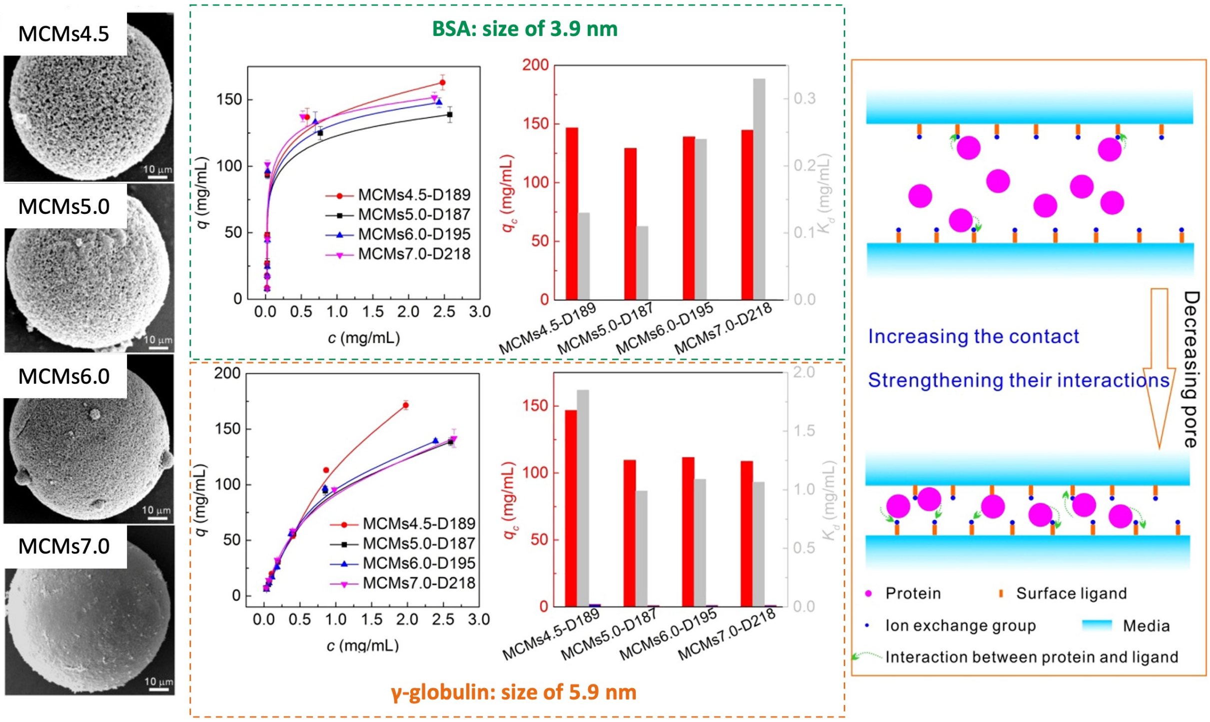

Figure 1.12: Adsorption equilibria and adsorbed density calculated from Langmuir equation (q_c) values at an equilibrium protein concentration of 1.5 mg/mL of BSA and γ-globulin on macroporous cellulose microspheres (MCMs); schematic adsorption illustrations of proteins at different pore sizes. Adapted from [49].

documented in the literature, highlighting their importance in optimizing performance across various applications.

1.4 POLYSACCHARIDE PARTICLES FOR PROTEIN ADSORPTION AND DRUG DELIVERY

Over the past twenty years, the development and structuring of polymers have emerged as a significant advancement with the potential to enhance a broad range of scientific and technological domains, including but not limited to, bioengineering, electronics, biotechnology, and medical applications.[50,51,52] This advancement is noteworthy for its environmental benefits, attributed to the low-cost formulation of multifunctional new materials, promising to introduce groundbreaking innovations across the aforementioned fields. The precision required in the structuring or modification of such polymers necessitates the adoption of micro- and nanotechnology techniques. Within this realm, maturally polymeric particles have gained prominence for their capacity to facilitate smart and controlled delivery of compounds, boasting attributes of biocompatibility and minimal toxicity.[53] Despite these advantages, the synthesis of these materials often falls short of green chemistry principles, with certain byproducts of the manufacturing process posing environmental and human health risks, thus constraining their widespread production. In light of these challenges, there's a growing consensus on the need for sustainable practices within nanotechnology. Efforts are increasingly being directed towards methodologies that minimize the generation of toxic byproducts. One such sustainable approach involves utilizing natural polysaccharides like chitosan, starch, and pectin for particle production.

Research in this direction has led to the development of spray-dried particles based on polysaccharides, which were assessed for their ability to maintain structural integrity and control the release of proteins, using bovine serum albumin (BSA) as a model protein.[54] These particles, comprising water-soluble chitosan for mucoadhesion and biocompatibility, hydroxypropyl-β-cyclodextrin, and polyethylene glycol for protein stabilization during the spray drying process, were fabricated with a mean diameter of 6–7 μm. Notably, these particles demonstrated an encapsulation efficiency for BSA exceeding 70%, and in vitro release studies using the Transwell® insert revealed a sustained release profile when compared to unencapsulated BSA.

Polysaccharides, in contrast to synthetic hydrophilic polymers, are endowed with a myriad of hydrophilic functional groups such as hydroxyl (OH), carboxyl (COOH), and amine (NH_2) groups (Figure 1.13a). These functional moieties play a pivotal role in the water absorption capabilities of polysaccharides, leading to their subsequent swelling. This unique structural attribute of polysaccharides enables them to offer a range of functional properties to polysaccharide-based systems for various application such as drug and gene delivery, textile, packaging, food additive (Figure 1.13a). Up to now, according to a survey on Web of Science from the year 2000, the number of studies on polysaccharide particles has increased significantly (Figure 1.13b). Notably in bioadhesion and controlled release, the potential for polysaccharide-based drug delivery systems to facilitate controlled release has been widely investigated, showcasing their efficacy in the sustained delivery of a diverse array of therapeutic agents, including chemotherapeutic drugs, proteins, peptides, and nucleic acids.[55] The mechanism behind the controlled release of therapeutics from swollen polysaccharides is intricately linked to the material's porosity or swelling degree, which can be fine-tuned through external parameters such as pH, temperature, ionic strength, and the application of electric fields.[56] This adaptability allows for the precise control of drug release rates and targeting, enhancing the efficacy of drug delivery. Among various polysaccharides, starch stands out for its effectiveness, particularly in the oral delivery of poorly soluble drugs.[57] Luo et al. demonstrated the encapsulation of curcumin within starch microparticles, resulting in a formulation that exhibited improved stability against photodegradation and oxidative changes.[58] Additionally, the research highlighted the ability to precisely adjust the size of curcumin-loaded starch microparticles from 0.3 to 2 μm by modulating the rate of the debranching reaction. This modification directly influenced the release characteristics of curcumin, suggesting the possibility of tailoring the release profile and target site by adjusting the crystallinity or dimensions of the microparticles. In the other research, the fabrication of colonic enzyme-responsive dextran-based oligoester crosslinked nanoparticles for the controlled release of the anticancer drug 5-fluorouracil (5-FU) is reported.[59] The 5-FU-loaded nanoparticles (DNPs, size $\sim$237 ± 25 nm, ζ-potential -17.0 ± 3 mV) were developed through in-situ crosslinking of dextran with a bifunctional telechelic oligoester, followed by physical drug encapsulation via nanoprecipitation. The encapsulation efficiency and drug loading capacity of the DNPs were determined to be approximately 76% and 8%, respectively. The DNPs demonstrated selective drug release in the presence of the dextranase enzyme. *In vitro* release kinetics assays revealed that the DNPs released about 75% of the entrapped drug within 12 hours of incubation with the dextranase enzyme (Figure 1.13c). These advancements underscore the versatility and potential of polysaccharide-based systems in the development of sophisticated drug delivery platforms.

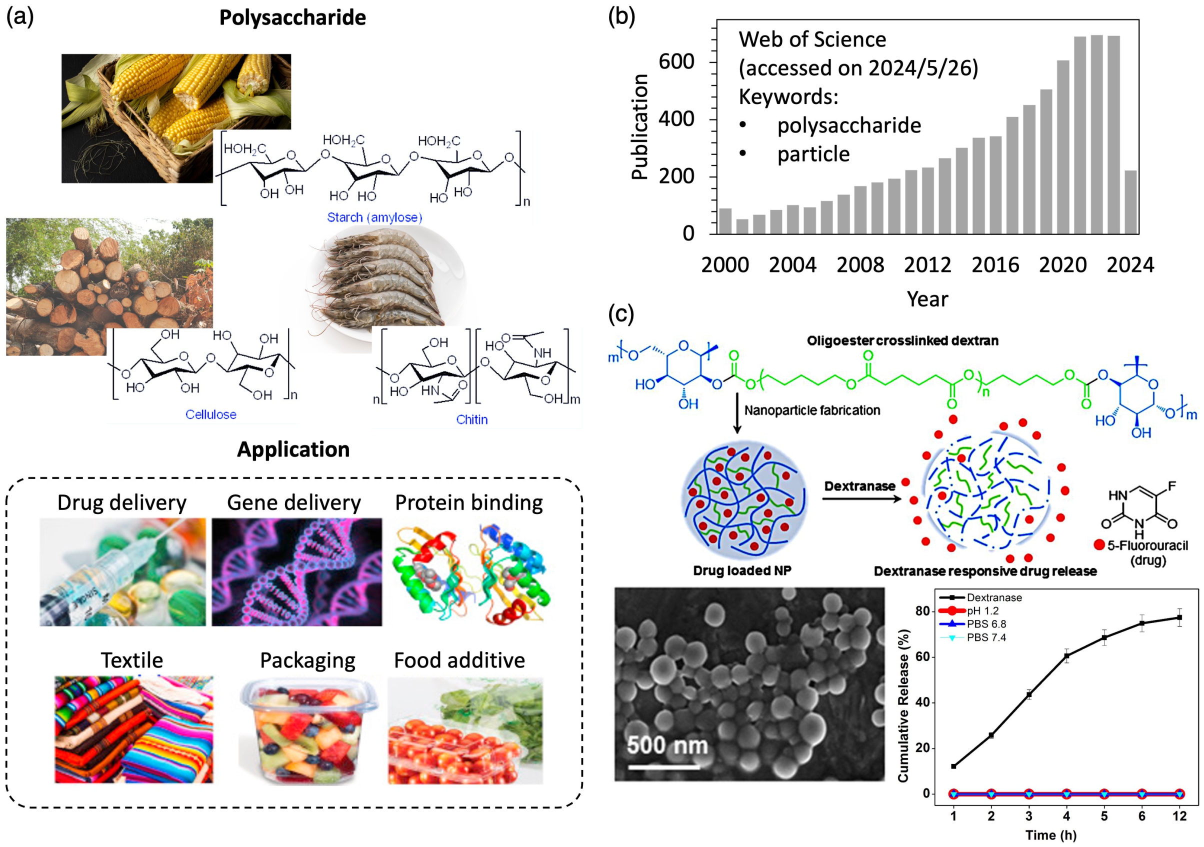

Figure 1.13: (a) Some polysaccharide exists in the natural sourses, and their applications. (b) Survey on polysaccharide particles from Web of Science accessed on 2024/5/26. (c) The fabrication of DNP in the presence of 5-FU, and the depiction of dextranase responsive drug release. Adapted from [59].

In the current scenario, porous particles synthesized via aerosol methods from materials such as metals, metal oxides, and synthetic polymers have been extensively developed. However, the production of porous particles from natural polymers, specifically polysaccharides, remains limited. This limitation arises from the thermal sensitivity of polysaccharides, necessitating the use of methods that do not involve excessively high temperatures. Consequently, research on the synthesis of porous polysaccharide particles using aerosol methods presents an intriguing and necessary area of investigation.

1.5 OBJECTIVES AND OUTLINE OF THE DISSERTATION

In this dissertation, through the utilization of an aerosolization technique our objective is to develop advanced adsorbents in the form of nanostructured particles. These particles are synthesized from environmentally benign and biocompatible raw materials, endowed with the following properties:
(1) Easy to be handling
(2) Highly biocompatible
(3) Based on sustainable materials
(4) Excellent adsorption capacity
(5) Good mass transfer

Porous polysaccharide particles have been synthesized using a template-assisted spray drying method to fulfill the aforementioned requirements. Initially, a variety of templates were explored to generate distinct porous structures within the polysaccharide particles. Subsequent investigations focused on the effects of varying template concentrations on the control of the structure and properties of the porous polysaccharide particles. Additionally, the relationship between the porous structure and protein adsorption capabilities, as well as drug release properties, was examined to elucidate the dynamics and mechanisms underpinning the adsorption and release processes.

In Chapter 2, utilizing a template-assisted spray-drying method coupled with a subsequent chemical etching step, we have fabricated porous particles from pectin, a naturally occurring biopolymer in plants, composed of D-polygalacturonic acid linked through α-1,4-glucosidic bonds. The process involved the use of either an organic template, specifically poly(methyl methacrylate) (PMMA), or an inorganic template, namely calcium carbonate ($CaCO_3$), to investigate their influence on the development of macroporous structures within the pectin particles. Additionally, we varied the template concentration in the precursor solution to elucidate the formation mechanism of these porous structures. Our findings indicate that the synthesized porous particles retain the intrinsic properties of pectin, with the choice of template significantly impacting the particle morphology, size (3 to 8 μm), pore size (80 to 350 nm), and pore volume (0.024 to 1.40 cm^3/g). Notably, particles formed using the $CaCO_3$ template exhibited a remarkable specific surface area of 171.2 m^2/g—114 times greater than that of nonporous pectin particles, highlighting the efficacy of employing PMMA and $CaCO_3$ templates for tailoring the properties of porous materials.

In Chapter 3, by modulating the concentration of $CaCO_3$, the specific surface area of these particles was regulated between 177.0 and 222.3 m^2/g. The study further delved into how the macroporous configuration, substantial specific surface area, and the cohesive pore network contribute to the adsorption capabilities and mechanism for protein (lysozyme). Remarkably, all variants of the porous pectin particles exhibited rapid adsorption rates (approximately 65% of the total capacity within the initial 5 minutes) alongside a significant increase in adsorption capacity, ranging from 1543 to a peak of 2621 mg/g. This enhanced performance is ascribed to the extensive availability of binding sites within the macropores, facilitated by their expansive surface areas and well-integrated pore networks. The macroporous pectin particles achieved in this investigation demonstrated an unparalleled adsorption capacity for lysozyme (2621 mg/g) compared to existing adsorbents.

In Chapter 4, we focused on the synthesis of porous pectin particles, intended for use as drug delivery vehicles, with indomethacin serving as the model drug. These particles notably enhanced their specific surface areas to 203 m^2/g—a significant improvement from the 1 m^2/g observed in nonporous counterparts. The engineered porous structure facilitated a shorter diffusion path for drug molecules, thereby accelerating the release rate. Analysis of the release mechanism revealed a predominance of Fickian diffusion in the porous pectin particles, in contrast to the erosion and diffusion combination mechanism characteristic of nonporous particles. Consequently, the drug-loaded porous pectin particles exhibited a tri-fold increase in the rate of drug release compared to their nonporous analogs. By modifying the porous architecture of these particles, we achieved a controlled release rate, presenting a highly effective method for the rapid release of drugs, specifically targeting the colonic region.

In Chapter 5, we presents a summary of all topics and future prospects.

2

Synthesis of Porous Pectin Particles by a Template-Assisted Spray Drying

Many types of porous particles containing inorganic and organic substances, such as carbon, metals, metal oxides, inorganic–organic hybrids, and polymers, have been developed. However, natural polymer-derived particles are relatively rare. To our knowledge, this report describes the first synthetic method for obtaining meso-/macroporous particles made from pectin, which is a natural polymer with a wide range of biological activities suitable for active substance support applications. These porous particles were prepared using a template-assisted spray-drying method, followed by a chemical etching process. An organic template [i.e., poly(methyl methacrylate) (PMMA)] or an inorganic template [i.e., calcium carbonate ($CaCO_3$)] was used to evaluate the resulting formation of macroporous structures in the pectin particles. Furthermore, the concentration of the templates in the precursor solution was varied to better understand the mechanism of porous pectin particle formation. The results showed that the final porous particles maintained the characteristic properties of pectin. The differences between the two templates resulted in two distinct types of porous particles that differed in their particle morphologies (i.e., spherical or wrinkled), particle sizes (ranging from 3 to 8 μm), pore sizes (ranging from 80 to 350 nm), and pore volume (ranging from 0.024 to 1.40 $cm^3\ g^{-1}$). Especially, the porous pectin particles using the $CaCO_3$ template have a significantly high specific surface area of 171.2 $m^2\ g^{-1}$, which is 114 times higher than that of nonporous pectin particles. These data demonstrated the potential for using PMMA and $CaCO_3$ templates to control and design desired porous materials.

---

published in part in *Langmuir* 2021, 37, 4256–4266

2.1 INTRODUCTION

Porous structured particles have attracted interest since the twentieth century and have been applied in various fields.[60,61,62] These porous structured particles have several inherent characteristics, such as a large surface area, high porosity, low density, and enhanced storage capacity, which distinguish them from conventional dense particles.[63,64,65] These features enable the porous particles to exhibit excellent performance in terms of catalyst,[66,67] adsorption,[68,69] gas/liquid separation,[70,71] sensor,[72,73] supercapacitor,[74,75] and drug delivery.[76,77] Because of this wide potential applicability, substantial research efforts have been dedicated to producing various porous structured particles.[78,79]

Among the numerous types of porous structured particles, macroporous particles, which contain pores larger than 50 nm, are currently considered as "new generation materials", owing to their unique and attractive mass transport properties.[79,46,80] In terms of catalytic applications, tungsten trioxide particles with highly-ordered macropores have been reported.[81] These particles demonstrated improved penetration and promoted interactions between molecules and light in the deepest parts of the active catalyst, resulting in an enhanced photocatalytic rate. In addition, it has been demonstrated that a macroporous structure can increase the soot–catalyst contact efficiency during the catalytic purification of soot by boosting the mass transfer and diffusion of the soot particles.[82] Regarding the use of macroporous particles as adsorbents, cellulose nanofiber-loaded macroporous silica particles were successfully prepared with an abundance of accessible binding sites by tuning the macropore size of the silica particles to attain a superior protein adsorption capacity.[79] This result indicated that the mass transfer of biomolecules is controlled by electrostatic interactions between the adsorbent and the adsorbate, as well as the diffusion of these molecules into the pores. When the pore size was larger than the biomolecule's size, mass transfer was principally controlled by pore diffusion, since a large pore could allow for better intraparticle diffusive transfer.[83] Overall, it is essential to expand the scope of research in this field to synthesize macroporous particles comprising various kinds of materials.

In the past decade, macroporous particles derived from various inorganic and organic materials, such as carbon,[84] metals,[85] metal oxides,[86] inorganic-organic hybrid materials,[87] and polymers[88] have been developed and tuned. Aiming to expand the scope of macroporous particles derived from nature, our research group focuses on pectin because it is an environmentally friendly natural polymer that is abundant in plant cell walls. In addition, pectin was recommended for the treatment of infections, allergies, and arthritis, owing to its ability to reach discrete compartments (e.g., eyes, lungs, and joints).[89] Importantly, it can be used to manufacture biocompatible and biodegradable materials because it is not hindered by any toxicity or biodegradability problems.[90]

Pectin can be synthesized as microparticles using an emulsion technique in solution,[91,92] or via an aerosol method, such as spray drying.[93,94] The emulsification method is primarily employed to produce pectin microparticles;[92] however, this method involves a complicated process that includes pouring oils and adding surfactants. After manufacturing the particles, the used oil and surfactant must be eliminated using organic solvents. In addition, the product is often contaminated with impurities, since surfactants may not have been completely removed. To overcome the drawbacks of the emulsion method, a novel strategy for fabricating pectin microparticles without using oils or surfactants was developed.[94] Lee et al. were successful in fabricating pectin particles using a spray drying method; these particles had regular spherical morphologies and a dense structure. The researchers investigated their drug release performance and showed that the drug release rate was effectively controlled. Nevertheless, to our knowledge, there are no studies focusing on controlling the morphology and structure of the pectin particles because of their limitation at high temperature and solubility in many solvents.

In this report, we describe the synthesis and characterization of macroporous pectin particles, with special attention paid to the advantageous aspects of macroporous structured particles mentioned above. To avoid the thermal decomposition of the natural polymer, which occurs at high temperature during the synthesis of porous particles, we applied a template-assisted spray drying method in combination with a chemical etching process. The template-assisted spray drying method is a well-established strategy for producing various nanostructured particles, including macroporous particles.[42,43,44,45] This method typically involves two main processes, including (i) the formation of composite particles consisting of host components and templates, and (ii) the production of nanostructured particles by removing the templates from the prepared composite particles.[43] The morphology of the obtained particles is highly ordered and controllable because it depends on the initial precursor component, droplet properties, and parameter conditions. In this method, the choice of the template plays a crucial role in the formation of the porous particles. The selected template should form pores of the desired size and should be economical and environmentally friendly. In this research, owing to their numerous attractive features, poly(methyl methacrylate) (PMMA) and calcium carbonate ($CaCO_3$) of various particle sizes were used as templates to investigate the formation of porous structures. PMMA has a relatively low decomposition temperature and can be dispersed homogeneously in solution;[42,95] $CaCO_3$ is advantageous because it can easily be removed using weak acids, which ultimately lessens the environmental impact.[96] Moreover, PMMA and $CaCO_3$ are cost-effective, meaning this method could be profitable for large-scale industrial development. To our knowledge, this article reports the first successful synthesis of macroporous structured pectin particles. The fabricated macroporous particles all exhibited enhanced specific surface areas compared with non-porous particles, although the results obtained using the $CaCO_3$ template clearly differed from those obtained using PMMA. In addition, the macroporous particles obtained from the two different types of templates had distinct properties in terms of morphology, particle size, and pore size. To explain these differences, the particle formation mechanisms in the two cases are also discussed herein.

2.2 MATERIALS AND METHODS

2.2.1 Preparation of porous pectin particles

The porous pectin particles were prepared by a template-assisted spray drying method, followed by a chemical etching process, as illustrated in Figure 2.1. First, an aqueous precursor solution containing raw pectin (supplied by Herbstreith & Fox GmbH & Co. KG Pektin-Fabriken, Neuenbürg, Germany) as the host material, and either PMMA (powder; Sekisui Plastics Co., Ltd., Tokyo, Japan) or $CaCO_3$ (30 wt.% in aqueous solution; Shiraishi Calcium, Osaka, Japan) as the template was prepared in deionized (DI) water as the dispersant media. The concentration of pectin in the precursor solution was controlled (as high as 1.0 wt.%), and the templates (PMMA or $CaCO_3$) were used in mass ratios of 1, 2, or 4, relative to pectin. The samples were labeled as PPT-X-Y, where X represents the template particles (X = P for PMMA, and C for $CaCO_3$), and Y indicates the mass ratio of template particles to pectin (Y = 1, 2, or 4). The details of the precursor solution contents are provided in Table 2.1.

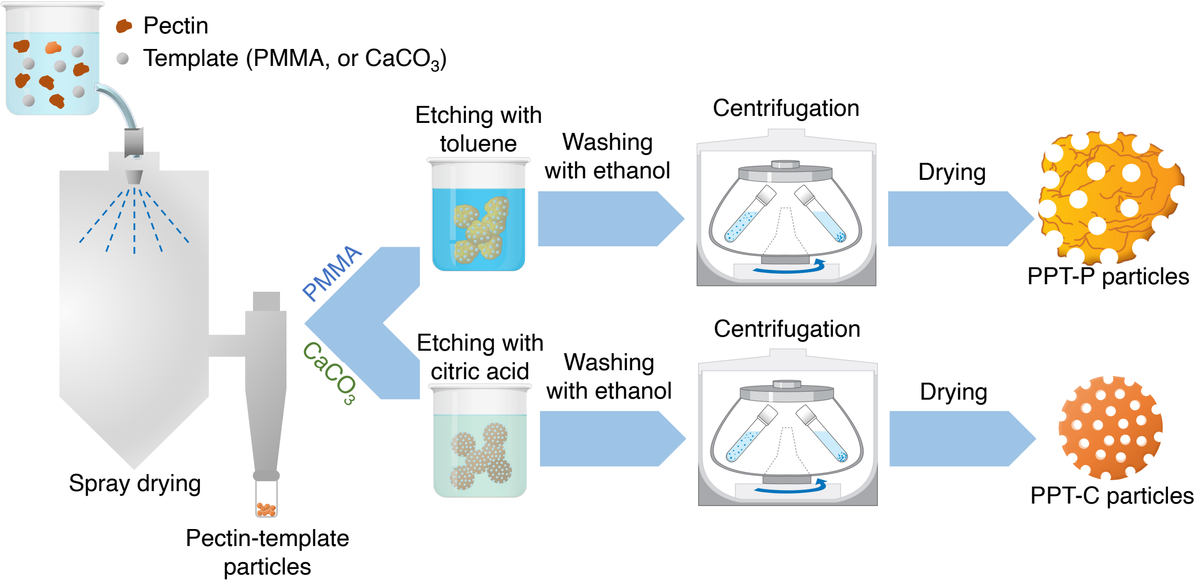

Figure 2.1: Preparation of porous pectin particles using PMMA or $CaCO_3$ templates. PPT-P = porous pectin particles using PMMA; PPT-C = porous pectin particles using $CaCO_3$.

The aqueous precursor was then homogenized using an ultrasonic device (T 10 basic ULTRA-TURRAX® S004, IKA®, Japan) with a rotation speed of 12800 rpm for 30 min to disperse the template molecules. Spray drying was performed using a mini spray-

Table 2.1: The contents and concentrations of porous pectin particle precursor solutions.

		Template				
Sample	Pectin (wt.%)	PMMA (wt.%)	$CaCO_3$ (wt.%)	DI water (wt.%)	Total volume (mL)	Yield (%)
PPT-0	1.0	-	-	99.0	50	64.8
PPT-P-1	1.0	1.0	-	98.0	50	60.9
PPT-P-2	1.0	2.0	-	97.0	50	61.7
PPT-P-4	1.0	4.0	-	95.0	50	62.7
PPT-C-1	1.0	-	1.0	98.0	50	74.1
PPT-C-2	1.0	-	2.0	97.0	50	77.4
PPT-C-4	1.0	-	4.0	95.0	50	64.1

dryer (BÜCHI B-290, Flawil, Switzerland) equipped with an external two-fluid mixing nozzle with a 0.7 mm liquid orifice diameter and a 1.5 mm gas orifice diameter. The precursor solutions were fed into the spray-dryer at a flow rate of 3 mL min^{-1}, leading to atomization and the formation of dried composite particles. During this process, a temperature of 150 °C was established as the inlet air temperature. The spray gas flow rate and aspiration rate were set to 357 L h^{-1} and 37000 L h^{-1}, respectively. A sample of spray-dried pectin only (PPT-0) was prepared as a control using the same method for comparison with the characteristics of porous pectin particles.

The dried composite particles were then etched and washed to generate the porous structures. The dried composite pectin-PMMA particles were added to toluene (Kanto Chemical Co., Inc., Japan) and stirred for 30 min to remove the PMMA templates. After that, they were centrifuged at 15000 rpm for 5 min, washed thoroughly with ethanol, and dried in a vacuum oven at 80 °C for 1 h to produce the PPT-P particles. The composite pectin-$CaCO_3$ particles were added to a 10.0 wt.% citric acid (Sigma Aldrich, Japan) aqueous solution and stirred for 15 min to remove the $CaCO_3$ templates. Then, they were centrifuged at 8000 rpm for 5 min and washed thoroughly with ethanol. After washing, they were dried in an oven at 80 °C for 1 h to obtain the final PPT-C particles.

2.2.2 Characterization of porous pectin particles

The morphologies of the porous pectin particles were investigated using scanning electron microscopy (SEM) S-5000 (Hitachi Ltd., Tokyo, Japan). The zeta (ζ) potential of particles was analyzed using Zetasizer Nano ZS (Malvern Instrument Inc., London, U.K.). A Fourier transform infrared (FT-IR) spectrophotometer IRAffinity-1S + MIRacle 10 (Shimadzu, Japan) was used to analyze the functional groups present in the samples. The specific surface area (SBET) of the samples was determined from N_2 adsorption-desorption isotherms obtained at 77 K using BELSORP-max (BEL Japan, Osaka, Japan); the specific surface areas were calculated using the Brunauer-Emmett-Teller (BET) method. The pore volume and pore size distribution were determined using the Barrett-Joyner-Halenda (BJH) and Horvath-Kawazoe (HK) methods, respectively.

2.3 RESULTS AND DISCUSSION

2.3.1 Morphology of porous pectin particles

The morphology of particles containing only pectin, composite particles, and porous pectin particles prepared at mass ratios of templates (PMMA or $CaCO_3$) to pectin of 4 are presented in Figure 2.2. As shown in Figure 2.2a-c, spray drying of precursor solutions containing only pectin (PPT-0) afforded spherical particles in 64.8% yield. After the spray drying process, composite particles consisting of the host material (pectin) and template (PMMA or $CaCO_3$) were formed with yields over 60% (Figure 2.2d, g). When the PMMA template was used, a change in morphology was observed; the particles adopted a concave form and non-spherical morphology. In contrast, when the $CaCO_3$ template was used, the particle morphology remained spherical. The morphological difference between these porous particles is discussed further in section 3.3. Chemical etching of the composite particles generated porous structures in the final particles. Figure 2.2e, h show that porous structures were successfully introduced in the pectin particles after spray drying followed by removal of the templates. Images of the final porous particles are presented in Figure 2.2 (PPT-P in Figure 2.2e-f, and PPT-C in Figure 2.2h-i). Compared with the composite particles, the morphology of the porous particles was maintained in terms of their structural integrity. These results revealed the effectiveness of combining spray drying and chemical etching processes to remove the templates from the two types of composite particles.

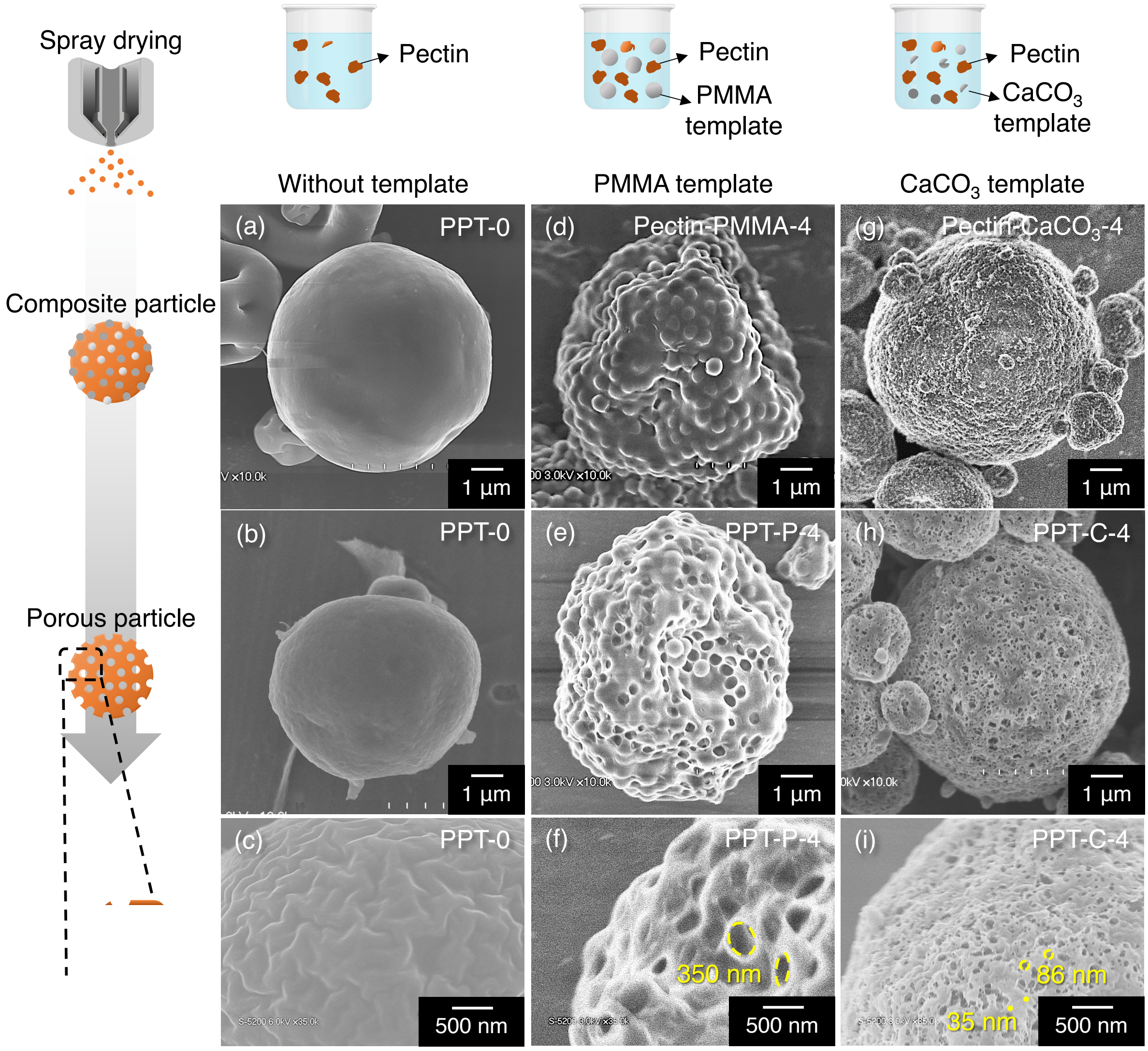

Figure 2.2: SEM images of (a-c) spray-dried pectin particles (PPT-0); (d) pectin-PMMA composite particles; (e, f) porous pectin particles prepared using the PMMA template; (g) pectin-$CaCO_3$ composite particles; (h, i) porous pectin particles prepared using the $CaCO_3$ template. The mass ratios of template/pectin in (d-i) were 4.

2.3.2 Characterization of porous pectin particles

During the chemical etching process, PMMA was dissolved in toluene, and $CaCO_3$ was dissolved in citric acid and produced calcium citrate together with CO_2; however, pectin was insoluble in both of these solvents, thus confirming that the structural framework of the porous pectin particles comprised pectin, and the pores were formed from the removal of PMMA or $CaCO_3$. This phenomenon is supported by the FT-IR results shown in Figure 2.3. Samples of pectin, template particles (PMMA and $CaCO_3$), and porous pectin particles with a template/pectin mass ratio of 4 before (pectin-PMMA-4 and pectin-$CaCO_3$-4) and after the etching process (PPT-P-4 and PPT-C-4) were analyzed. In the PMMA case, the FT-IR spectrum of the pectin-PMMA composite particles contained the characteristic signals of PMMA (1725 cm^{-1}) and pectin (1402 and 1606 cm^{-1}) (Figure 2.3a).[45] No new signals emerged in this sample, indicating that the self-assembly of pectin and PMMA did not occur via a chemical reaction or involve other intermediate components during the spray drying process. After chemical etching, the FT-IR spectrum only contained signals similar to those of the composite particles; however, the intensity of the PMMA-specific signal decreased, which suggested that PMMA was removed after etching. In the $CaCO_3$ case, characteristic signals of $CaCO_3$ (711, 875, and 1450 cm^{-1}) and pectin (1402 and 1606 cm^{-1}) (Figure 2.3b) were observed in the spectrum corresponding to pectin-$CaCO_3$-4 composite particles.[97] There were no new signals detected (other than those typical of $CaCO_3$ and pectin), which indicated that no chemical reaction had occurred between pectin and $CaCO_3$ during the spray drying process. However, in the final product (PPT-C-4), only signals corresponding to pectin were present, without other signals (e.g., the signal corresponding to C=O of citrate group), indicating that $CaCO_3$ was removed by the etching process and the calcium citrate from the reaction of citric acid with $CaCO_3$ was also eliminated after the washing process. Therefore, we concluded that we had successfully created porous particles without damaging the pectin, because the characteristic properties of the pectin were preserved.

To confirm that the framework of the porous pectin particles was made from pectin and that the pores were formed from PMMA or $CaCO_3$ removal, the ζ potential at pH 7 of the PPT-0 particles (fabricated without using a template) was compared with that of composite particles (templates and pectin) and porous pectin particles (after template

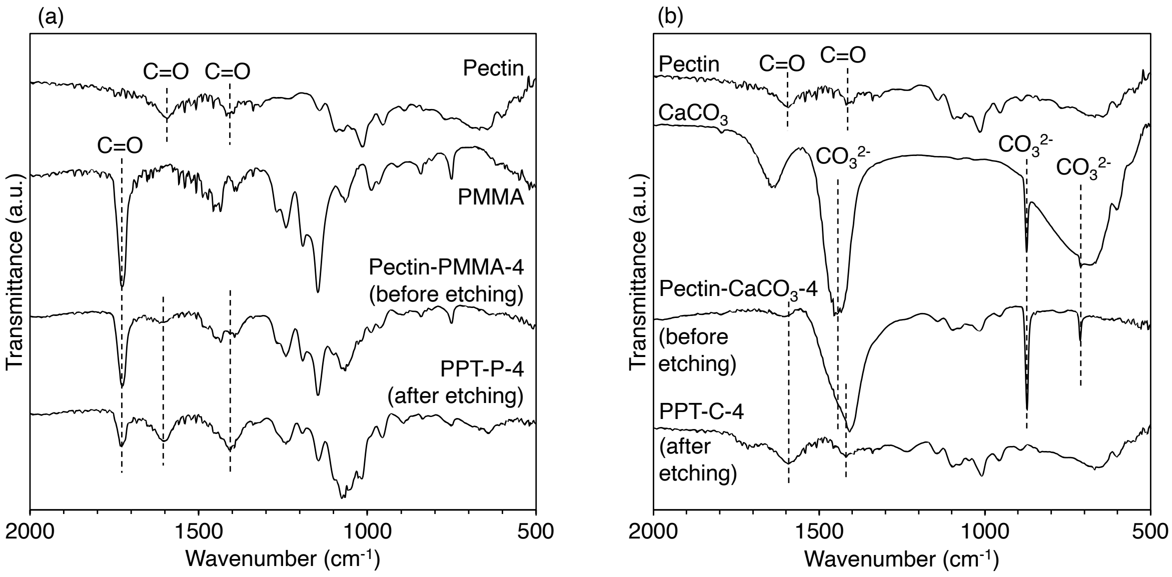

Figure 2.3: FT-IR spectra of (a) pectin, PMMA, pectin-PMMA-4 composite (before etching), and PPT-P-4 (after etching); (b) pectin, $CaCO_3$, pectin-$CaCO_3$-4 composite (before etching), and PPT-C-4 (after etching).

removal) (Figure 2.4a-b). The PPT-0 particles maintained a large negative ζ potential of −42.4 mV because of the presence of COO– groups in the chemical structure of pectin.[98] This result indicates that the spray drying process successfully built nanostructured particles without changing the chemical functional groups. After spray drying and template removal, the resulting porous particles retained large negative ζ potential values. In Figure 2.4a, for pectin-PMMA composite particles, the absolute ζ potential value increased to −51.1 mV, and this change was attributed to the presence of the carbonyl group (C=O; absorption band at 1725 cm^{-1}) in PMMA. The ζ potential value of PPT-P-4 porous structure particles was −48.4 mV, which was still more negative than that of the PPT-0 particles. This result confirmed that PMMA remained in the porous particles, which was consistent with the observed FT-IR spectral results. Additional experiments were conducted in which the volume of toluene used during etching was double, triple, and quadruple. FT-IR spectroscopic results (Figure 2.4c) also showed that PMMA was still present in porous particles. These phenomena indicated that the porous pectin particles using the PMMA template had less interconnected channels. Therefore, during etching, toluene cannot penetrate and dissolve these PMMA particles. In this research, our focus is to make porous structures without influencing pectin properties and predict particle shape and pore size; thus, further investigation of this issue needed to be studied in the future. As shown in Figure 2.4b, pectin-$CaCO_3$ composite particles had the ζ potential of −41.4 mV, which was comparable with that of PPT-0. During the formation of porous particles, the acid used to remove the $CaCO_3$ template partially converted COO– groups to COOH. Moreover, in the presence of divalent cations, such as calcium ions, a coordination complex was formed in which calcium ions were held between two pectin chains.[99] The carboxyl groups and calcium ions formed a junctional zone as an egg-box model (Figure 2.4d), which reduced the number of carboxyl groups in pectin. The factors mentioned above led to an increase in the ζ potential of PPT-C-4 (to –35.4 mV).

Experiments using various template/pectin ratios were also performed to confirm that the pores were formed from removal of the template molecules. In both cases, the template and pectin were prepared in mass ratios of 1, 2, and 4. After chemical etching to remove the templates, the porous particles were successfully formed, as confirmed by FT-IR (Figure 2.5a-b), and their morphologies are shown in the SEM images in Figure 2.5c-h. Based on the SEM images of the particles, the number of pores increased with increasing proportions of the template in the precursor solution. This indicated that PMMA and $CaCO_3$ participate in self-assembly and occupy the space inside the particles. This result further suggested that it was possible to control the pore volume by changing the template concentration.

As mentioned previously, the morphology of the pectin particles changed after the addition of PMMA, and the particles adopted a concave form, whereas the particle morphology maintained a spherical shape when the $CaCO_3$ template was used. Additionally, it was determined that the porous particles synthesized with PMMA had a larger average size relative to those synthesized using $CaCO_3$ (Figure 2.5i). In the experiments with PMMA, the average size of PPT-P particles increased from 5 to 8 μm, as the mass ratios of PMMA/pectin increased from 1 to 4. In the experiments with $CaCO_3$ templates, changing the template/pectin ratio from 1 to 4 also led to a slight increase in the average particle size (from 3 to 4 μm). The differences in particle morphology

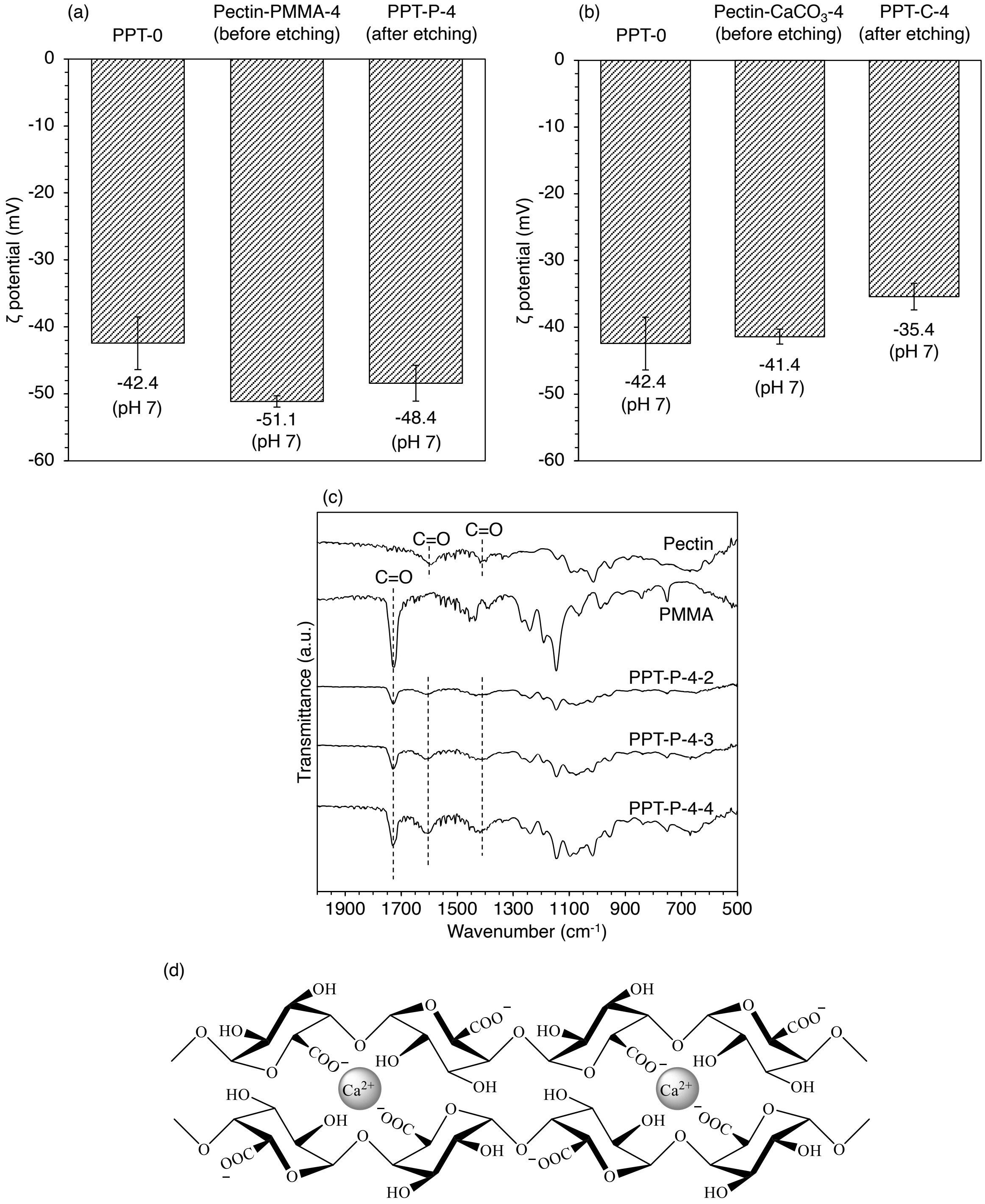

Figure 2.4: Plots showing the ζ potential at pH 7 of (a) pectin, pectin-PMMA-4 composite (before etching), and PPT-P-4 (after etching); (b) pectin, pectin-$CaCO_3$-4 composite (before etching), and PPT-C-4 (after etching). (c) FT-IR spectra of PPT-P-4 particles after etching with the increasing volume of toluene from double to quadruplicate. The samples were labeled as PPT-P-4-X, where X indicates the times in volume of toluene compared with the volume used for PPT-P-4 (X = 2, 3, or 4). (d) The egg-box model for junction zone formation in pectin – calcium ions.

and particle size are discussed further in section 3.3 as they relate to the mechanism of particle formation.

To better understand the pore size distribution of porous pectin particles prepared with different ratios of template/pectin, it was necessary to compare the pore sizes and template sizes. As shown in Figure 2.6, PMMA and $CaCO_3$ have different sizes and shapes. The PMMA used in this study had a spherical shape with an average size of 513 nm, whereas the average size of $CaCO_3$ was 86 nm with a non-spherical shape. The pores on the PPT-P particles had an average size of 351 nm (Figure 2.6a, c). Comparing the size of the PMMA particles with the pore sizes in the PPT-P sample, it was clear that the size of the pores was smaller than the original size of PMMA. This result is in good agreement with previously published work.[45] The template particles were evenly distributed throughout the precursor solution, i.e., there was no aggregation of PMMA (Figure 2.6b, d). The wide pore size distribution resulted from the abnormal surface morphology, which had many concave wrinkles. In contrast, using the smaller $CaCO_3$ template led to smaller sized pores. The average pore size in the PPT-C particles was 90 nm (Figure 2.6b, d). Furthermore, it was observed that the PPT-C particles had a similar pore size distribution relative to the size distribution of $CaCO_3$. There was an uneven distribution of $CaCO_3$ particles in the precursor, indicating that local agglomeration between $CaCO_3$ particles had occurred (Figure 2.6g); this caused a wide pore size distribution in the PPT-C particles. These results confirmed the participation and essential role of the templates in the formation of pores in the final particles.

The N_2 adsorption and desorption isotherms were investigated as a part of the pore structure analysis (Figure 2.7a-b). The particles made from only pectin (PPT-0) and the PPT-P-4 particles exhibited type II isotherms, characteristic of the adsorption of non-porous and macroporous materials.[100,101] The PPT-C-4 particles exhibited combined isothermal adsorption behavior (between type II and type IV), characteristic of mesoporous and macroporous materials.[101] The type H2 hysteresis loop occurred in this sample at a relative pressure of $P/P_0 > 0.7$, which indicated that the pores were disordered and had a wide distribution. At a relative pressure lower than 0.1, the PPT-

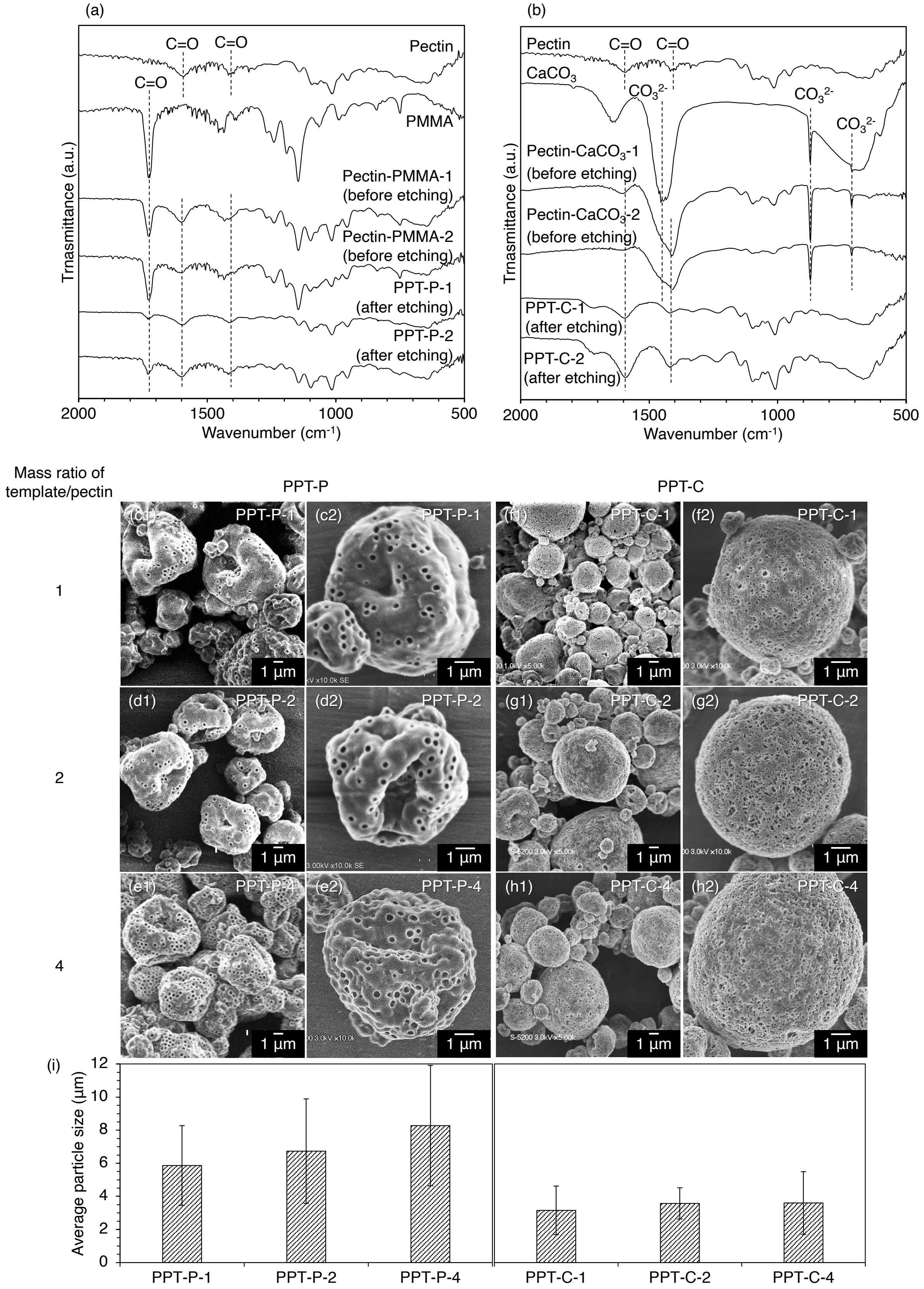

Figure 2.5: FT-IR spectra of pectin-template composite particles and PPT particles at mass ratios of template/pectin equal to 1 and 2: (a) PMMA, and (b) $CaCO_3$. SEM images of porous pectin particles prepared using PMMA as a template at mass ratios of PMMA/pectin of (c) 1, (d) 2, (e) 4, and porous pectin particles prepared using $CaCO_3$ as a template at mass ratios of $CaCO_3$/pectin of (f) 1, (g) 2, (h) 4. (i) The average particle size of porous pectin particles; 300 particles observed in the SEM images were used to calculate the average particle sizes. Error bars represent the standard deviation corresponding to SEM particle size measurements.

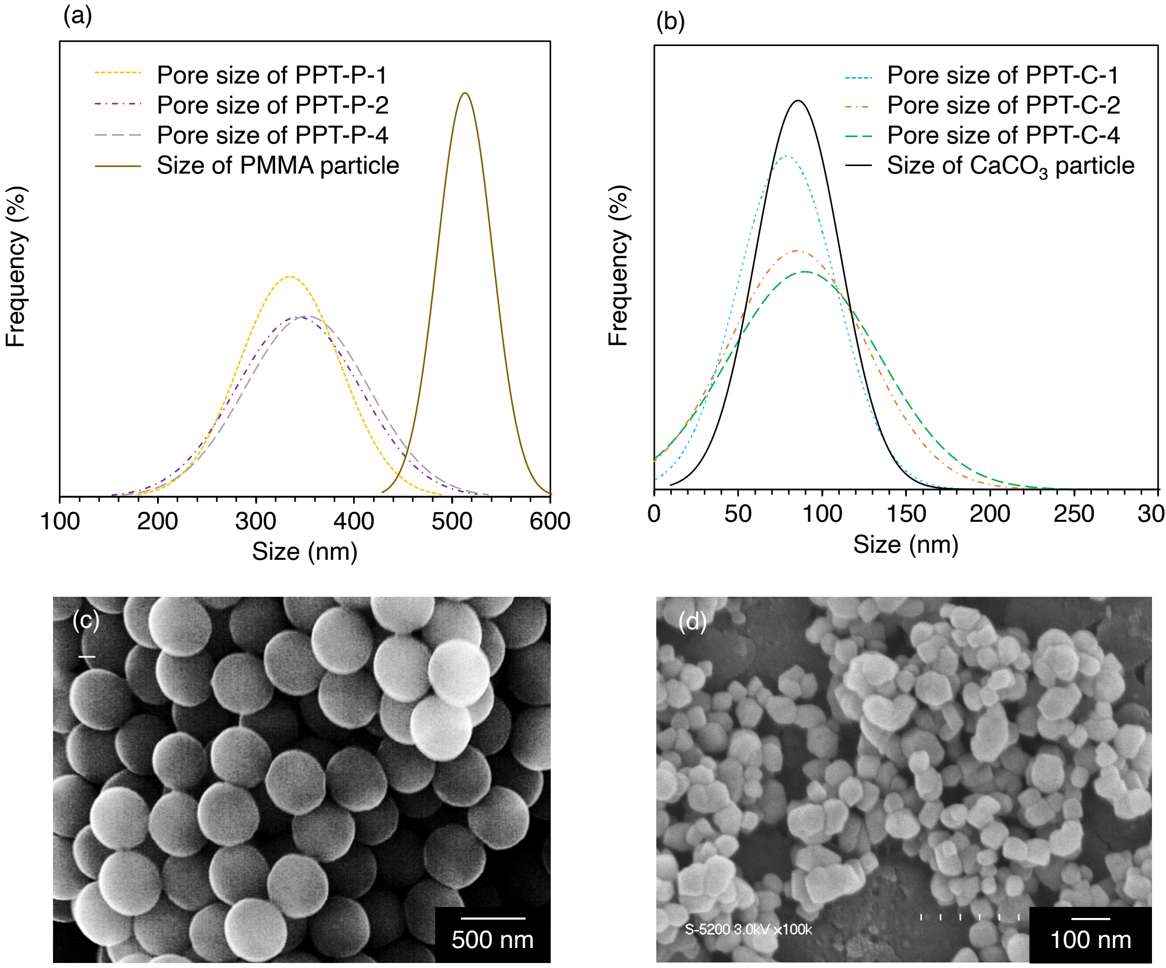

Figure 2.6: Comparison of the template size distribution and the pore size distribution of porous pectin particles prepared with different ratios of template/pectin using (a) PMMA template, and (b) $CaCO_3$ template. 300 particles observed in SEM images were used to calculate pore sizes. SEM images of (c) PMMA and (d) $CaCO_3$ templates.

0, PPT-P-4, and PPT-C-4 particles showed a gradual increase in the adsorption of N_2 gas. These results implied the presence of micropores when using PMMA and $CaCO_3$ templates; however, the number of micropores formed using PMMA was negligible relative to the number formed using $CaCO_3$.

More details of the pore size distribution of PPT-0, PPT-P-4, and PPT-C-4 particles were evaluated to determine the influence of the templates on pore formation. The general pore size distribution was analyzed in the range of 2 to 100 nm using the BJH method (Figure 2.7c), and the micropore size distribution was analyzed in the 1 to 2 nm range using the HK method (Figure 2.7d). When PMMA was used, PMMA particles collide and contact each other at the same position in the self-assembly process to form the composite particles (Figure 2.7e). This phenomenon is called the kissing effect. After the chemical etching process, PMMA templates were removed, and this kissing effect generated a porous network spanning micropores to macropores,[45] which improved the pore volumes compared with non-porous particles (PPT-0). However, the size of the PMMA was greater than 500 nm, so it was difficult to determine the exact volume of the macropores within the range of the calculations.[102] In contrast, since $CaCO_3$ was smaller than PMMA, the overall pore volume in PPT-C particles (1.40 cm^3 g^{-1}) was significantly greater than that in PPT-P particles (0.024 cm^3 g^{-1}). This enhancement of the porous network ranging from micropores to macropores may be derived from the kissing effect and arrangement of $CaCO_3$ during self-assembly and particle construction in the spray drying process. Additionally, removal of the $CaCO_3$ template using acid released CO_2 gas (molecular size $\approx$ 0.33 nm), as shown in Figure 2.7f, g. This increased the pressure and caused the structural skeleton of the particle to break, leading to pore formation. This result also demonstrated the potential advantage of using an environmentally friendly weak acid to remove $CaCO_3$ templates, which has never been reported.

Based on the data presented in Table 2.2, the incorporation of PMMA and $CaCO_3$ into pectin through spray drying significantly increased the specific surface area by forming pores of various sizes. The specific surface area calculated using the BET equation for PPT-0 particles was 1.5 m^2 g^{-1}. The specific surface area of the PPT-P-4 particles was 5.4 m^2 g^{-1}, which represents an increase of 3.6 fold. The PPT-C-4 particles had the largest specific surface area (171.2 m^2 g^{-1}). The porous structure in PPT-C-4 enhanced its specific surface area by 32 times relative to PPT-P-4, and 114 times compared with non-porous PPT-0. These results confirmed that the structure of the porous pectin particles allows for good penetration by small compounds with plenty of space on the surface and interior. With such great potential, research regarding the adsorption capacity of porous pectin particles will certainly be investigated in the future.

Table 2.2: Specific surface area and micropore, mesopore, and macropore volumes in porous pectin particles.

Sample	S_{BET} (m^2 g^{-1})	$V_{micropore}$ (cm^3 g^{-1})	$V_{mesopore}$ (cm^3 g^{-1})	$V_{macropore}$ (cm^3 g^{-1})	Total pore volume (cm^3 g^{-1})
PPT-0	1.5	5.5×10^{-4}	4.7×10^{-3}	2.3×10^{-3}	7.5×10^{-3}
PPT-P-4	5.4	2.1×10^{-3}	7.1×10^{-3}	0.015	0.024
PPT-C-4	171.2	0.063	0.43	0.96	1.4

2.3.3 Mechanism of particle formation

The morphology and size of the ordered porous structure particles formed using the spray drying method can be influenced by various factors, including the initial size of the template, the mass ratio of template particles to host materials, and the conditions of the drying process.[103,104,105,106] The pectin host materials started to decompose at 200 °C, as shown in Figure 2.8. Therefore, the temperature of hot air was fixed at 150 °C, and similar mass ratios of PMMA or $CaCO_3$ particles to pectin were used to draw comparisons. Considering the changes in the morphology of the particles generated using PMMA versus $CaCO_3$ (while maintaining identical drying conditions), we predicted that there was also a template-dependent difference in the particle formation mechanisms.

In this study, we focused on the influence of the droplet size on the morphology, structure, and size of the produced particles. The droplet size depends on the properties

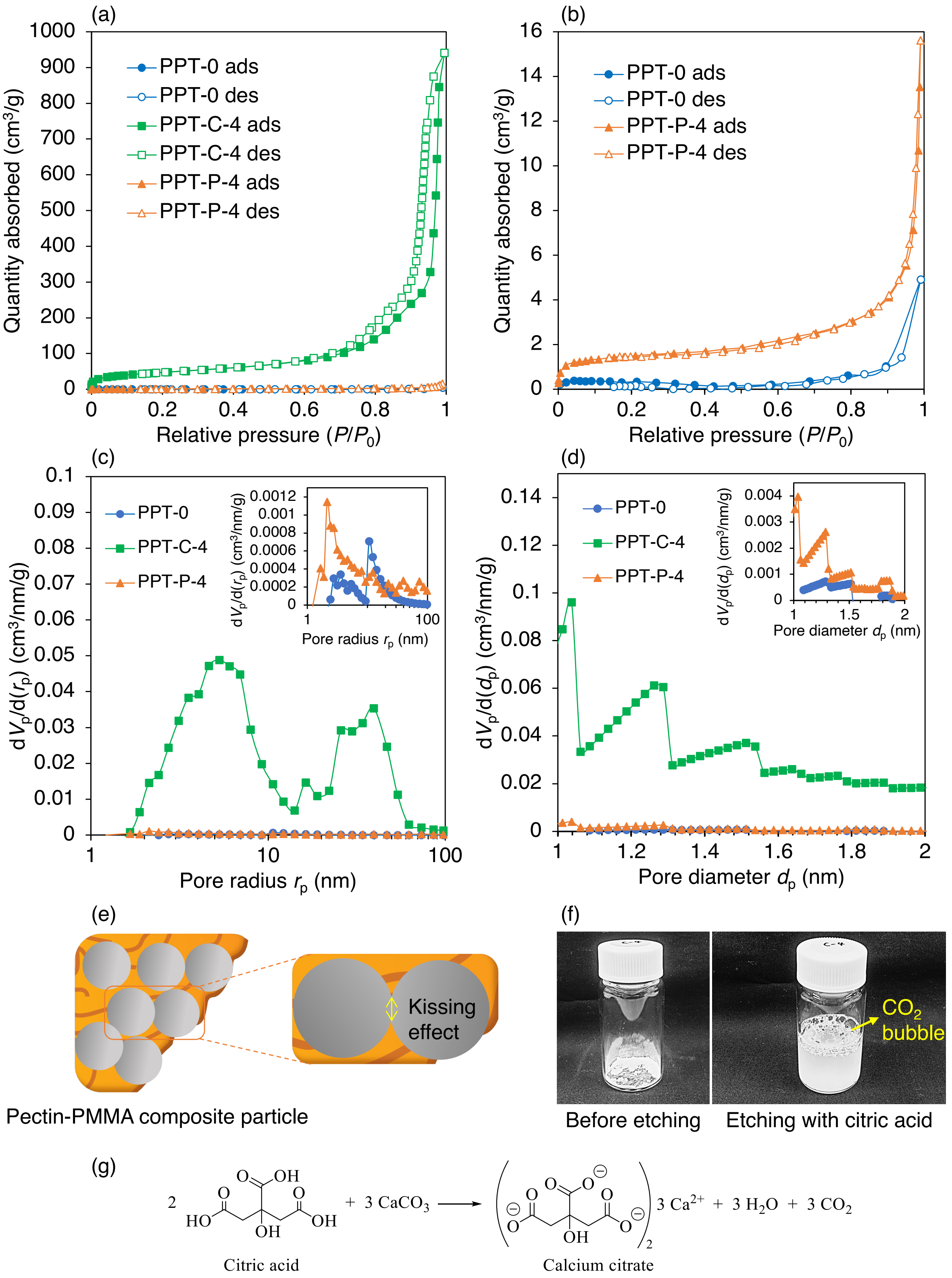

Figure 2.7: (a, b) N_2 adsorption-desorption isotherms of porous pectin particles. The pore size distribution of porous pectin particles was obtained using (c) the BJH method and (d) the HK method. (e) Illustration of the kissing effect of PMMA particles. (f) Pectin-$CaCO_3$ composite particles with a pectin/$CaCO_3$ mass ratio of 4 before etching (left) and while etching with citric acid (right). (g) Reaction between citric acid and $CaCO_3$ to produce CO_2 gas.

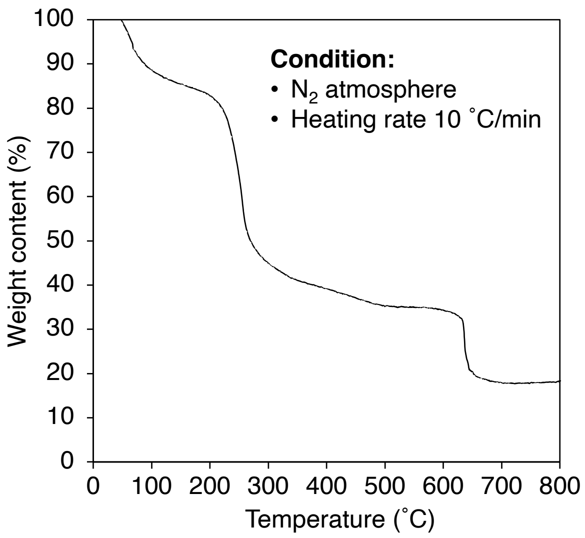

Figure 2.8: Thermogravimetric (TG) analysis diagram of pectin.

of the precursor solution, e.g., density, viscosity, and surface tension. Nukiyama et al. proposed that these properties were related to the droplet size during the spray drying process with two-fluid nozzles according to Equation 2.1,[107]

$$D_d = \frac{0.585}{V_a}\left(\frac{\sigma}{\rho_L}\right)^{0.5} + 53\left(\frac{\eta_L^2}{\sigma\rho_L}\right)^{0.225}\left(\frac{Q_L}{Q_A}\right)^{1.5} \tag{2.1}$$

where D_d is the average droplet size (µm), V_a is the liquid jet velocity (m s^{-1}), σ is the liquid surface tension (kg s^{-2}), ρ_L is the density of liquid (kg m^{-3}), η_L is the viscosity of the liquid (kg m^{-1}s^{-1}), Q_L is the liquid flow rate (m^3 s^{-1}), and Q_A is the carrier gas flow rate (m^3 s^{-1}). The droplet diameters, D_d, were calculated using Equation 2.1, and the results are presented in Table A.1. The presence of PMMA or $CaCO_3$ in the pectin solution effectively changed the precursor's density, viscosity, and surface tension, which affected the initial droplet size after atomization. The droplet from the precursor solution containing only pectin had D_d = 30.2 µm. For precursor solutions with a template/pectin ratio of 4, the droplet size of the solution containing $CaCO_3$ was 30.8 µm, which was smaller than the droplet size of the analogous solution containing PMMA (33.4 µm). Based on these results, we proposed the particle formation mechanisms described in Figure 2.9.

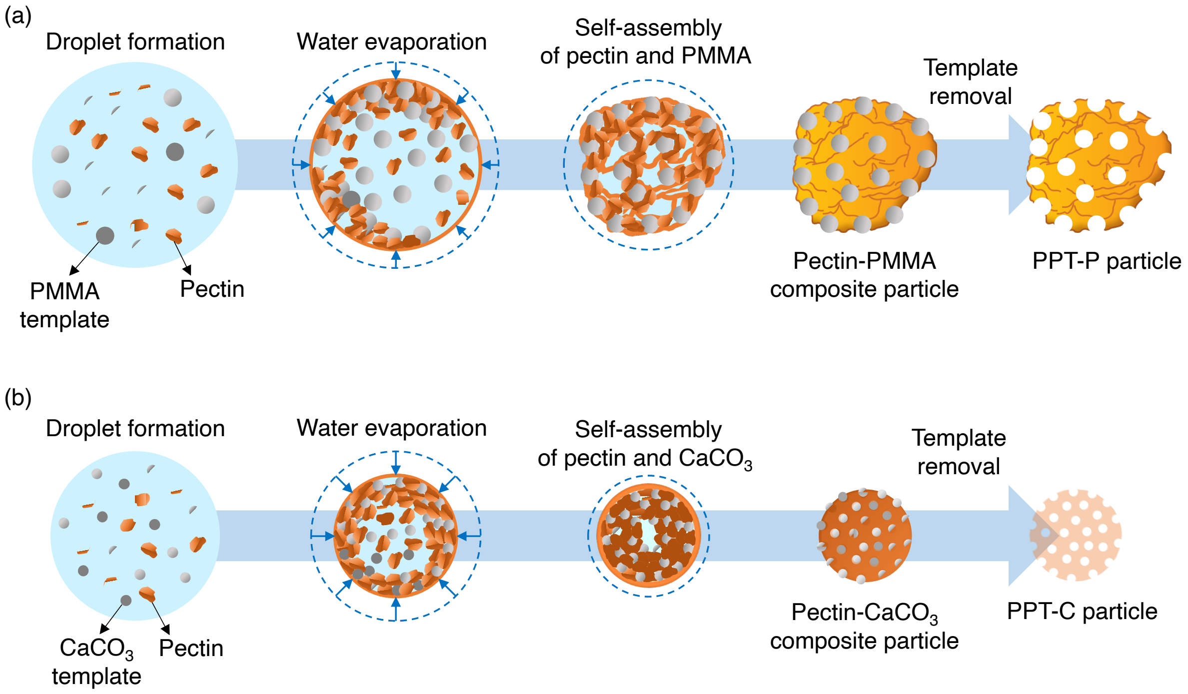

Figure 2.9: Porous pectin particle formation mechanisms using (a) PMMA templates or (b) $CaCO_3$ templates.

As illustrated in Figure 2.9, porous pectin particles were formed in a four-step process, including (i) droplet formation, (ii) water evaporation, (iii) self-assembly of pectin and template components in the droplet, and (iv) template removal. During atomization to generate droplets from the precursor in the first step, the initial droplets formed via spray drying have different sizes because of the initial difference in precursor properties, which depend on the template used. In the precursor containing $CaCO_3$ templates, the resulting droplets were smaller than those with PMMA templates. In the second step, some of the template particles move toward the inner surface of the droplet as the water begins to evaporate. In the third step, self-assembly between templates and pectin occurs via van der Waals, drag, electrostatic, and surface tension forces, which initiate the distribution of template and pectin inside the droplet during the drying process. Then, further evaporation of water and shrinkage in droplet diameter cause more trapped particles to accumulate on the surface. When the surface concentration of the template particles and pectin reaches its maximum value, a solid shell forms on the droplet surface. For small droplets (i.e., PPT-C), the droplet structure was stable, and the final obtained particles were spherical (similar to the initial shape of the droplet, except smaller in size). However, when the droplet size was large, as in the case of PPT-P, the drying was not completed under the same conditions, meaning that the interior was still wet. The droplet structure was also less stable, so under the drying gas, the difference in pressure inside and outside of the particles caused their shape to become abnormal, and a concave morphology was adopted. The instability of the droplets during the spray drying process was considered based on the Bond number theory described by Equation 2.2,[108]

$$\beta = \frac{\Delta\rho \times \alpha \times D_d^2}{\sigma} \tag{2.2}$$

where, β is the Bond number, $\Delta\rho$ is the differences in densities between the droplet and the surrounding fluid, α is the acceleration of the droplet moving during the drying process, σ is the surface tension of the precursor solution, and D_d is the average droplet size. In general, the closer β is to zero, the more stable the droplet, and the more capable it is of maintaining its spherical shape. Based on Equation 2.2, the value of the Bond number is directly proportional to the square of the average droplet size, indicating that changes in D_d dramatically affect the stability of the droplet. Therefore, when the droplets were large, the Bond numbers were also large, and indeed, the droplets became irregular in shape; when these droplets were dried, they formed particles with non-spherical morphologies. The SEM images of the porous pectin particles (Figure 2.2a-f) confirmed that the large droplet size in the PPT-P case was unstable, leading to non-spherical particles. These results supported our analysis regarding droplet stability based on Bond number theory. In addition, experimental data showing the change in the size of the porous particles (Figure 2.2g) confirmed that a large droplet size led to the formation of large porous particles, i.e., the size of PPT-P particles was greater than that of PPT-C particles. These results are consistent with previous reports demonstrated that the droplet size also affects the properties of the obtained porous particles.[106,109] The droplet diameter only influences the outer diameter and morphology of the particles. Moreover, the porous structure (i.e., pore sizes, shapes) is the result of the self-assembly of components during the drying process, and there is no relation to the droplet diameter. Furthermore, pectin is widely used for various applications, so understanding how to control the morphology and porous structure of pectin particles is crucial for advanced applications.

2.4 CONCLUSIONS

This report described the synthesis of meso-macroporous pectin particles using a template-assisted spray drying method involving two types of templates, i.e., PMMA and $CaCO_3$. Spectroscopic data (FT-IR) and ζ potential values indicated that porous structured particles were successfully prepared without impacting the inherent characteristics of pectin. The initial droplet size during the spray drying process influenced the morphology and size of the porous pectin particles. The obtained PPT-P particles (using PMMA templates) had wrinkled morphology, and the particle size varied from 5 to 8 μm when the mass ratio of template / pectin increased from 1 to 4. When $CaCO_3$ templates were used, the resulting PPT-C particles were spherical, and their size changed slightly from 3 to 4 μm as the template / pectin mass ratio increased from 1 to 4. The pores contributed to the increased specific surface area of the porous pectin particles compared with particles formed using only pectin (without a template). With a template / pectin mass ratio of 4, the PPT-C particles had a higher specific surface area (171.2 m^2 g^{-1}) than the PPT-P particles (5.4 m^2 g^{-1}). Overall, this study demonstrated the potential for using PMMA and $CaCO_3$ templates to control and design macroporous materials. With such incredible potential, appealing opportunities are awaiting porous pectin particles in the field of drug delivery systems. More specifically, further research is on-going in controlling the morphology and pore sizes of porous pectin particles and utilizing them in adsorption experiments of macromolecules (e.g., antibodies and enzymes) for a wide range of drug delivery applications.

3

Protein Adsorption Capacity of Porous Pectin Particles

There has been much interest in developing protein adsorbents using nanostructured particles, which can be engineered porous materials with fine control of the surface and pore structures. A significant challenge in designing porous adsorbents is the high percentage of available binding sites in the pores owing to their large surface areas and interconnected pore networks. In this study, continuing the idea of using porous materials derived from natural polymers toward the goal of sustainable development, porous pectin particles are reported. The template-assisted spray drying method using calcium carbonate ($CaCO_3$) as a template for pore formation was applied to prepare porous pectin particles. The specific surface area was controlled from 177.0 to 222.3 $m^2\ g^{-1}$ by adjusting the $CaCO_3$ concentration. In addition, the effects of a macroporous structure, the specific surface area, and an interconnected pore network on the protein (lysozyme) adsorption capacity and adsorption mechanism were investigated. All porous pectin particles performed rapid adsorption ($\sim$65% total capacity within 5 min) and high adsorption capacity, increasing from 1543 to the highest value of 2621 mg

g^{-1}. The results are attributed to the high percentage of available binding sites located in the macropores owing to their large surface areas and interconnected pore networks. The macroporous particles obtained in this study showed a higher adsorption capacity (2621 mg g^{-1}) for lysozyme than other adsorbents. Moreover, the rapid uptake and high performance of this material show its potential as an advanced adsorbent for various macromolecules in the food and pharmaceutical fields.

---

published in part in *ACS Appl. Mater. Interfaces* 2022, 14, 14435–14446

3.1 INTRODUCTION

As an indispensable part of biomacromolecules, proteins play essential roles in fundamental biological processes and have an important place in the biotechnological and biopharmaceutical industries.[110,111] Accordingly, it is necessary to develop high-productivity adsorbents to transport highly reliable proteins for human use.[112] Nanostructured particles, especially porous particles, are efficient adsorbents owing to the good accessibility of the active sites.[46] In recent years, application of conventional porous particles such as porous silica and carbon as adsorbents for small molecules has been well established.[113,114,115] However, their utilization for macromolecular organic compounds, such as drugs, proteins, and antibiotic residues, is still minimal because they mainly contain micropores and mesopores.[116,117] The poor accessibility of the binding sites in the inner micropores of these materials and the longer contact times that are often required to enable large molecules to transfer lead to a low processing rate.[118,119] Therefore, it is necessary to develop an efficient protein adsorbent with large pores that possess more active sites to enhance protein interaction performance.

To overcome the above drawbacks, recent interest in adsorption, separation, and controlled release of large molecules has been combined with advanced synthesis techniques to readily introduce macropores (pore diameters larger than 50 nm) into particles.[120,121,122] Although macroporous materials typically have lower specific surface area than mesoporous materials, macropores have the potential to improve the accessibility of reactants (especially macromolecular organic compounds) to the active sites in these materials.[123,124] The adsorption capacity and selectivity are known to depend on the pore sizes and pore network of the adsorbent. Thus, the differences in the dimensions and interconnected channels can be used to accomplish adsorption of proteins. Several research groups have demonstrated many approaches that use this concept, such as the double emulsion method,[125,126] seeded polymerization,[127,128] colloidal templating,[129] microfluidic techniques,[130,131] and other methods.[132,133] For instance, Pavel and co-workers[132] recently prepared hierarchical porous materials that combine mesopores with macropores (average pore sizes of 9 and 200 nm, respectively) by a sol–gel method from a silica precursor and a dispersion of solid lipid nanoparticles in a micelle phase. They found that adsorption of dimers or monomers of an enzyme (small size) preferentially occurred in the mesopores, while the tetrameric (larger size) form adsorbed in the macropores. However, most of the aforementioned methods require additional chemicals, such as surfactants, complicated processes to generate pores, and sophisticated equipment. To overcome the above disadvantages, the development of a simple method for the synthesis of high porosity particles has been researched and established. Aerosol methods, such as the spray process, are efficient and useful methods to prepare porous particles.[134,43,135,136] Particles prepared by the spray process are continuously and rapidly formed in a limited number of steps and generate low waste. Rahmatika et al.[79] reported cellulose-nanofiber-loaded macroporous silica particles fabricated by tuning the macropores of silica particles to achieve unrivaled protein adsorption capacity. By modifying macroporous silica particles with different pore sizes, the optimum macropore size successfully enhanced the adsorption capacity owing to the improved interconnectivity between the pore networks with an abundance of accessible binding sites. From that issue, the importance of macropores to the performance of large molecules of materials is remarkably impressive for further studies in practical application. Nevertheless, tailoring the macroporous structure to include high specific surface area with an interconnected pore network while selecting a material with excellent properties according to the goal of sustainable development remains a challenge.

For many applications, especially in drug-delivery systems and the food industry, the choice of the raw materials is important for sustainable particulate material development. Among the potential adsorbents, natural polymer-based materials are the most promising because they are biocompatible and have a low environmental effect while demonstrating high strength, stiffness, and chemical resistance.[120,45] Pectin is a complex polysaccharide consisting mainly of esterified D-galacturonic acid in an α-(1-4) chain present in every plant's primary cell wall and center lamellae grown from the ground, and has various bioactivities.[90] It is appropriate for synthesizing a sustainable material for industrial scale-up as it has different properties, including gelling ability, viscosity, and cation binding properties between cation and non-esterified galacturonic acid units. Recently, our group reported fabrication of macroporous particles from pectin by the template-assisted spray drying method for the first time.[137] The results showed the potential of using a poly(methyl methacrylate) or a $CaCO_3$ template to tailor macroporous materials. Importantly, the porous pectin particles obtained using the $CaCO_3$ template had extremely high specific surface area, which is beneficial for providing active binding sites for protein adsorption. However, application of macroporous pectin particles as an adsorbent for proteins has not been reported.

In this study, we investigated the effectiveness of macroporous pectin particles with different specific surface areas to enhance the protein (lysozyme as a model) adsorption performance. In addition, we elucidated the lysozyme-adsorption mechanism by calculating the adsorption kinetics and isotherm parameters.

3.2 EXPERIMENTAL SECTION

3.2.1 Materials

Pectin was purchased from Herbstreith & Fox GmbH & Co. KG Pektin-Fabriken (Neuenbürg, Germany). $CaCO_3$ (30 wt.% in aqueous solution) with the average size of 86 nm (from the diameter measurement of more than 300 particles from the SEM images) was obtained from Shiraishi Calcium (Osaka, Japan). Citric acid was purchased from Sigma-Aldrich (Osaka, Japan). The model protein (lysozyme) was purchased from MP Biomedicals (Solon, OH). All of the chemicals and solvents for the experiments were used as received without further purification.

3.2.2 Preparation of the porous pectin particles

Precursor preparation

First, the precursor solution, including raw pectin and $CaCO_3$ as the template, was prepared in deionized (DI) water as the dispersant medium. The pectin concentration in the precursor solutions was controlled at 1.0 wt.%, and $CaCO_3$ was used in weight ratios of 4, 8, and 12 relative to the weight of pectin. An ultrasonic device (T 10 basic ULTRA-TURRAX S004, IKA, Japan) was then used to homogenize the aqueous precursor with a rotation speed of 12,800 rpm for 30 min to disperse the components. The precursor solution contents are given in Table 3.1.

Table 3.1: Precursor concentrations of various porous pectin particles (DI water was used as the solvent).

Sample	Pectin (wt.%)	$CaCO_3$ (wt.%)	Weight ratio of pectin:$CaCO_3$	Total weight of the precursor solution (g)
PPT-0	1.0	-	1:0	50.0
PPT-4	1.0	4.0	1:4	50.0
PPT-8	1.0	8.0	1:8	50.0
PPT-12	1.0	12.0	1:12	50.0

Template-assisted spray drying followed by template removal

The porous pectin particles were prepared by template-assisted spray drying, followed by a chemical removal process.[137] The method is shown in Figure 3.1a. A mini spray-dryer (BÜCHI B-290, Flawil, Switzerland) was used with an external two-fluid mixing nozzle with a 0.7 mm liquid orifice diameter and a 1.5 mm gas orifice diameter. The feed rate of the precursor solutions was 3 mL min^{-1}. During this process, the inlet air temperature was 150 °C. The spray gas-flow rate and aspiration rate were set to 357 L h^{-1} and 37,000 L h^{-1}, respectively. Spray-dried pectin only (PPT-0) as a control sample was prepared by the same method for comparison with the porous pectin particles. The dried composite particles were then immersed and washed to generate the porous structures. The composite pectin–$CaCO_3$ particles were placed in 10.0 wt.% citric acid aqueous solution and stirred for 15 min to remove the $CaCO_3$ template. They were then centrifuged at 8000 rpm for 5 min and washed thoroughly with ethanol. After washing, the particles were dried in an oven at 80 °C for 1 h to obtain the porous particles. The porous samples are labeled PPT-X, where X is the weight ratio of the template particles to pectin (X = 0, 4, 8, and 12).

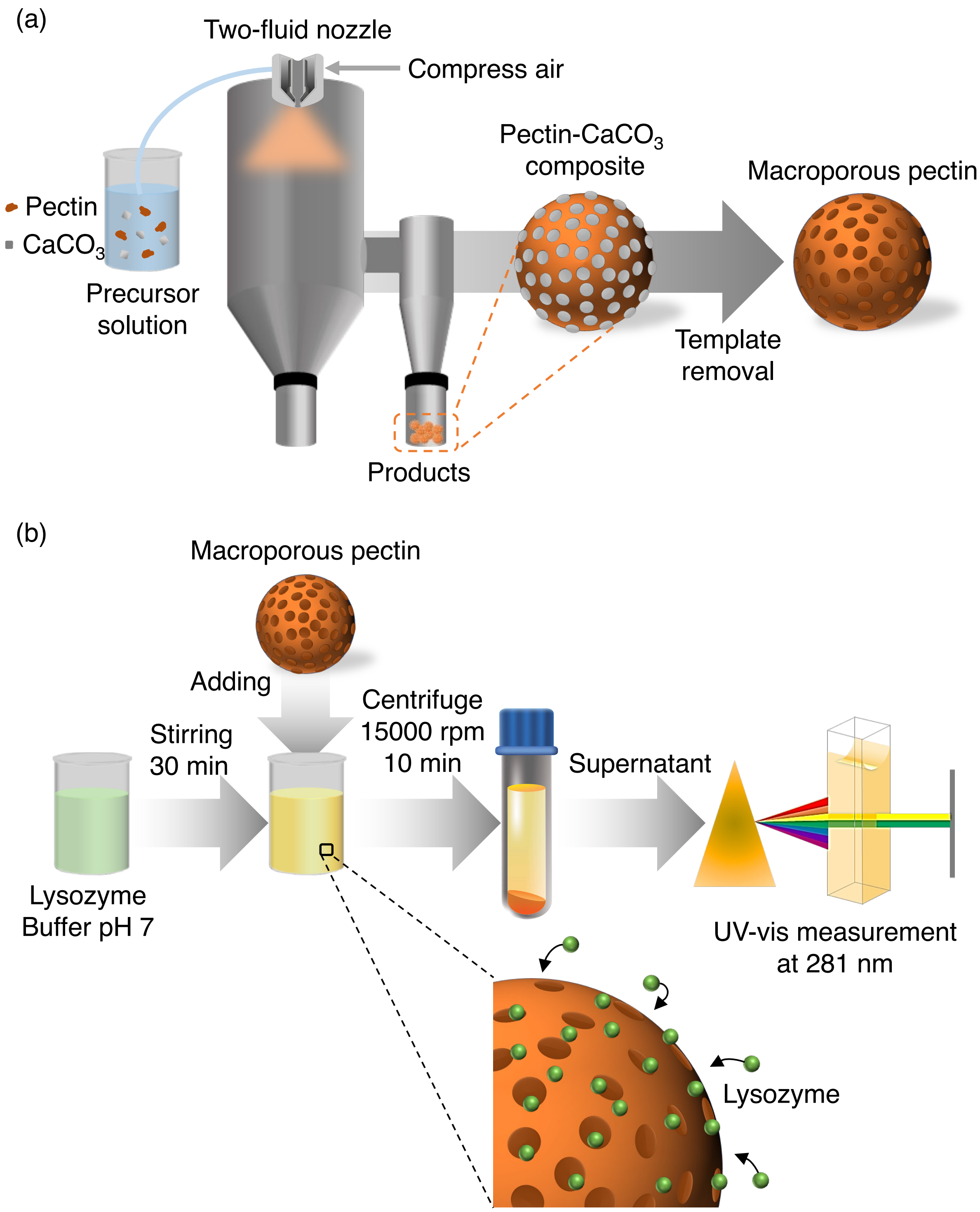

Figure 3.1: (a) Procedure for preparing the porous pectin particles. The precursor solution containing pectin and $CaCO_3$ was spray-dried to give pectin–$CaCO_3$ composite particles. The pectin–$CaCO_3$ composite particles were then collected for $CaCO_3$ removal to obtain porous pectin particles. (b) Application of the porous pectin particles to lysozyme adsorption. The lysozyme solution in pH 7 buffer was prepared, and then the porous pectin particles were added to the solution. After each determined time, a sample of the solution was centrifuged. The supernatant fraction was then subjected to UV–Vis measurement at 281 nm to determine the adsorbed lysozyme amount.

Characterization of the porous pectin particles

The morphologies of the particles were investigated by scanning electron microscopy (SEM) (S-5200, Hitachi Ltd., Tokyo, Japan). The cross-sectional SEM images were acquired with a Xe^+ plasma focused ion beam (PFIB) system using an FEI Helios PFIB Dual Beam FIB-SEM facility. The specific surface areas of the samples were determined from the nitrogen adsorption–desorption isotherms obtained at 77 K using BELSORP-max (BEL Japan, Osaka, Japan). The specific surface areas were calculated by the Brunauer–Emmett–Teller (BET) method. The pore volume and pore-size distribution were determined by the Barrett–Joyner–Halenda (BJH) and Horvath–Kawazoe (HK) methods. The zeta potential of the particles was determined with a Zetasizer Nano ZS (Malvern Instrument Inc., London, UK).

Evaluation of the equilibrium adsorption performance

To investigate the adsorption capacity of the prepared porous pectin, lysozyme (isoelectric point (pI) of 10.5 and dimensions of 4.5 nm × 3.0 nm × 3.0 nm)[79] was used as a model molecule. The procedure of the adsorption experiments is shown in Figure 3.1b. An aqueous lysozyme solution with a concentration of 0.4 mg mL^{-1} and a pH value of 7 was prepared using phosphate buffer. To test the static adsorption performance, 10.0 mg of the prepared porous pectin was soaked in 50.0 mL of the aqueous lysozyme solution. The mixed solution was then stirred at 25 °C for 2 h. A 5.0 mL sample was periodically withdrawn and then centrifuged (15,000 rpm for 10 min). The calibration curve of the lysozyme solution was prepared from 6.25×10^{-3} to 1.5 mg mL^{-1}. All of the changes in the absorption intensity of the supernatant were measured at 281 nm with an ultraviolet–visible (UV–Vis) spectrophotometer (UV-2450, Shimadzu, Japan) from 250 to 350 nm at 25 °C. The following equation was used to calculate the adsorption capacities of all of the adsorbents:

$$Q_t = \frac{(C_0 - C_t)V}{m} \tag{3.1}$$

where Q_t is the adsorption capacity of the adsorbent at time t (mg protein / g adsorbent), C_0 is the initial protein concentration, C_t is the protein concentration at time t, which was calculated from the calibration curve, m (g) is the weight of the adsorbent, and V (mL) is the volume of the protein solution. All tests were performed in triplicate.

A further investigation of the maximum lysozyme uptake capacities of PPT-12 at various lysozyme concentrations (0.1, 0.2, 0.4, 0.9, 1.1, and 1.3 mg $\mathrm{mL^{-1}}$) was performed for use in isotherm fitting. For all of the materials, the batch adsorption experiments were monitored kinetically and maintained for a period of time to reach equilibrium.

3.3 RESULTS AND DISCUSSION

3.3.1 Preparation of the porous pectin particles

The morphologies of the prepared dense pectin particles (PPT-0) and porous pectin particles (PPT-4, PPT-8, and PPT-12) are shown in Figure 3.2. Spherical particles with a smooth surface were obtained by spray drying the precursor solution containing only pectin (PPT-0) (Figure 3.2a). After spray drying pectin with $CaCO_3$ template, the pectin-$CaCO_3$ composite particles were obtained (Figure B.1). Subsequently, porous structures with spherical morphology were successfully introduced into the pectin particles after the chemical removal process of the $CaCO_3$ template with citric acid (Figure 3.2b–d). Another experiment was conducted using HCl to remove the $CaCO_3$ template. However, the porous particles appeared with large pores and broken particles were obtained (Figure B.2). This result was in stark contrast to the use of citric acid. In addition, citric acid is environmentally friendly because it can be extracted from nature, and they are also used in the production of foods such as confectionery because they are not harmful to the human body. Based on our survey results and the benefits of citric acid, the citric acid solution was chosen for this study. To confirm the removal of $CaCO_3$, FT-IR measurements of the pectin particles before and after removing $CaCO_3$ were conducted (Figure B.3). Along with that, we measured the spectra of pectin, and $CaCO_3$. Based on the results, the characteristic signals of $CaCO_3$ were detected in the pectin-$CaCO_3$ composite particles. However, after etching treatment with citric acid, the characteristic signals of $CaCO_3$ no longer appeared in the porous pectin samples. The FT-IR spectra results shown in Figure B.3 indicated that the framework of the porous pectin particles was made from pectin, and the pores were formed from $CaCO_3$ removal. These results are similar to the porous pectin particles obtained in a previous study.[137] By comparing the porous particles with various $CaCO_3$ concentrations, it was found that the number of pores increased proportionally with increasing concentration of the $CaCO_3$ template (Figure B.4). This shows that it is possible to control the pore volume by varying the $CaCO_3$ concentration. Moreover, calcium ions can form an egg-box model with pectin.[138,139] This structure can be described as two antiparallel chains that conjugate with calcium ions and further aggregate laterally (Figure B.5). This phenomenon contributes to the increased stability of these porous particles, specifically by reducing the water solubility (the detailed calculation is given in the Appendix B, Figure B.6).[140] Additionally, the calcium ion contents of porous pectin particles were determined by the ICP-AES method. The results showed that the presence of calcium ions in the porous pectin particles of PPT-4, PPT-8, and PPT-12 were 18, 28, and 30 wt.%, respectively (the detailed in the Appendix B, Figure B.7). From the aforementioned results, we found that $CaCO_3$ plays two essential roles in formation of porous pectin particles: (1) as a template to prepare the porous structure in the particles and (2) the calcium ions formed after chemical removal of the template stabilize the porous structure through the egg-box model.

The structural characteristics of the inside of the nonporous and porous pectin particles with weight ratios of $CaCO_3$ to pectin of 4, 8, and 12 were investigated in detail (Figure 3.3). The cross-sectional SEM images of the nonporous pectin particles exposed the inner structure without the pores, which is consistent with their observed SEM images above. Before $CaCO_3$ templates removal, the cross-sectional SEM images of pectin-$CaCO_3$ composite particles showed the even distribution of $CaCO_3$ inside the particles (Figure B.8). The porous pectin particles revealed that the internal structures of the particles with numerous pores formed densely interconnected pore networks. These results indicated the effectiveness of the pores formation of chemical etching processes

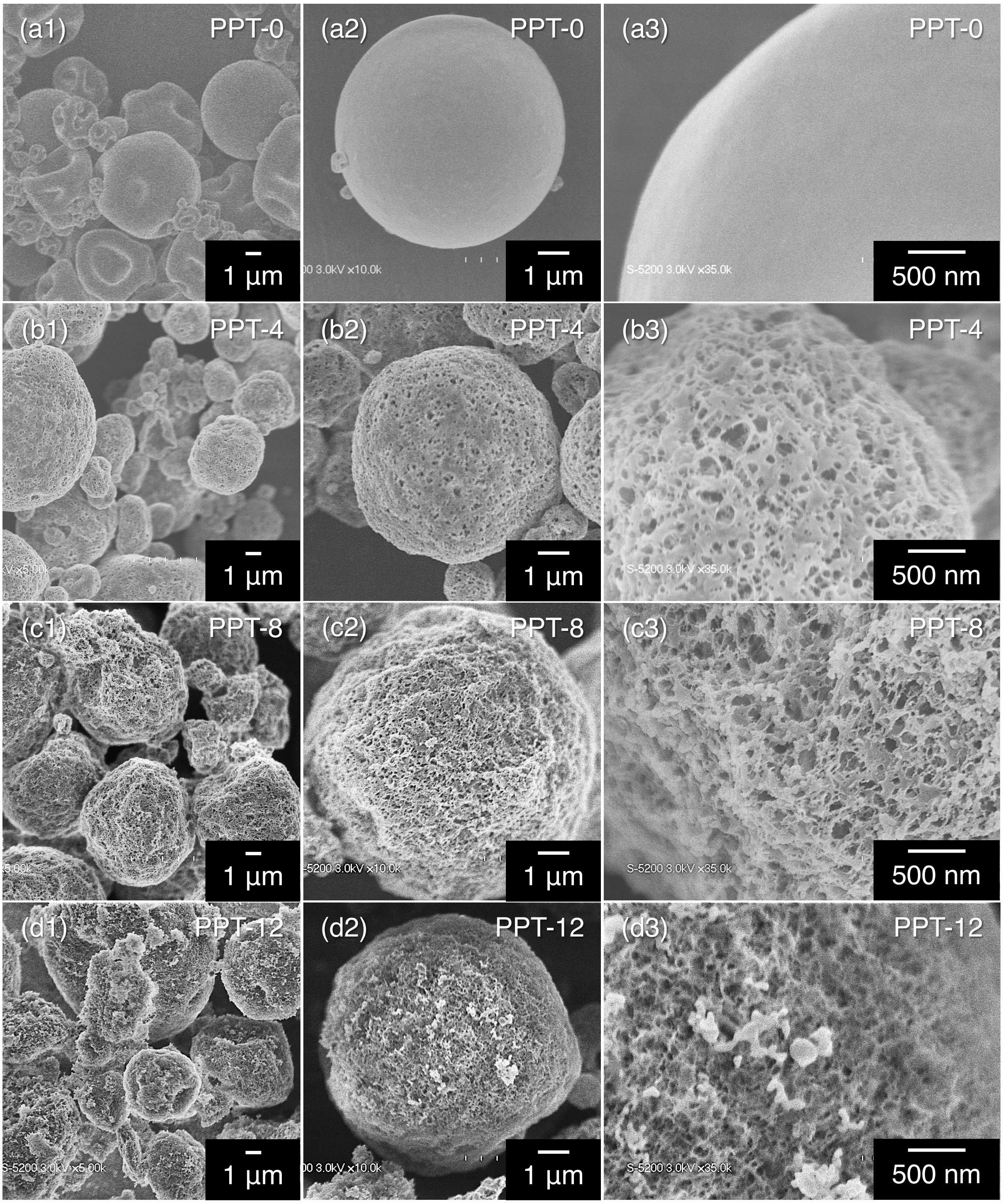

Figure 3.2: SEM images of porous pectin particles with weight ratios of $CaCO_3$ to pectin of (a1)–(a3) 0, (b1)–(b3) 4, (c1)–(c3) 8, and (d1)–(d3) 12. The images at different magnifications are classified into three categories: (1) images of many particles at magnification of ×5.0k, (2) images of one particle at magnification of ×10.0k, and (3) images of the surface of a particle at magnification of ×35.0k.

to remove the template. As observed in the high magnification images, the shape and size of the pores were consistent with the $CaCO_3$ particles used as the template. The average pore diameter (~80 nm) was almost identical to the size of the $CaCO_3$ particles (80 nm). Moreover, larger pores formed owing to the interlaced arrangement of the $CaCO_3$ particles inside the pectin particles. This interconnected porous structure is important for adsorption because the molecules can move freely between adjacent channels. The influence of this structure on the diffusion behavior has already been examined through the movement of individual molecules in the channel structures using single-molecule tracking.[141,142] Consequently, the interconnected pore network can enhance mass transfer of liquid and improve the processing efficiency, which are favorable for applications in the field of adsorbents.

3.3.2 Effect of the $CaCO_3$ concentration on the specific surface area of the porous pectin particles

To elucidate the surface physicochemical properties of the porous pectin particles and the effect of the $CaCO_3$ concentration on the specific surface area, nitrogen adsorption–desorption tests of PPT-0, PPT-4, PPT-8, and PPT-12 were performed (Figure 3.4 and Table 3.2). As shown in Figure 3.4a, the N_2 adsorption–desorption isotherm of the PPT-0 particles was type II, corresponding to a nonporous structure.[137,101,95] All of the PPT-4, PPT-8, and PPT-12 porous particles showed a combination of type II and IV adsorption isotherm curves. According to the IUPAC definition, they have typical meso- and macroporous structures.[137,101] Moreover, the hysteresis loops of all of the porous pectin samples were H2 type, indicating that they had disordered and wide pore-size distributions. The PPT-4 sample characteristics were similar to those reported previously,[137] showing the reproducibility of the experiment to produce porous pectin particles. As can be seen from Figure 3.4b, the specific surface areas of the PPT-4, PPT-8, and PPT-12 porous particles were significantly larger than that of PPT-0. This is attributed to an increase of the total pore volume owing to formation of more pores with increasing weight ratio of $CaCO_3$ to pectin.

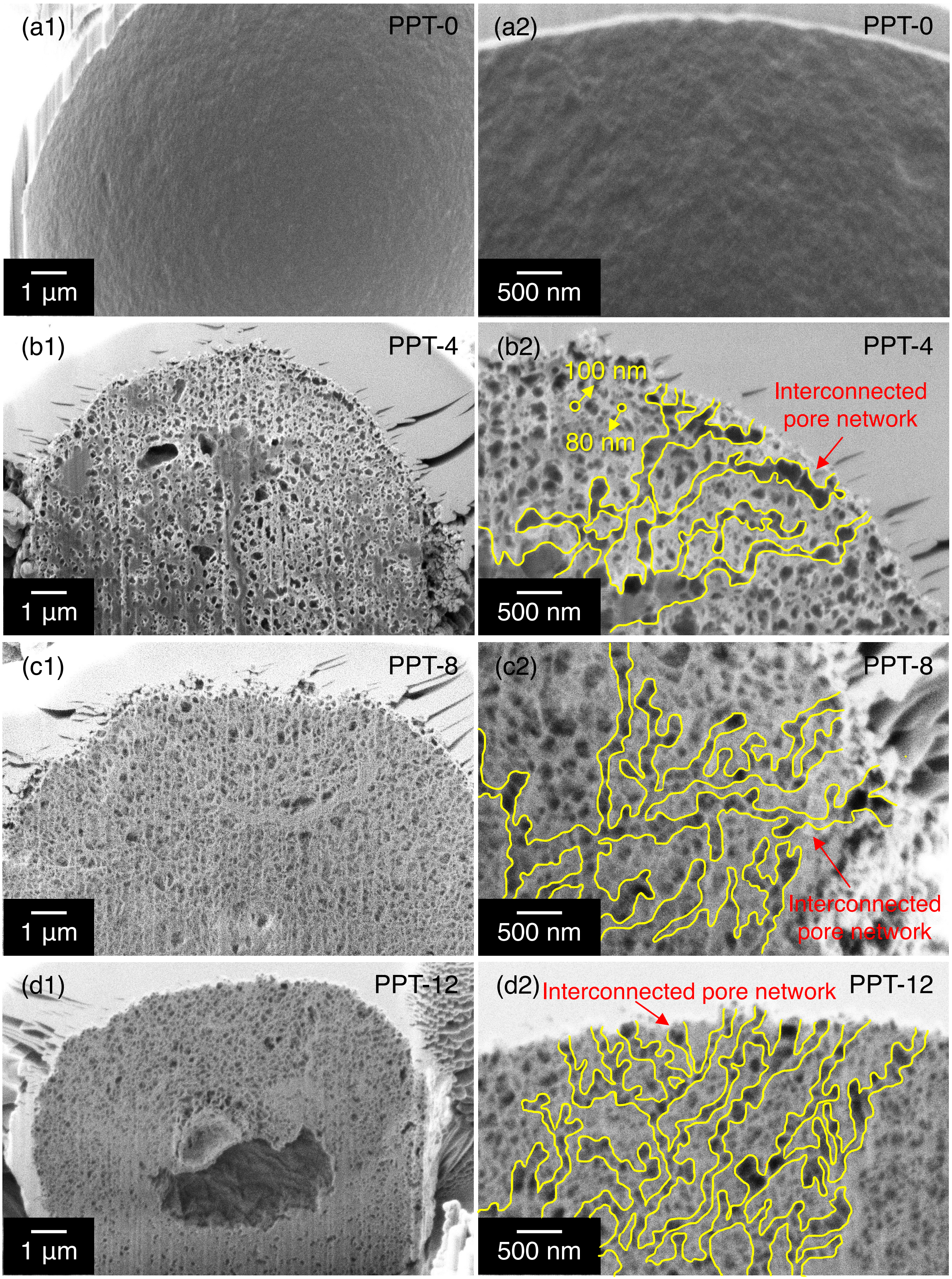

Figure 3.3: Cross-sectional SEM images of (a1)–(a2) nonporous pectin particles and porous pectin particles with weight ratios of $CaCO_3$ to pectin of (b1)–(b2) 4, (c1)–(c2) 8, and (d1)–(d2) 12 at different magnifications. (a1), (b1), (c1), and (d1) are at low magnification of ×10.0k and (a2), (b2), (c2), and (d2) are at high magnification of ×25.0k. The regions marked in yellow in the high-magnification images are the interconnected pore networks.

Table 3.2: Characteristics of the macroporous pectin particles (different superscript letters indicate a significant difference ($p < 0.05$) compared with the other samples as assessed by two-tailed Student's t-tests).

Sample	Specific surface area (m^2 g^{-1})	$V_{micropore}$ (cm^3 g^{-1})	$V_{mesopore}$ (cm^3 g^{-1})	$V_{macropore}$ (cm^3 g^{-1})	Total pore volume (cm^3 g^{-1})
PPT-0	1.5	0.00055^a	0.0047^a	0.0023^a	0.0075
PPT-4	177.0	0.065^b	0.39^b	0.78^b	1.2
PPT-8	193.2	0.072^b	0.56^b	$1.6^{b,\,c}$	2.2
PPT-12	222.3	0.082^c	0.59^b	1.9^c	2.5

More specific aspects of the pore-size distributions of the porous pectin particles were evaluated to determine the effect of the template on pore formation. The micropore-size distribution was investigated in the 1–2 nm range by the HK method (Figure 3.4c), and the meso-/macropore-size distribution was analyzed in the range 2–200 nm by the BJH method (Figure 3.4d). For all of the porous pectin particles, the wide pore-size distribution in the meso-/macropore range with an evenly distributed pore volume indicated that they possessed highly interconnected pore networks with open macropores in the size range 60–120 nm. Furthermore, based on the data in Table 3.2, increasing the $CaCO_3$ concentration resulted in significant increases of the micropore volume (from 0.065 to 0.082 cm^3 g^{-1}), mesopore volume (from 0.39 to 0.59 cm^3 g^{-1}), and macropore volume (from 0.78 to 1.9 cm^3 g^{-1}). These results remarkably contributed to the high specific surface areas of the porous pectin particles, namely, the specific surface areas of 177.0, 193.2, and 222.3 m^2 g^{-1} for PPT-4, PPT-8, and PPT-12, respectively. The significant increases in the micropore and macropore volumes of the PPT-12 particles led to an increase in the specific surface area (the specific surface area was about 150 times higher than that of the nonporous PPT-0 particles (1.5 m^2 g^{-1})). The improvement of the specific surface area combined with the abundance of accessible binding sites of the mesopores, macropores, and interconnected pore network can promote the capacity for protein adsorption when the porous pectin particles are applied as an adsorbent.

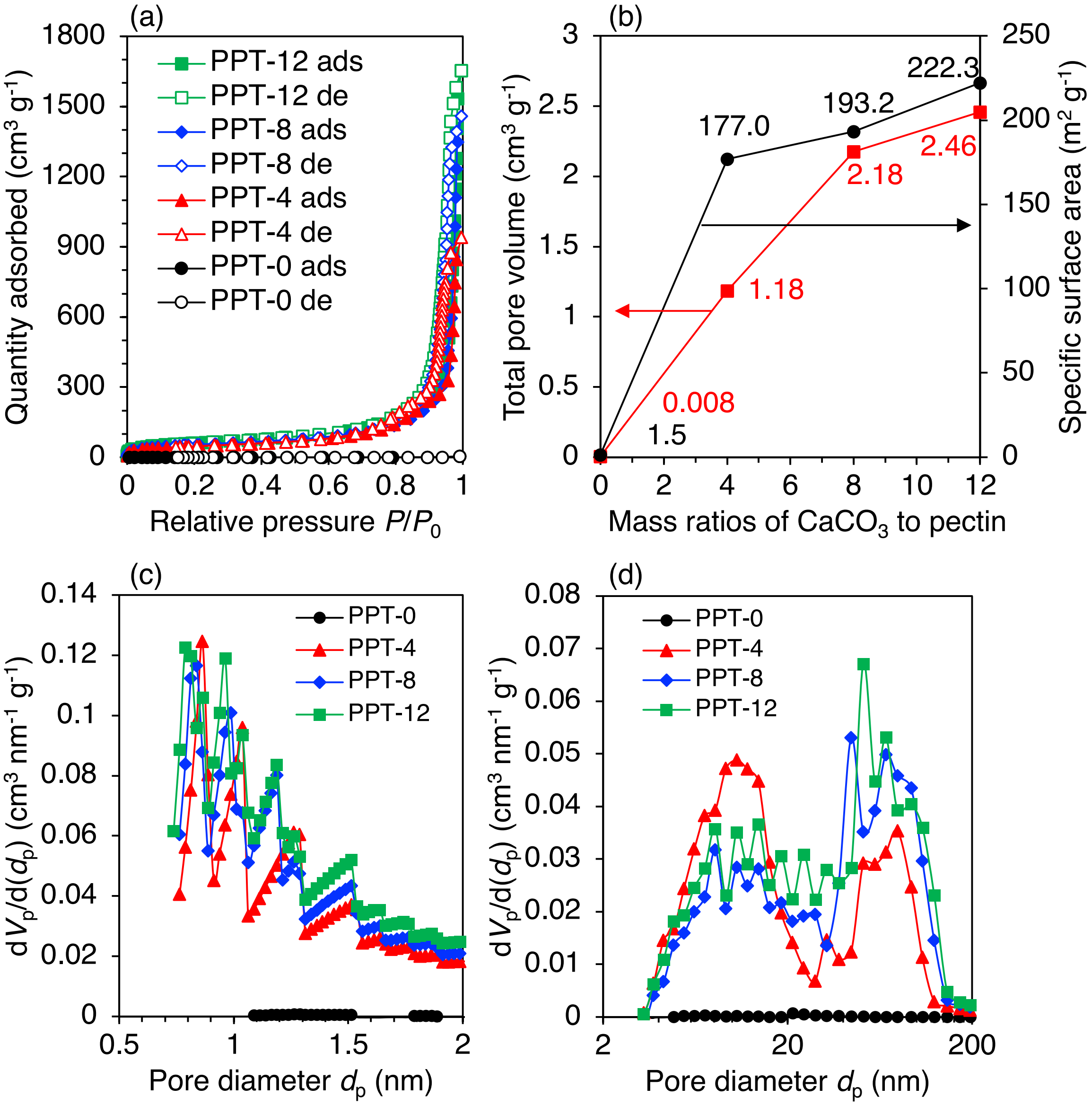

Figure 3.4: (a) Nitrogen adsorption (ads)–desorption (de) isotherms. (b) Relationships between the specific surface area and total pore volume and the $CaCO_3$ concentration as a template. (c) and (d) Micropore-, mesopore-, and macropore-size distributions of the porous pectin particles fabricated with different $CaCO_3$ concentrations.

3.3.3 Elaboration of the lysozyme adsorption system

Adsorption kinetics

Lysozyme adsorption on the porous pectin particles was carried out in batch experiments. Initially, a calibration absorbance–concentration curve was prepared between 6.25×10^{-3} and 1.5 mg mL^{-1} lysozyme concentration (correlation factor $R^2 = 0.9999$, Figure B.9). The concentration of adsorbed lysozyme was analyzed by measuring the absorbance of lysozyme at 281 nm using a UV–vis spectrophotometer, and the adsorption capacities (mg lysozyme/g adsorbent) were calculated by Equation 3.1. Proteins are charged molecules, and their overall charge depends on their pI value, which significantly influences their adsorption on adsorbent surfaces. Because lysozyme has a pI value of 10.5, the protein molecules are mostly neutral in charge at this point. At pH lower than the pI value (e.g., pH 7), the amine groups of lysozyme are protonated and it turns into a positively charged protein, while pectin possesses negative charge owing to the presence of carboxyl (–COOH) groups (Figure 3.5a). Therefore, lysozyme can absorb on the adsorbent through electrostatic interaction between the negatively charged pectin particles and positively charged protein molecules.

The pore structures of the pectin particles allow proteins to adsorb in the macropores; however, protein adsorption in the micropores is limited. We investigated the effect of the specific surface area/pore size on the adsorption capacity for PPT-4, PPT-8, and PPT-12. Although all of the particles had almost the same zeta potential value (Figure 3.5a), there were apparent differences in the adsorption capacities of the particles (Figure 3.5b). This emphasized the efficient adsorption performance of these adsorbents. This efficiency is not only caused by electrostatic interaction acting as the driving force, but the porous structure also plays a role in enhancing protein diffusion to the binding sites. From Figure 3.5b, PPT-12 showed the best adsorption performance. A macroporous structure with a high surface area can enhance protein adsorption and promote the diffusion process, because pectin particles possess a high percentage of available active binding sites located within the macropores owing to their large surface areas and interconnected pore networks. This confirmed the success of our design strategy, which was based on an interconnected porous framework containing macropores. Moreover, during lysozyme absorption experiments of porous pectin particles, the calcium ions were released into the aqueous solution (Figure B.10). These released calcium ions remained soluble in the solution. To confirm the interaction of calcium ions and lysozyme, an additional experiment was conducted by mixing calcium ions with lysozyme. The result showed that there is no sedimentation of calcium ions with lysozyme. Therefore, calcium ions did not affect the lysozyme adsorption performance determined by our method.

To study and compare the kinetic characteristics of the PPT-4, PPT8, and PPT-12 porous pectin particles, theoretical kinetic models such as the pseudo-first-order, pseudo-second-order, and intraparticle-diffusion models were used to fit the experimental data. The lysozyme adsorption capacity against time and pseudo-first-order kinetic, pseudo-second-order kinetic, and intraparticle-diffusion model plots for PPT-4, PPT-8, and PPT-12 are shown in Figure 3.5b–d and Figure B.11, and the kinetic parameters calculated by linear regression are given in Table 3.3. The experimental data fitted the pseudo-second-order kinetic model with high correlation coefficients for all of the adsorbents ($R^2 = 0.9813$ for PPT-4, $R^2 = 0.9992$ for PPT-8, and $R^2 = 0.9983$ for PPT-12). This indicates that the active sites dominate the adsorption process rather than other mass-transfer processes, and that the rate-limiting adsorption step is likely to be chemisorption (Figure 3.5c).[143,48] The equilibrium adsorption capacities of PPT-4, PPT-8, and PPT-12 were 1543, 2021, and 2621 mg g^{-1}, respectively (Figure 3.5b and Table 3.3), which were similar to the adsorption capacity at equilibrium (Q_e) values obtained from the pseudo-second-order kinetic model (1667, 2067, and 2683 mg g^{-1}). The kinetic study revealed that the macropores increased both the lysozyme uptake capacity and adsorption rate. In the case of the adsorption rate, ~65% of the total adsorption capacity of the porous pectin particles was reached in 5 min, and the remaining ~35% adsorption capacity was achieved in the slow intraparticle-diffusion step (Figure 3.5d). The lysozyme adsorption process is schematically illustrated in Figure 3.6. Initially, lysozyme adsorbs on the external surface of the pectin particle. Thereafter, macropore diffusion occurs and lysozyme penetrates the macropores and adsorbs on the binding sites within the macropores. The protein molecules then further diffuse into the binding sites of the mesopore regions. Comparing the rate constants of the diffusive steps in the macropores (Table 3.3), the intraparticle-diffusion rate constant (k_d) values were different, indicating that the macroporous diffusion and intraparticle diffusion steps were significantly affected. These results demonstrate the success of our strategy, which was based on the concept of implementing a macroporous structure with high surface area. This statement is shown in detail by Figure B.12 in Appendix B. Figure B.12 demonstrated the relationship between lysozyme adsorption capacity and physical characterizations such as specific surface area and macropore volume. By controlling the concentration of $CaCO_3$, the properties of the porous pectin particles were also adjusted to enhance the protein adsorption capacity. These are important characteristics for fast and efficient separation in chromatographic and adsorption applications.

Table 3.3: Pseudo-first-order, pseudo-second-order, and Weber–Morris diffusion model parameters for the porous pectin particles.

		Pseudo-first-order		Pseudo-second-order		Macropore-diffusion	
Sample	Q_e exp (mg g^{-1})	Q_e (mg g^{-1})	R^2	Q_e (mg g^{-1})	R^2	$k_d{}^*$ (mg g^{-1} min$^{-0.5}$)	R^2
PPT-4	1543	578	0.7528	1667	0.9813	69.3	0.8176
PPT-8	2021	735	0.9043	2067	0.9992	114.0	0.9022
PPT-12	2621	903	0.9460	2683	0.9983	148.1	0.8773

* Calculated based on the macropore-diffusion stage shown in Figure 3.5d.

Adsorption isotherms

A series of exposure time experiments for the lysozyme adsorption process was performed at 25 °C for different initial lysozyme concentrations (0.1–1.3 mg mL^{-1}), and the results are shown in Figure 3.7a. For low initial lysozyme concentration (0.1–0.4 mg mL^{-1}), the equilibration time was relatively short (~5 min). However, higher initial lysozyme concentrations (0.9–1.3 mg mL^{-1}) required a longer time (~60 min) to reach equilibrium. Owing to the many vacancies on the surface sites available for adsorption,

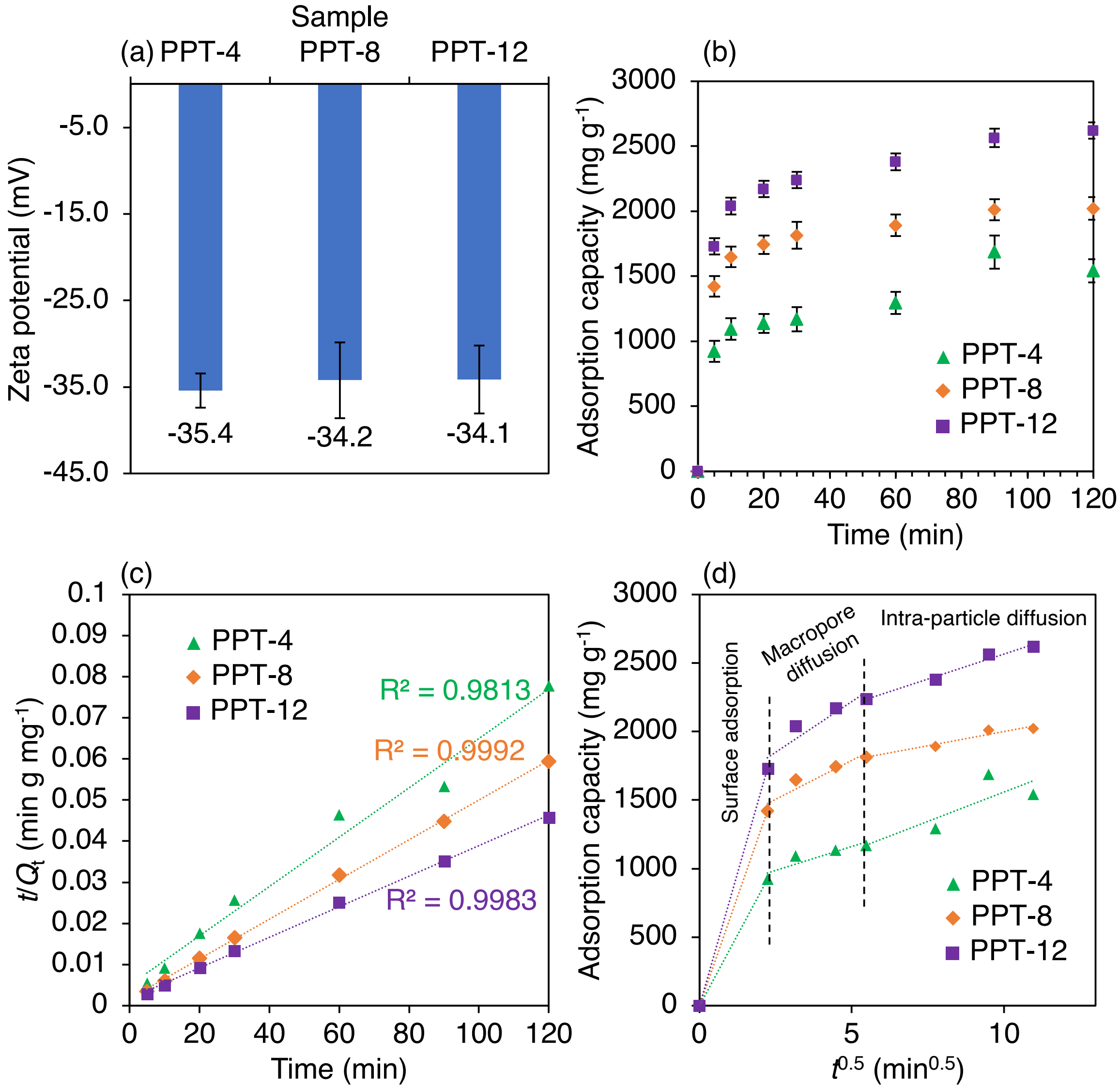

Figure 3.5: (a) Zeta potentials of the porous pectin particles at pH 7. (b) Adsorption capacity of lysozyme as a function of time under the following conditions: initial lysozyme concentration of 0.8 mg mL^{-1}, dosage of adsorbent of 0.2 mg mL^{-1}, pH of 7, and equilibrium time of 120 min. Error bars represent the standard deviation of means values corresponding to triplicate experiments. (c) Pseudo-second-order kinetic and (d) Weber–Morris diffusion model plots of porous pectin particles for lysozyme adsorption.

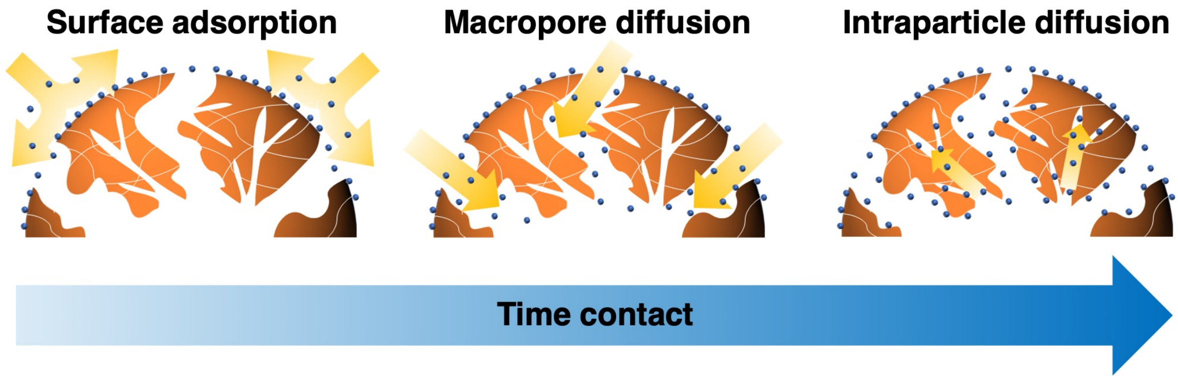

Figure 3.6: Lysozyme adsorption mechanism on porous pectin particles. Initially, lysozyme adsorbs on the external surface (left), and then lysozyme molecules penetrate the macropores (middle) and further diffuse into the binding sites of the mesopore regions (right).

the adsorption rate was high during the initial stage. However, it reached equilibrium after a sufficiently long period, and it was difficult for the remaining vacancies on the surface sites to be occupied owing to the repulsive forces between the solute molecules on the adsorbent surface. Therefore, surface adsorption played an essential role during the adsorption process.

To control the design parameters of the adsorption process, it is necessary to determine the adsorption behavior at equilibrium using adsorption isothermal models. Three empirically obtained two-parameter isotherm models, the Langmuir, Freundlich, and Temkin models, were used to analyze protein adsorption (the details are given in the Appendix B, Figure B.13). PPT-12 was selected to examine the adsorption isotherm owing to it showing the highest adsorption capacity among the porous pectin particles. As shown in Figure 3.7b, the Langmuir adsorption isotherm curve was the closest to the experimental data with an error value of less than 1% (Table B.1). The Langmuir model is applicable to predict homogeneous adsorption, which can only occur at a finite number of definite binding sites without steric hindrance between the adsorbate molecules and interaction between adjacent sites. The data indicated that the distinct horizontal plateau was achieved at a lysozyme concentration of approximately 0.8 mg mL^{-1}, which is the equilibrium saturation state where the surface is covered with a monolayer of lysozyme owing to complete filling of the active and available binding sites. In addition, the surface packing density of the lysozyme was calculated from the molecular weight of lysozyme, the adsorption capacity, specific surface area of porous pectin particles (detailed calculation in Section 14 of Appendix B). In porous pectin particles PPT-12, the results showed that there was 0.4 lysozyme molecule per square nanometer, which means there was about 1 lysozyme molecule per 3 nm^2 adsorbent. With the lysozyme dimensions of 4.5 nm × 3.0 nm × 3.0 nm, this result indicated that lysozyme was monolayer adsorbed in the end-on orientation.[144,145] From the Langmuir model parameters, the maximum equilibrium adsorption capacity (Q_{max}) of the adsorbent was in agreement with the experimental results (2666 mg g^{-1} (model) versus 2621 mg g^{-1} (experiment data)). Comparing PPT-12 with other adsorbents reported in the literature (Table 3.4), PPT-12 stands out because of several factors, such as its (i) macroporous structure and (ii) high specific surface area. This study provides a new class of materials with a porous structure and high specific surface area. With its particular macropores, this material shows great potential as an advanced adsorbent for many macromolecule applications in the biological field, such as a carrier for proteins and antibodies, a virus capturer, and for recovery of micro- and nanoplastic waste of various sizes.

3.4 CONCLUSIONS

Macroporous pectin particles with different specific surface areas have been successfully prepared by spray drying of pectin and $CaCO_3$ nanoparticles. Increasing the weight ratio of $CaCO_3$ to pectin from 4 to 12 resulted in an enhancement in the specific surface area from 177.0 to 222.3 m^2 g^{-1} and an increase in the total pore volume from 1.2 to 2.5 cm^3 g^{-1} owing to the contribution of pore formation. In addition, $CaCO_3$ plays an additional role in providing calcium ions after chemical removal of the $CaCO_3$ template to stabilize the porous structure through the egg-box model. PPT-12 showed the highest specific surface area of 222.3 m^2 g^{-1}, which was 150 times higher than that of the nonporous particles (PPT-0). This improvement and the abundance of accessible binding sites of the mesopores, macropores, and interconnected pore network can enhance the protein-adsorption capacity when applying porous pectin particles as an

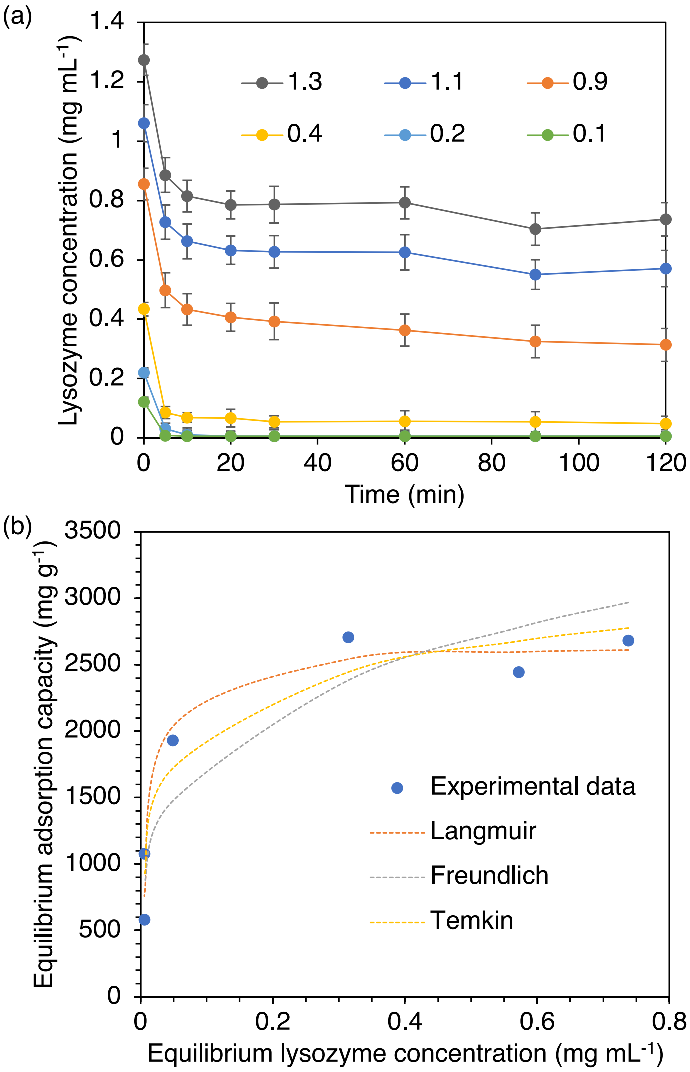

Figure 3.7: (a) Lysozyme concentration after adsorption of lysozyme to PPT-12 particles as a function of time under the following conditions: initial lysozyme concentration of 0.1, 0.2, 0.4, 0.9, 1.1, and 1.3 mg mL^{-1}, dosage of PPT-12 of 0.2 mg mL^{-1}, pH of 7, and equilibrium time of 120 min. (b) Adsorption isotherms of lysozyme on the PPT-12 particles.

adsorbent. All of the porous pectin particles showed rapid adsorption (~65% total capacity within 5 min) and high uptake capacity of lysozyme (>1500 mg lysozyme g^{-1} adsorbent), among which the PPT-12 particles showed the highest adsorption capacity of 2621 mg lysozyme g^{-1} adsorbent for the same amount of adsorbent particles. The high percentage of available active sites located in the macropores owing to the large and interconnected pores resulted in diffusion-promoted adsorption on the macroporous structure of the pectin particles. From adsorption isotherm investigation, adsorption of the protein was confirmed to rapidly form a monolayer following the Langmuir model. Owing to its specific structure, this material shows potential as an advanced macromolecule adsorbent with many potential applications, such as protein and antibody purification, virus capture, and recovery of micro- and nanoplastics from the environment. Along with that, the porous particles were synthesized from the natural polymer, which was exploited in significant quantities by a simple spray drying method without any modifications. In the future, this study is a premise with great potential for the synthesis of sustainable materials in large-scale industrial implementation. The ability to release active ingredients of porous pectin particles will also be studied to better understand the applicability of porous pectin particles.

Table 3.4: Comparison of lysozyme adsorption capacity with previously reported adsorbent.

Adsorbent	Amount of adsorbent (mg)	Initial lysozyme concentration (mg mL^{-1})	Maximum adsorption capacity (mg g^{-1})	Reference
Monolithic molecularly imprinted cryogel	240	5.0	36	[146]
MCM-41 silica particles	30	1.0	37	[147]
Tris(hydroxymethyl)amino methane-modified magnetic microspheres	5	0.30	109	[148]
Chitin-silica-based chromatographic matrix	50	10	117	[149]
PAA-modified Fe_3O_4@silica core/shell microspheres	4	0.27	127	[150]
N,*N*-dimethyl-*N*-methacryloyloxyethyl-*N*-(3-sulfopropyl) ammonium monomer	500	1.0	130	[151]
Sulfonated poly(glycidyl methacrylate) grafted cellulose	100	0.30	142	[152]
Reactive Red 120 modified magnetic chitosan microspheres	5	30	145	[153]
Porous cellulose nanofiber–Fe_3O_4 particles	10	0.20	955	[45]
Porous silica-supported carboxylated cellulose nanofibers	5	0.20	1516	[79]
Porous pectin particles	10	0.80	2621	This study

4

Porous Pectin Particles as a Colon Targeted Drug Delivery System

The conventional pectin delivery systems in the colon are often impaired by a slow release rate. Nanostructured particles, especially porous ones, have gained popularity as drug delivery systems owing to their high mass transfer efficiency. In this research, porous pectin particles were synthesized as drug carriers (using indomethacin as a model drug) via template-assisted spray drying. Specific surface areas of the porous pectin particles have been improved by up to 203 $m^2\ g^{-1}$ compared with nonporous particles (1 $m^2\ g^{-1}$). The porous structure shortened the diffusion path and improved the release rate of drug molecules. Additionally, the predominant drug release mechanism from porous pectin particles is Fickian diffusion, which is different from the combination of erosion and diffusion mechanism observed for nonporous particles. As a result, these porous drug-loaded pectin particles demonstrated rapid drug release rates of up to three times faster than nonporous particles. Control of the release rate could be achieved by changing the porous structure of the particles. This strategy is an efficient means to synthesize porous particles allowing rapid drug release into the colonic target.

---

published in part in *ACS Appl. Bio Mater.* 2023, 6, 2725–2737

4.1 INTRODUCTION

Efficient drug delivery has an essential role in medical therapy and remains numerous challenges, including the location, rate, and duration of release of a particular drug in the body. To address these problems, many different carriers and drug delivery systems have been investigated. As part of these efforts, nanostructured particles have emerged as potential novel drug carriers owing to their high specific surface area, high porosity, low density, hybrid functionalities, and ease of handling.[43,46,154,155] Notably, among the various nanostructured particles, porous particles have been commonly used for oral administration.[156,40] Porous particles are made to improve stability, reduce side effects, alter drug release profiles, and efficiently deliver a pharmaceutically active ingredient at a low dose.[157,158,159] Many conventional delivery systems necessitate the incorporation of high concentrations of active agents for therapeutic success owing to their low efficiency.[160] Thus, there is a need for delivery systems that can maximize the release period and efficiency of an active ingredient.

Porous particles expertly fulfill these aforementioned requirements. As porous particles are distinguished from common particles by their large surface area,[135,161,162] high porosity,[137] uniform and tunable pore structure,[136,45,79,163] and well-defined inner and outer surface properties,[164,165] they are particularly suited to the delivery of drugs with fast mass transfer.[40] For example, ammonium bicarbonate was used as the porogen to make porous microparticles from poly(lactic-*co*-glycolic acid) (PLGA) by a water-in-oil-in-water double emulsion method.[166] The most prevalent asthma medication, budesonide (BD), has a loading efficiency of approximately 60% in porous PLGA microparticles. The lung uptake efficiency of porous PLGA microparticles was higher than that of nonporous PLGA microparticles, and the sustained release of BD from porous PLGA microparticles was achieved for 24 h in vitro. In addition, to enhance drug delivery to the colon, a porous carrier composed of starch coated with chitosan–phytic acid was developed.[167] Porous starch displayed improved entrapment efficiency (87%) and drug loading (15%) for paclitaxel as a model hydrophobic drug. The release curve in the colon was obtained and indicated that 87% drug release was achieved. These approaches to controlling the porous structure and the drug release behavior from porous particles are useful for designing and tailoring novel drug delivery systems.

Ingredients that are ingested orally are typically absorbed and assimilated by the body through the epithelium of the small intestine; however, various bioactive ingredients, including living probiotics, and colon therapies require colonic delivery.[168] The oral administration of anti-inflammatory medications to the colon, such as antibiotics and chemotherapy agents, is necessary to treat inflammatory diseases.[169,170] As a result, delivery systems based on exploiting degradation by colonic bacterial enzymes have been developed for colon-specific delivery.[171,172] Different polysaccharidases that the intestinal microflora produces degrade polysaccharides for the most part. On the other hand, the acidic properties of the polysaccharides confer stability in the upper gastrointestinal tract. Among its other desirable attributes, pectin is an eco-friendly, renewable, non-immunogenic, and biodegradable polysaccharide.[173,174] Consequently, it is utilized extensively in pharmaceuticals, food, and other industries. Pectin-based delivery systems are suitable for colon delivery, particularly as pectin is indigestible in the human stomach or the small intestine and degraded by colonic bacterial enzymes.[175,176]

Compared with other modifications, the use of porous pectin is a cleaner strategy for the delivery of such substances.[177,178] In our previous study, porous pectin was prepared by template-assisted spray drying followed by chemical removal.[161,137] Porous pectin, which has a larger specific surface area, good stability in water, and excellent protein adsorption properties, has been used as an adsorbent. These properties are necessary for the effective adsorption of active ingredients, particularly proteins such as lysozyme. Given the favorable characteristics of porous pectin particles, we propose the generation of porous pectin-containing indomethacin (IND), a nonsteroidal anti-inflammatory drug for the colon. Previously, IND-loaded pectin microspheres were formed using spray drying.[94] However, they had a dense structure with a slow release of IND over 24 h. Therefore, with the aim of achieving rapid IND release, we produced a porous structure for IND-loaded pectin particles. A porous structure enhances the mass diffusion of drug molecules because the diffusion pathway is open and fully accessible. In this study, we investigate the generation of porous IND-loaded pectin particles through a general method of template-assisted spray drying followed by acid treatment to remove the template, and demonstrate their rapid drug release under the stimulated colon conditions of the enzyme pectinase. In this strategy, porous IND-loaded pectin particles enable a more rapid release rate than nonporous particles since the mass transfer of drug molecules has been improved through structural modification. The outcome of this study provided the concept for applying porous pectin particles in drug delivery at the colon target.

4.2 EXPERIMENTAL SECTION

4.2.1 Materials

Pectin was purchased from Herbstreith & Fox GmbH & Co. KG Pektin-Fabriken (Neuenbürg, Germany). Shiraishi Calcium (Osaka, Japan) provided calcium carbonate nanoparticles ($CaCO_3$ NPs) (suspension of 30.0 wt% in aqueous solution) with an average diameter of 86 nm (as determined from scanning electron microscope (SEM) images of more than 300 particles). The model drug IND and phosphate-buffered saline (PBS) pH 7.2 were purchased from FUJIFILM Wako Pure Chemical Corporation (Osaka, Japan). Enzyme pectinase (from Aspergillus niger, 366.0 U mg^{-1} at pH 4.0 and 40 °C) was purchased from Tokyo Chemical Industry Co. Ltd. (Tokyo, Japan). Citric acid was acquired from Sigma-Aldrich (Osaka, Japan). For all experiments, chemicals and solvents were used as received without further purification.

4.2.2 Preparation of porous IND-loaded pectin

In the first step, deionized (DI) water was used as the dispersant medium to prepare the precursor solution containing raw pectin, IND, and $CaCO_3$ NPs. The precursor solutions were controlled to have 1.0 wt% concentration of pectin and 0.1 wt% concentration of IND. $CaCO_3$ to pectin weight ratios of 0.5, 1, and 12 were used. The aqueous precursor was homogenized using an ultrasonic device (T 10 basic ULTRA-TURRAX S004, IKA, Osaka, Japan) for 30 min at a rotation speed of 12800 rpm to disperse the components. The content of the precursor solutions is presented in Table 4.1. The porous IND-loaded pectin particles were prepared by template-assisted spray drying followed by a chemical removal process. The method is illustrated in Figure 4.1a. An external two-fluid mixing nozzle with a 0.7 mm liquid orifice diameter and a 1.5 mm gas orifice diameter was attached to a mini spray-dryer (BÜCHI B-290, Flawil, Switzerland). The feed rate of the precursor solutions was 3.0 mL min^{-1}. The temperature of the inlet air during this procedure was 130 °C. The spray gas flow rate and aspiration rate were set to 357 and 37000 L h^{-1}, respectively. The porous structures were then made by immersing and washing the dried composite particles. Specifically, the $CaCO_3$ NPs was removed by stirring the composite pectin-IND-$CaCO_3$ particles for 15 min in an aqueous solution containing 10.0 wt% citric acid. Subsequently, they were thoroughly cleaned with ethanol and centrifuged for 5 min at 8000 rpm. The particles were then dried for 1 h in an oven at 80 °C. The nomenclature of the porous samples is given the form P-IND-X-Y, where X is the weight ratio of the template particles to pectin (X = 0, 0.5, 1, and 12) and Y represents the state before and after acid treatment (Y = Be for before acid treatment, Af for after acid treatment). The control sample of spray-dried pectin and IND only (P-IND-0) was prepared by the same method for comparison with the porous IND-loaded pectin particles. Before conducting further experiments, the P-IND-0 particles were soaked in citric acid to undergo the same experimental conditions as the porous particles.

4.2.3 Characterizations of porous IND-loaded pectin

The particle morphology was investigated by field-emission scanning electron microscopy (FE-SEM; S-5200, Hitachi High-Tech. Corp., Tokyo, Japan). The particles were prepared by dispersing in ethanol before being pipetted dropwise onto an aluminum plate and subjected to heating at 60 °C for drying of ethanol. Then, the dispersed particles were covered by a thin layer of sputtered platinum. The specific surface areas of the samples were determined from nitrogen adsorption–desorption isotherms obtained at 77 K using a Belsorp Max (BEL Japan, Osaka, Japan). Before measurement, each sam-

Table 4.1: Precursor concentrations of various porous IND-loaded pectin particles (DI water was used as the solvent).

	Pectin		IND		$CaCO_3$ NPs	
Sample*	Weight (g)	Mass fraction (%)	Weight (g)	Mass fraction (%)	Weight (g)	Mass fraction (%)
P-IND-0	1.0	1.0	0.1	0.1	-	-
P-IND-0.5	1.0	1.0	0.1	0.1	0.5	0.5
P-IND-1	1.0	1.0	0.1	0.1	1.0	1.0
P-IND-12	1.0	1.0	0.1	0.1	12.0	12.0

* P-IND-X-Y, where X is the weight ratio of the template particles to pectin (X = 0, 0.5, 1, and 12), Y represents the state before and after acid treatment (Y = Be for before acid treatment, Af for after acid treatment).

ple was preheated at 110 °C for 5 h. The specific surface areas were calculated by the Brunauer–Emmett–Teller (BET) method. The pore volume and pore size distribution were determined by the Barrett–Joyner–Halenda (BJH) and Horvath–Kawazoe (HK) method. A Fourier transform infrared (FT-IR) spectrophotometer (IRAffinity-1S with MIRacle 10, Shimadzu, Kyoto, Japan) was used to analyze the presence of IND in the samples. 5 mg of the samples was placed on diamond prism. The samples were then pressed with a sample clamp. The FT-IR spectra were obtained by the attenuated total reflection method. X-ray diffraction (XRD) analysis was conducted using a Bruker D2 PHASER equipped with a Cu Kα radiation source (40 kV and 30 mA, Bruker Corp., Billerica, MA, USA). The diffraction patterns were recorded in the range from 10° to 60°.

4.2.4 Determination of IND in pectin particles

First, pectinase solution (40.0 U mL^{-1}) was prepared by dissolving 0.11 g pectinase into 1.0 L PBS solution. The amount of IND-loaded in the pectin particles was determined by placing 10.0 mg of porous IND-loaded pectin particles in 50.0 mL of pectinase in PBS (40.0 U mL^{-1}) at pH 7.0 for 36 h at 37 °C with vigorous stirring. The solution was then centrifuged at 15000 rpm for 5 min. An ultraviolet–visible (UV–vis) spectrophotometer (UV-2450, Shimadzu, Kyoto, Japan) was used to determine the IND concentration in the supernatant through measurement of the absorbance at 319 nm. The calibration curve of the IND solution was prepared from 1.1×10^{-4} to 0.11 mg mL^{-1} (correlation factor $R^2 = 0.9994$, Figure C.1). The following equations were used to calculate the IND content as a percentage and the loading efficiency. All experiments were conducted in triplicate.

$$\text{Theoretical IND loading content } (\%) = \frac{\text{weight of feed IND}}{\text{weight of feed pectin, IND, and CaCO}_3} \times 100 \tag{4.1}$$

$$\text{Actual IND loading content } (\%) = \frac{\text{weight of loaded IND in particles}}{\text{weight of particles}} \times 100 \tag{4.2}$$

$$\text{Loading efficiency } (\%) = \frac{\text{Actual IND loading content}}{\text{Theoretical IND loading content}} \times 100 \tag{4.3}$$

4.2.5 Drug release studies

The procedure for drug release in the simulated colon conditions is illustrated in Figure 4.1b. The release rate was measured as follows: 10.0 mg of IND-loaded pectin particles (nonporous and porous particles) was suspended in 2.0 mL of pectinase in PBS (40.0 U mL^{-1}) at pH 7.0. The solution was placed in a dialysis tube (Mini Dialysis Kit, 1 kDa cut-off) and the tube was introduced into 50.0 mL of release medium (PBS). The temperature was kept at 37 °C. The medium was stirred vigorously. At predetermined times, 3.0 mL of the release medium was removed, and an equal volume of fresh PBS was added. The IND concentration that was released into the medium was detected through measurement of the absorbance at 319 nm using a UV–vis spectrophotometer. All experiments were conducted in triplicate.

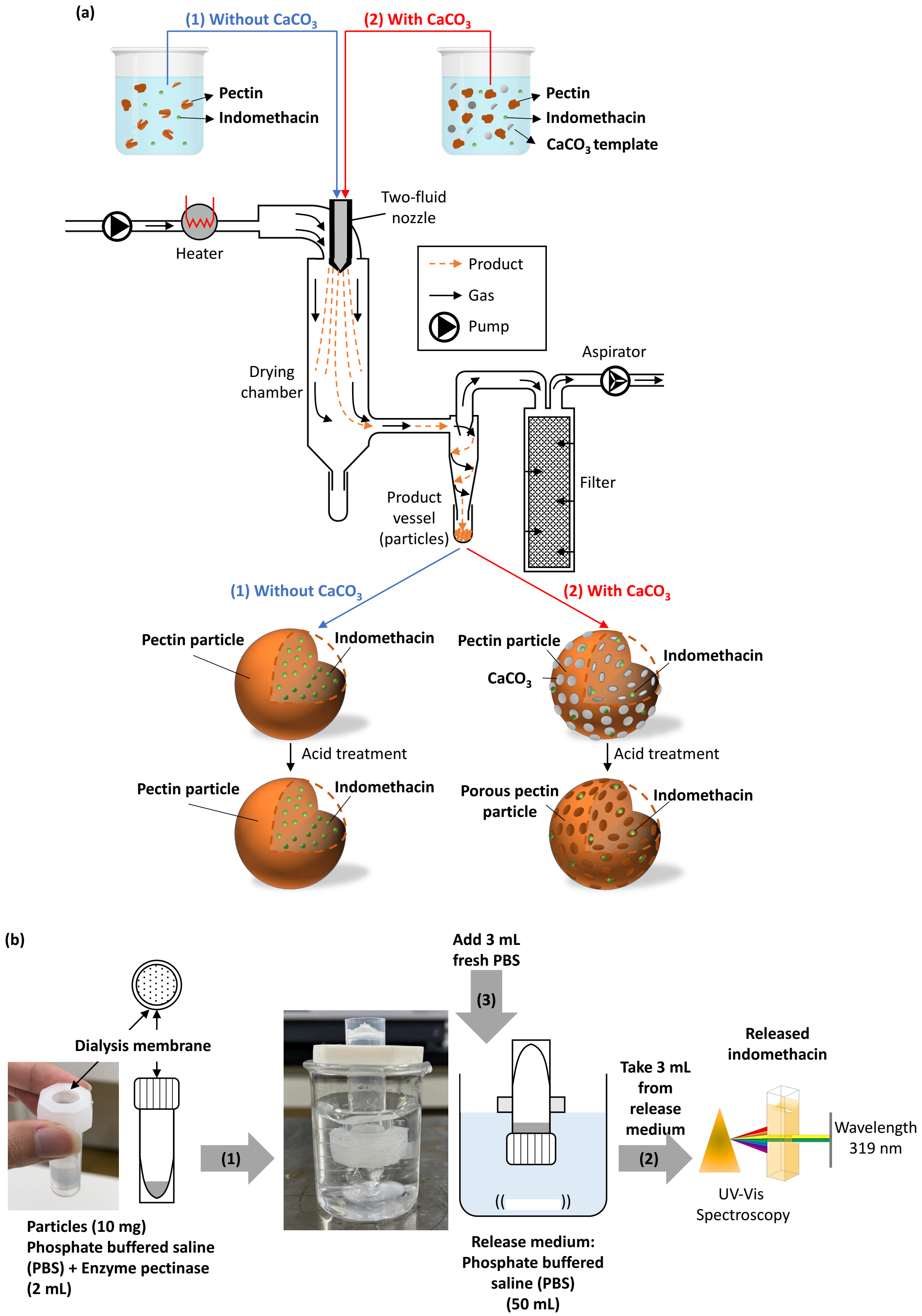

Figure 4.1: (a) Preparation procedure for porous IND-loaded pectin particles. The precursor solution containing pectin, IND, and CaCO$_3$ NPs was spray-dried to form the pectin-IND-CaCO$_3$ composite particles. (b) Procedure for the IND release study: (1) 10.0 mg of IND-loaded pectin particles (nonporous and porous particles) was suspended in 2.0 mL of PBS with the enzyme pectinase (40.0 U mg^{-1}) in a dialysis tube; (2) at predetermined times, the absorbance of 3.0 mL of the release medium was measured at 319 nm using a UV–vis spectrophotometer; and (3) 3.0 mL of fresh PBS was added to the release medium.

4.3 RESULTS AND DISCUSSION

4.3.1 Morphology and characterizations of IND-loaded pectin particles

SEM imaging was used to validate the morphologies of IND-loaded pectin particles after spray drying, as shown in Figure 4.2a–d. Spray drying of the precursor solution comprising IND and pectin produced particles with a smooth surface (Figure 4.2a). The composite pectin-IND-$CaCO_3$ particles were created by spray drying pectin, IND, and $CaCO_3$ NPs (Figure 4.2b–d). The distribution of $CaCO_3$ NPs in the prepared particles increased as the amount of $CaCO_3$ NPs were utilized in the template. Citric acid was used to remove the $CaCO_3$ NPs, creating the final particles with porous structures.

The SEM images of IND-loaded pectin particles produced with various $CaCO_3$ NPs to pectin weight ratios after acid treatment are shown in Figure 4.2e–h. Following the acid treatment, the $CaCO_3$ NPs-free particles (P-IND-0-Af) were no longer as smooth as previously observed (Figure 4.2e). As pectin is hydrophilic, this finding suggests that some of the pectin had been partially dissolved. The chemical removal of the $CaCO_3$ NPs using citric acid was successful in introducing porous structures with spherical morphology into the pectin particles, as shown in Figure 4.2f–h. P-IND-0.5-Af and P-IND-1-Af particles had a porous exterior structure, as seen in Figure 4.2f and g. In Figure 4.2h, the surface roughness of P-IND-12-Af increased. This observation indicated that the number of pores increased proportionately with increasing $CaCO_3$ NPs concentration, from 7 to 110 per square micrometer (Figure C.2). It could be explained by the fact that the number of pores is influenced by the distribution of $CaCO_3$ NPs in the particles. In addition, pores smaller than the size of $CaCO_3$ NPs were observed on the surface. The formation of these small pores was due to the release of CO_2 following the acid removal of $CaCO_3$ NPs. These data are consistent with previous studies.[161,137] These findings demonstrate that alterations of the $CaCO_3$ NPs concentration can be used to modify the porous structure.

In order to comprehend the properties of IND-loaded pectin particles after being treated with acid, various analyses were conducted on their particle sizes, specific sur-

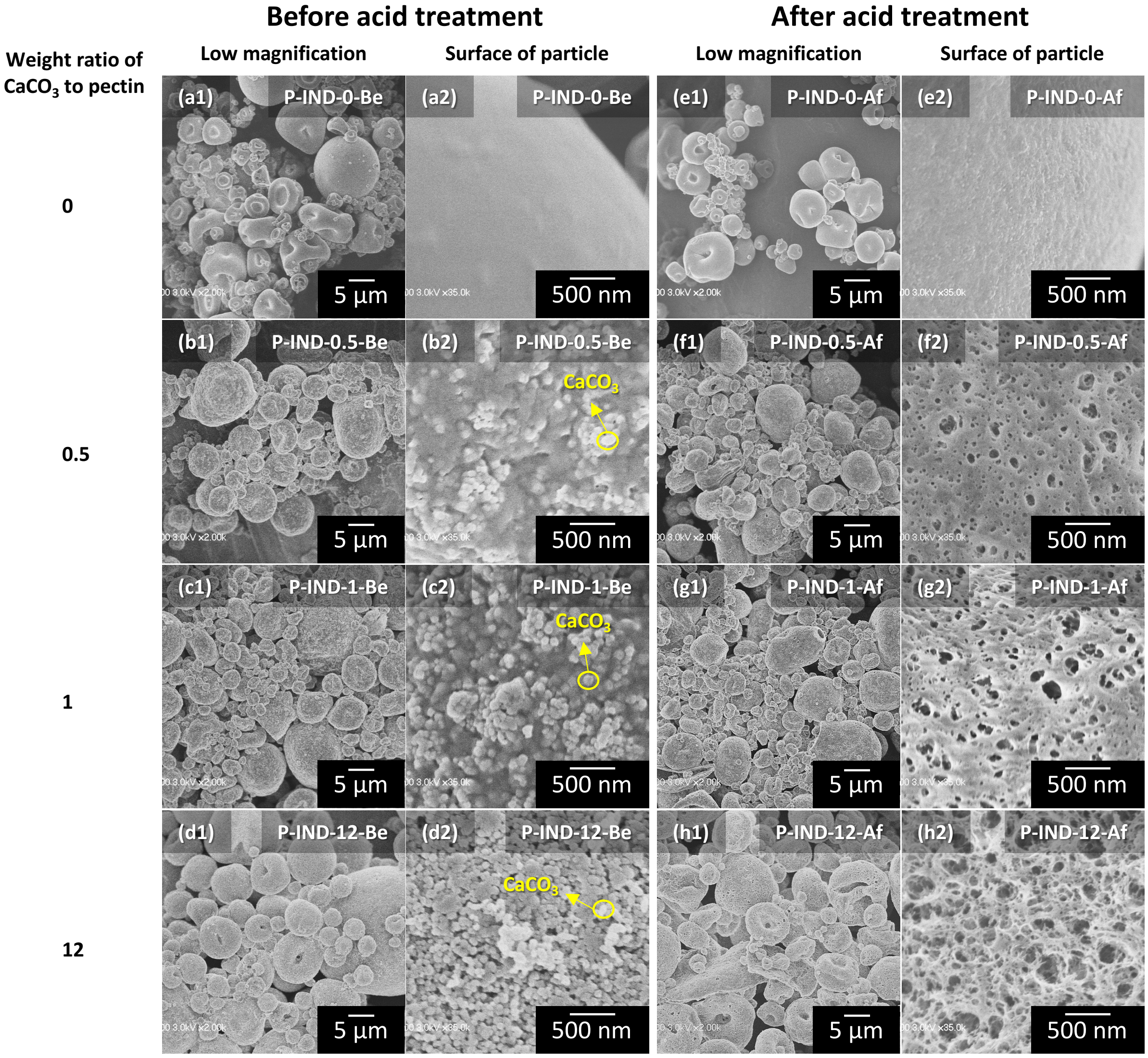

Figure 4.2: SEM images of various IND-loaded pectin particles before and after acid treatment with calcium carbonate to pectin weight ratios of (a, e) 0, (b, f) 0.5, (c, g) 1, and (d, h) 12. The images at different magnifications are classified into two categories: (1) images at a magnification of ×2000, and (2) images of the surface of a particle at a magnification of ×35000.

face areas, and pore volumes. The size of the P-IND-0-Af particles was about 6 µm (Figure C.3a). By altering the $CaCO_3$ NPs/pectin ratio from 0.5 to 12, the average particle size increased from 3 to 7 µm as shown in Figure C.3b – d. The pore structure analysis involved studying the nitrogen adsorption and desorption isotherms (Figure C.3e and f). The P-IND-0-Af particles showed type II isotherms, which are characteristic of non-porous materials.[101] On the other hand, P-IND-0.5-Af, P-IND-1-Af, and P-IND-12-Af particles displayed combined isothermal adsorption behavior between type II and type IV, which is typical of mesoporous and macroporous materials.[101] The type H2 hysteresis loop was observed in these samples at a relative pressure of $P/P_0 > 0.8$, indicating a wide distribution of pores. To investigate the impact of $CaCO_3$ NPs on pore formation, the pore size distribution of particles P-IND-0-Af, P-IND-0.5-Af, P-IND-1-Af, and P-IND-12-Af was further analyzed (Figure C.3g). The HK method was used to evaluate the micropore size distribution in the 1 to 2 nm range, while the BJH method was used to analyze the general pore size distribution in the range of 2 to 100 nm. The pore size distributions of P-IND-0-Af and P-IND-0.5-Af were lower than that of P-IND-1-Af and P-IND-12-Af. It can be seen that the pore sizes in the two samples P-IND-1-Af and P-IND-12-Af ranged from 40 to 100 nm, with a peak distribution at 60 nm, which was similar to the size distribution of $CaCO_3$ NPs (about 86 nm). These findings indicated that $CaCO_3$ NPs played a critical role in pore formation in the final particles.

Based on the data presented in Table 4.2, the incorporation of $CaCO_3$ NPs significantly increased the specific surface area by forming pores of various sizes. The specific surface area calculated using the BET equation for P-IND-0-Af particles was 1 $m^2\ g^{-1}$. The specific surface area of the P-IND-0.5-Af particles was 31 $m^2\ g^{-1}$. P-IND-1-Af particles had the specific surface area of 115 $m^2\ g^{-1}$, which represents an increase of about 115-fold, compared to P-IND-0-Af. P-IND-12-Af had the highest specific surface area of 203 $m^2\ g^{-1}$. The porous structure in P-IND-12-Af enhanced its specific surface area by 200 times relative to P-IND-0-Af. The formation of porous structure also increased the total pore volume. P-IND-0.5-Af has a total pore volume of 0.12 $cm^3\ g^{-1}$, a 30-fold increase compared to $4.3 \times 10^{-3}\ cm^3\ g^{-1}$ of P-IND-0-Af. The total pore volume of P-

IND-1-Af and P-IND-12-Af increased significantly with values of 0.67 cm^3 g^{-1} and 2.9 cm^3 g^{-1}, respectively. These values are 150 and 665 times greater than the values of P-IND-0-Af. These results confirmed that the structure of the porous pectin particles allows for good penetration by small compounds with plenty of space on the surface and interior.

Table 4.2: Characterizations of specific surface areas, and pore volumes of IND-loaded pectin particles.

		Pore volume			
Sample	Specific surface area S_{SSA} (m^2 g^{-1})	Micropore $V_{micropore}$ (cm^3 g^{-1})	Mesopore $V_{mesopore}$ (cm^3 g^{-1})	Macropore $V_{macropore}$ (cm^3 g^{-1})	Total pore volume V_t (cm^3 g^{-1})
P-IND-0-Af	1	2.8×10^{-4}	1.7×10^{-3}	2.3×10^{-3}	4.3×10^{-3}
P-IND-0.5-Af	31	0.014	0.083	0.025	0.12
P-IND-1-Af	115	6.9×10^{-3}	0.28	0.38	0.67
P-IND-12-Af	203	0.036	1.4	1.5	2.9

4.3.2 IND loading efficiency

Only physical interactions occur between IND and pectin components, as well as $CaCO_3$ NPs. This phenomenon is supported by the FT-IR spectra of different IND-loaded pectin particles, as shown in Figure 4.3. The FT-IR spectra of pectin and IND were utilized as standards for comparison with the prepared particles. The characteristic peaks observed at 1400 and 1600 cm^{-1} were attributable to the carboxyl (COOH) groups of pectin.[161,137] For IND, there are characteristic peaks of two carbonyl C=O groups at 1687 and 1708 cm^{-1}.[179,180] As shown in Figure 4.3a, after spray drying, the IND-loaded pectin particles all displayed the characteristic signals of pectin. No new signals were observed in these samples, indicating that the self-assembly of pectin, IND, and $CaCO_3$ NPs occurred during the spray drying without forming chemical reactions or involving other intermediate components. Moreover, no signals characteristic of IND were observed in these particles, which indicated that IND was completely encapsulated inside the pectin particles after spray drying. After acid treatment of all of the IND-loaded pectin particles (Figure 4.3b), the signals characteristic of pectin were still present, which indicated that the acid treatment had no impact on the chemical composition of pectin. In the nonporous sample P-IND-0-Af, the characteristic signals of IND emerged in the spectrum. These results suggest that pectin was partially dissolved in water following the acid treatment and indicate the presence of IND. Additionally, signals characteristic of IND were also present in the porous particles P-IND-0.5-Af, P-IND-1-Af, and P-IND-12-Af. This emerged signal differs from the distinctive doublet peak of IND and can be attributed to the formation of hydrogen bonds between the carbonyl group of IND and pectin,[181,182,183] as illustrated in Figure C.4. In the case of porous samples, IND was detectable as the porous structure was formed in these pectin particles after the removal of $CaCO_3$ NPs. This FT-IR investigation provides evidence that IND was successfully loaded into pectin particles. In addition, Figure C.5 showed the XRD pattern of IND-loaded pectin particles after acid treatment. It can be seen that the pectin (raw material) has an amorphous structure, while the IND has a crystalline structure. After spray drying, the pattern of P-IND-0-Be particles showed the crystalline peaks of IND and also amorphous pectin. However, after acid treatment, the structure of P-IND-0-Af existed only in the amorphous form. From the FT-IR analysis of P-IND-0-Af, IND was still present in the particles after acid treatment. Hence, it is plausible that the acid treatment caused a transformation of IND from a crystalline to an amorphous structure by dehydration.[184,185,186] This hypothesis was verified through the amorphous pattern of the acid-treated IND (IND-Af). Additionally, there might be a loss of IND during the acid treatment process, leading to a variation in the signal intensity between P-IND-0-Af and P-IND-0-Be. To validate this hypothesis, a quantitative analysis of the IND content in each sample will be conducted in the subsequent analysis. The resulting amorphous structure was also observed in P-IND-0.5-Af, P-IND-1-Af, and P-IND-12-Af particles. According to previous studies, the amorphous formulation enabled the dissolution enhancement compared to crystalline structure.[187] This is an advantage for applying IND-loaded pectin particles for the colon targeted drug delivery system.

We quantified the IND content in pectin particles to provide more evidence for the presence of IND. The amount of IND-loaded in pectin particles before acid treatment

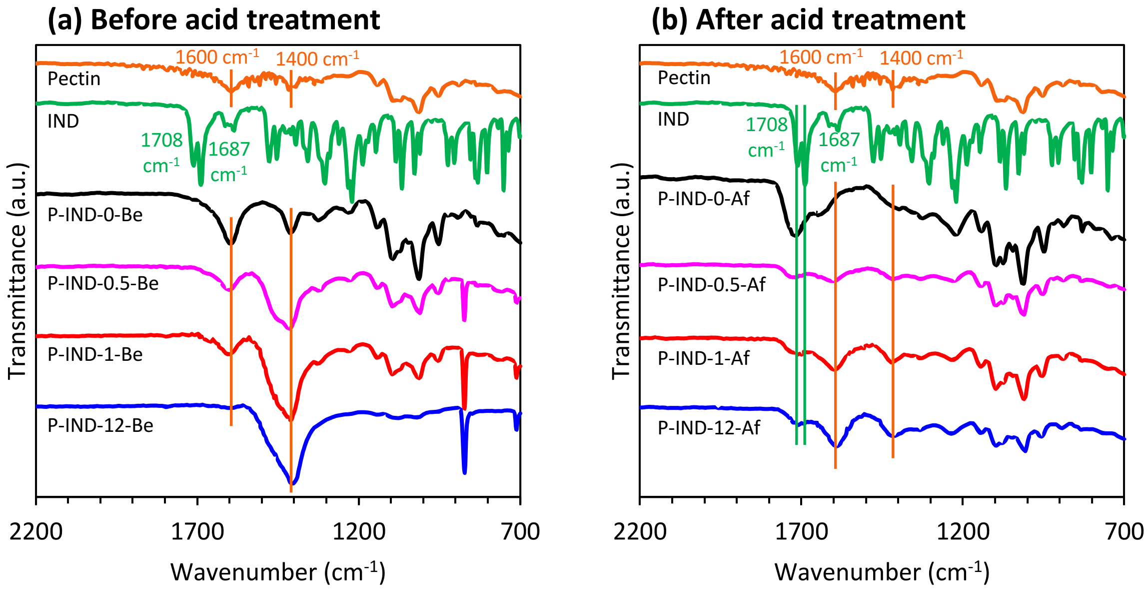

Figure 4.3: FT-IR spectra of various IND-loaded pectin particles (a) before acid treatment (after spray drying), and (b) after acid treatment. The spectra of pectin and IND were used as references for the comparison.

(after spray drying) (Figure 4.4a) and the IND loading efficiency (Figure 4.4b) were reasonable and in good agreement with a previous study.[94] The IND loading efficiencies of all samples were greater than 90%. Interestingly, these data demonstrate that the spray drying process and additional $CaCO_3$ NPs did not affect the loading efficiency of the prepared particles. At this stage, the IND loading content in the particles gradually decreased owing to the increase in $CaCO_3$ NPs. However, the drug loading behaviors of different carriers (nonporous and porous particles) after acid treatment was changed, as shown in Figure 4.4c and d. There was a clear loss (of almost half) in the drug content of all samples (Figure 4.4c). In addition, the loading efficiency decreased as the total pore volume increased (Figure 4.4d). One reason for this observation may be due to the weak interaction of IND with pectin (Figure C.5).[167] The adsorption of IND into pectin is mainly driven by the hydrophobic CH-π effect, whereas hydrogen bonding is the main force retaining IND in the particles. Thus, the greater the total pore volume of particles, the more IND may diffuse out of the particles during immersion in acidic solution and be removed when the particles are washed.[188,189] Also, possibly IND was attached to the surface of the $CaCO_3$ NPs in the assembly, and is then easily washed out. This fact has been supported by additional experimental results. Initially, a solution containing IND in water was prepared, and the IND concentration was determined by UV-vis spectroscopy. Subsequently, $CaCO_3$ was added to the IND solution, and the resulting mixture was centrifuged to remove the solid portion, allowing for the collection of the supernatant. The IND concentration in the supernatant was then determined by measuring its absorbance. The results regarding the absorbance of IND before and after the addition of $CaCO_3$ are depicted in Figure C.6. The findings demonstrate a decrease in the absorbance of IND in the extracted solution compared to the initial absorbance. Therefore, it can be concluded that a portion of IND has bound to $CaCO_3$ and settled in the solid phase. This phenomenon can be explained that IND is a weak acid, whereas $CaCO_3$ is a basic compound. When IND and $CaCO_3$ come into contact within an aqueous environment, an acid-base reaction may occur. The acidic IND can react with $CaCO_3$, resulting in the formation of calcium salts of IND, such as calcium indomethacin. These salts can be washed out during the washing process.[190,191]

4.3.3 IND release study

Pectin particles are excellent carriers for drug release owing to their distinct physicochemical properties and outstanding biocompatibility with the colonic bacteria.[171,172] Therefore, the enzyme pectinase was employed to simulate the experimental circumstances of drug release in the colon. We investigated the drug release rate from pectin particles with different porous structures and compared it with that from nonporous particles. The time-dependent release curves of different drug-loaded carriers are presented in Figure 4.5a – b. IND is released by dissolution from the carrier substrate and diffuses via the three-dimensional network structure to produce controlled and sustained release. Figure 4.5a showed the result of IND release from the particles in the absence of pectinase. The result indicated that about 30% of the IND was released after 60 min for all samples. It is consistent with that reported in previous studies.[94] The release of IND without using pectinase can be attributed to the release of IND on surfaces. The IND release profile in the presence of pectinase was shown in Figure 4.5b. All the IND-loaded pectin particles burst in the initial stage of drug release. The main reason

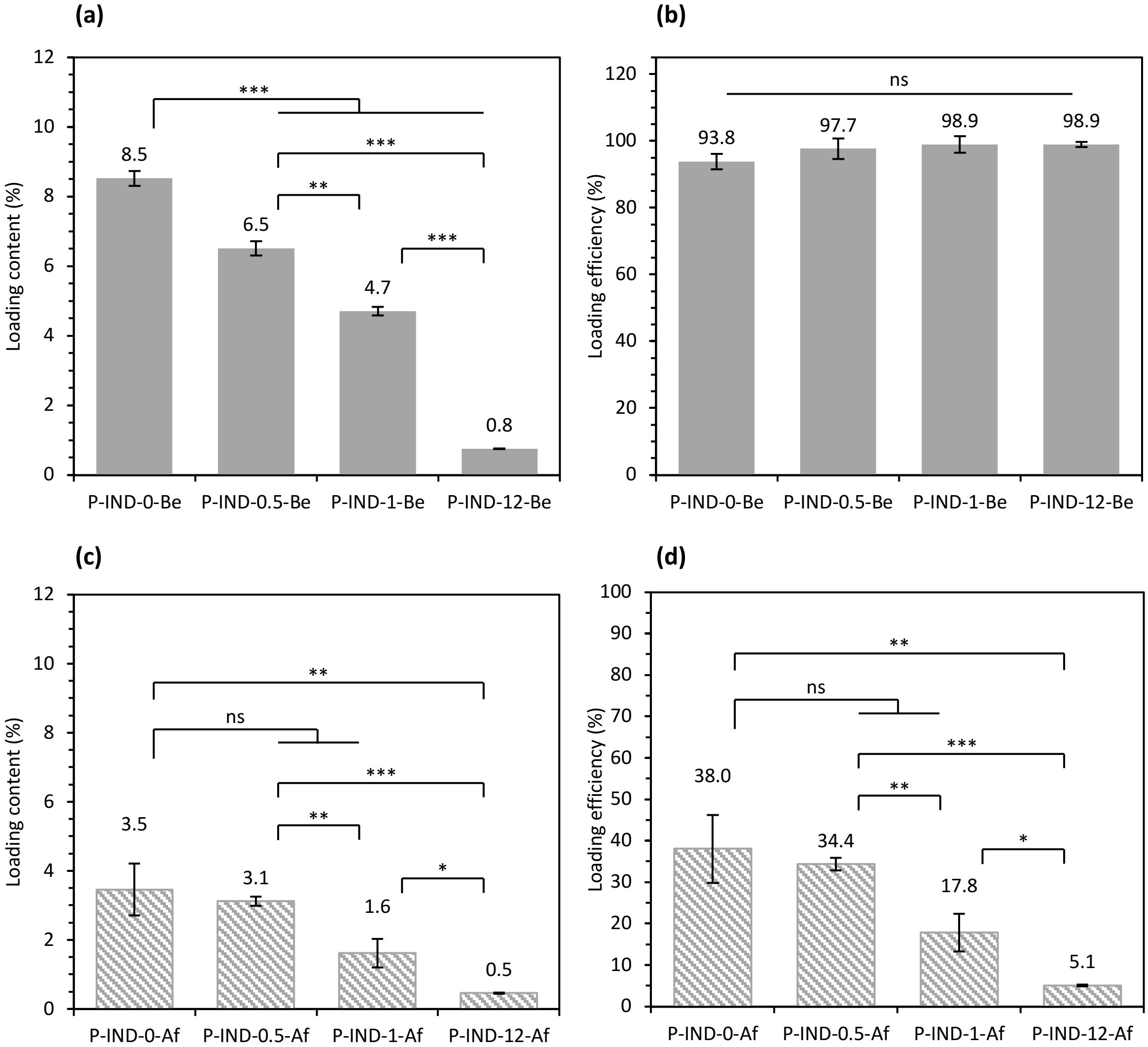

Figure 4.4: IND loading content, and loading efficiency of various IND-loaded pectin particles (a, b) before, and (c, d) after acid treatment. All data are presented as the average ± standard deviation. n = 3 for all analyses. *$p < 0.05$, **$p < 0.01$, and ***$p < 0.001$. ns refers to a $p > 0.05$.

for burst release was the drug near the surface of particles.[192] Another reason was that some parts of the particle surface were eroded, allowing IND to leach into the medium. This phenomenon was confirmed by SEM images of samples collected after the release experiments, as shown in Figure 4.6. The rate of IND release from porous P-IND-0.5-Af, P-IND-1-Af, and P-IND-12-Af particles was more rapid than from release rate of nonporous particles (P-IND-0-Af). The difference in drug release rates between these two types of particles was due to their structural differences. The drug release from P-IND-1-Af and P-IND-12-Af particles was complete in 20 min, whereas IND-loaded P-IND-0.5-Af particles sustained drug release for approximately 30 min. However, the release from P-IND-0-Af particles was only 60% at 20 min, with further gradual release until 60 min. The release profile shows that P-IND-0.5-Af released IND twice as fast as P-IND-0-Af, even though the loading content was almost the same. An increase in the total pore volumes and higher specific surface areas, which promotes the diffusion process of IND by shortening the diffusion path length and improving the release rate of particles.[166,167,193] Consequently, the drug release rates from porous P-IND-1-Af and P-IND-12-Af particles were more rapid than from P-IND-0.5-Af particles, up to three times faster than that from P-IND-0-Af. However, as the $CaCO_3$ NPs to pectin weight ratio increased from 1 to 12, the release rate did not change significantly. Therefore, it can be assumed that P-IND-1-Af might be a good candidate among the others for IND release. Moreover, the IND release rate from nonporous P-IND-0-Af is slower than from porous compounds as they need time to erode before IND can be leached from them. This result demonstrates the advantage provided by the porous structure, which is able to promote more rapid drug release than the conventional dense structure. Compared with IND release profile without pectinase, IND was released more rapid when pectinase was used. From this outcome, we can emphasize that the main reason for selecting pectin as a drug carrier was its biodegradable property in the colon by colonic microflora. Under the influence of pectinase that is found in the colon, the drug release rate from pectin particles would be faster. Therefore, these particles can be used as drug carriers for colonic delivery.

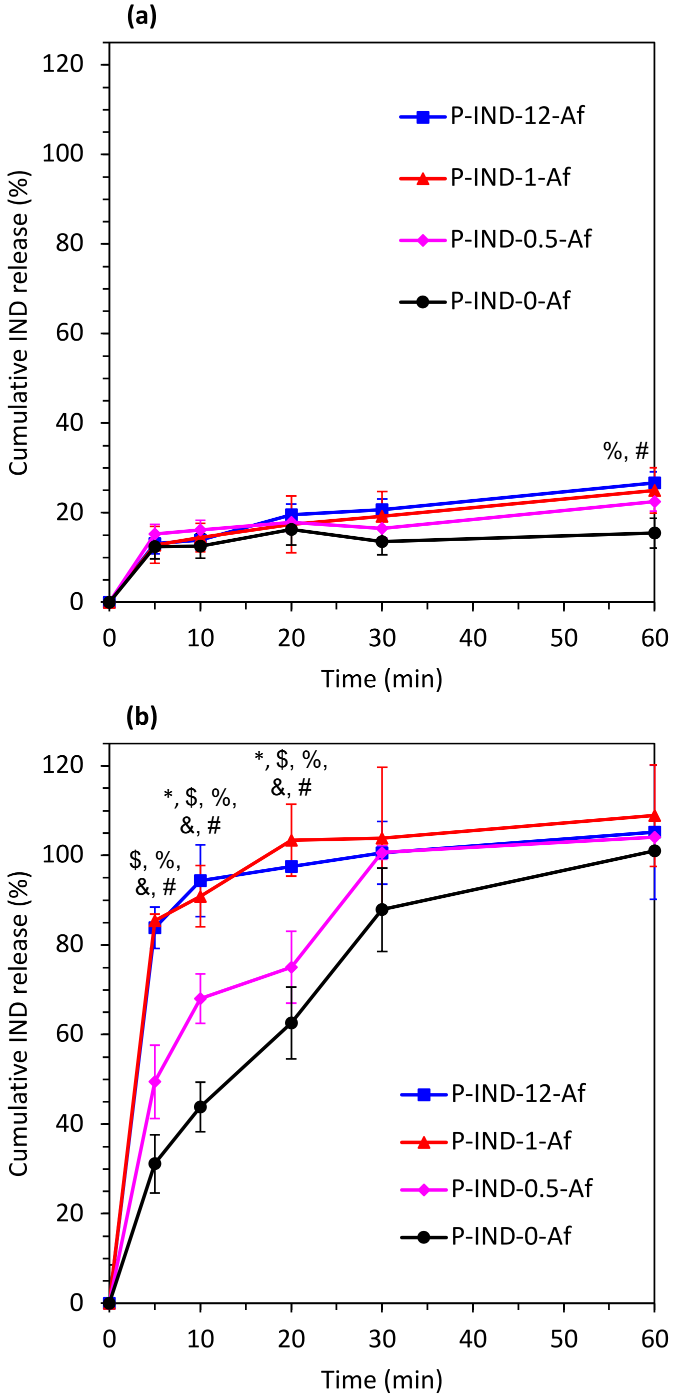

Figure 4.5: Release profiles of IND (a) without and (b) with enzyme pectinase from the P-IND-0-Af, P-IND-0.5-Af, P-IND-1-Af, and P-IND-12-Af pectin particles. All data are presented as the average ± standard deviation. n = 3 for all analyses. * $p < 0.05$ (P-IND-0-Af vs P-IND-0.5-Af). \$ $p < 0.05$ (P-IND-0-Af vs P-IND-1-Af). % $p < 0.05$ (P-IND-0-Af vs P-IND-12-Af). & $p < 0.05$ (P-IND-0.5-Af vs P-IND-1-Af). # $p < 0.05$ (P-IND-0.5-Af vs P-IND-12-Af).

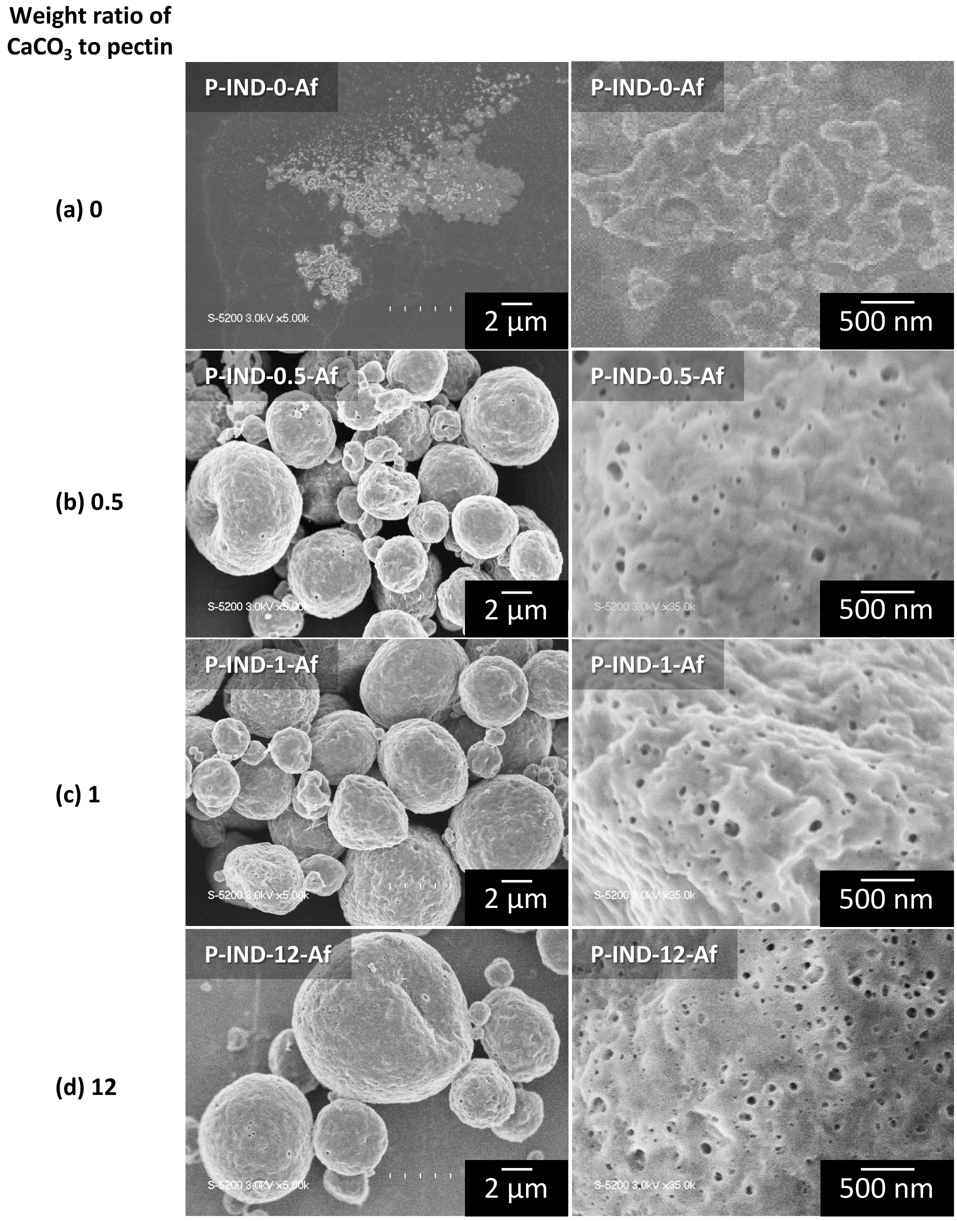

Figure 4.6: SEM images of various IND-loaded pectin particles after release experiments with $CaCO_3$ NPs to pectin weight ratios of (a) 0, (b) 0.5, (c) 1, and (d) 12. The images at different magnifications can be classified into two categories: images of one particle at a magnification of ×10000 and images of the surface of a particle at a magnification of ×35000.

4.3.4 Release kinetics

Mathematical models were applied to determine the mechanism through which drug release occurred and were interpreted in the form of a graphical presentation, as shown in Figure C.7. Several release kinetics models, including the zero-order (Figure C.7a, Equation C.1), first-order (Figure C.7b, Equation C.2),[194] Higuchi (Figure C.7c, Equation C.3),[195,196] and Korsmeyer–Peppas models (Figure C.7d, Equation 4.4 and Equation C.4),[197,198] were used to fit the drug release data for the four samples, P-IND-0-Af, P-IND-0.5-Af, P-IND-1-Af, and P-IND-12-Af. The correlation coefficients (R^2 values) and fitting parameters for the four models of the IND-loaded pectin particles are summarized in Table 4.3. The most suitable mathematical model that measured the kinetics of drug release was selected by the largest correlation coefficient.

Fitting the experimental data to the four samples revealed that the Korsmeyer–Peppas model had a higher correlation coefficient than other models. The fitting coefficient was up to 0.9755, indicating that the fitting data were comparable to the actual connection between the parameters of the response data. The Korsmeyer–Peppas model, which is derived from Fick's law theory, is an ideal drug release kinetic model.[199] The formula is shown below:

$$\frac{C_t}{C_\infty} = k_{KP}\, t^n \tag{4.4}$$

where C_t is the concentration of the drug in the release solution at time t; C_∞ is the equilibrium concentration of drug in the release solution; t is the release time; k_{KP} is the kinetic rate constant; and n is the release exponent, a parameter that characterizes the release mechanism. As indicated in Table C.1, when n is less than 0.45, the drug release mechanism follows Fick diffusion,[200] and the release is mainly based on drug diffusion; when $0.45 < n < 0.89$, drug release is non-Fickian diffusion, and the drug release mechanism is non-Fickian diffusion (anomalous) control; when $n > 0.89$, the drug release is dominated by erosion.

Two essential fitting variables comprise the Korsmeyer–Peppas equation: k_{KP}, the kinetic rate constant; and n, the release exponent. Interestingly, as shown in Table 4.3, the rate constant k_{KP} increases as the $CaCO_3$ NPs used for pore formation increases (k_{KP} values of P-IND-0-Af, P-IND-0.5-Af, P-IND-1-Af, and P-IND-12-Af increase, from 0.12, 0.32, 0.73, and 0.75, respectively). The increased rate constants indicated that the release rates increased as the particles became more porous. This increase in release rates may be governed by the increased surface area resulting from the pores. This observation was consistent with aforementioned release profiles and previous studies,[166,167,193] which reported that drug release was proportional to the increased effective surface area of the particles owing to the decrease in diffusional path length. However, the release rate did not change significantly when the $CaCO_3$ NPs to pectin weight ratio increased from 1 to 12. This result proves that the $CaCO_3$ NPs to pectin weight ratio of 1 may effectively create an excellent structure for the IND release rate.

The release exponent n may provide further insight into the unexpected increase in the release constant. The drug release mechanism is defined by the release exponent n. From the fitting of our model, the nonporous P-IND-0-Af particles had an n value of 0.50 (greater than 0.45). Values above 0.45 typically indicate anomalous drug transport; thus, this suggests that the drug release from the nonporous P-IND-0-Af particles was caused by Fickian diffusion of the drug from the particles, as well as release following the degradation and subsequent erosion of the pectin particles.[198] In clear contrast, the release constant for the porous particles P-IND-0.5-Af, P-IND-1-Af, and P-IND-12-Af were 0.31, 0.10, and 0.09, respectively, below 0.45. These data revealed that Fickian diffusion dominated the drug release mechanism.[198,200] We hypothesize that the thin walls of the pores and the tunnels within the porous particles led an increase in the surface area, which promoted the Fickian diffusion process. This analysis was consistent with the drug release mechanism proposed above. Our results suggest that porous particles may deliver their payload faster than the complete degradation of the pectin. Thus, it may be essential to consider the polymer formulation and the porous structure in the design of particles for specific drug delivery applications.

Table 4.3: Parameters for different models of IND release from P-IND-0-Af, P-IND-0.5-Af, P-IND-1-Af, and P-IND-12-Af.

Model		P-IND-0-Af	P-IND-0.5-Af	P-IND-1-Af	P-IND-12-Af
Zero-order model	$k_0 \times 10^{-5}$	7.4	6.2	0.48	0.41
	R^2	0.8725	0.7749	0.7443	0.6971
First-order model	k_1	0.020	0.012	0.004	0.004
	R^2	0.7915	0.7260	0.7252	0.6726
Higuchi model	k_H	0.22	0.13	0.04	0.04
	R^2	0.9502	0.8761	0.8642	0.8278
Korsmeyer–Peppas model	n	0.50	0.31	0.10	0.09
	k_{KP}	0.12	0.32	0.73	0.75
	R^2	0.9755	0.9303	0.9185	0.9390

4.3.5 Release mechanisms

Based on the release profile and the SEM images of the particles collected after the IND release experiments, we proposed mechanisms for the release of IND from the nonporous and porous pectin particles, as illustrated in Figure 4.7. For nonporous particles (Figure 4.7a), we observed a rapid release of the model drug, IND, in the first 20 min. It is known that diffusion and erosion regulate the release of drugs from nonporous biodegradable particles.[201,202] Governed by the drug transport properties, the release phase is initially controlled by diffusion through the polymeric matrix and water-filled pores. Thus, slow release of the drug molecules into the medium occurs. The second process involves bulk erosion. The polymer chains are degraded, become small enough to be soluble, and the drug is released during the dissolution of pectin (Figure 4.6a). This occurrence will, in turn, accelerate the diffusion rate of the released drug, resulting in the complete release.[203] Porous pectin particles are more stable in aqueous solution than nonporous particles as they are reported to form an "egg-box structure" with calcium ions.[161,140] Even if the surface of porous particles is partially eroded (Figure 4.6b–d), the primary transport mechanism for porous particles is diffusion through pores (Figure 4.7b).[204] At this point, the drug molecules are released rapidly into the medium until the release was complete. In the case of small molecule drugs that diffuse rapidly through the particles, complete release may have occurred before total particle degradation and erosion.[205]

(a) Release mechanism of nonporous particle

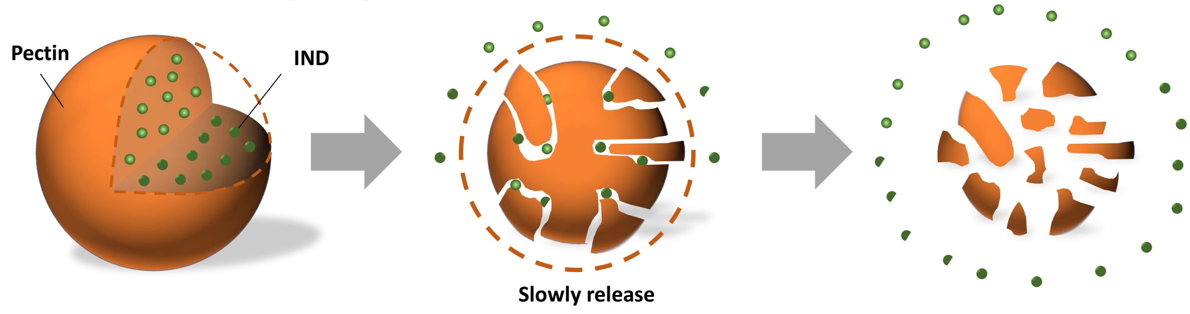

(b) Release mechanism of porous particle

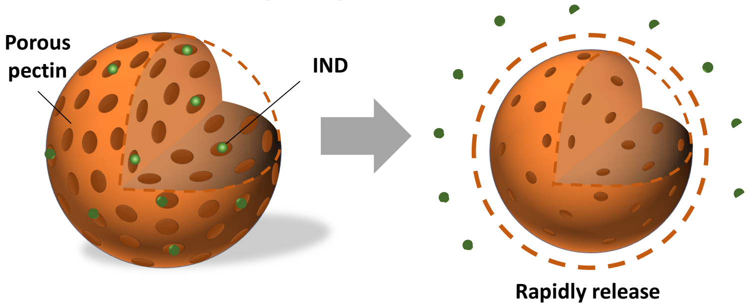

Figure 4.7: Schematic representation of drug release from (a) nonporous particles and (b) porous particles.

4.4 CONCLUSIONS

In summary, we have synthesized a series of porous IND-loaded pectin particles by template-assisted spray drying using $CaCO_3$ NPs as templates. Our work presents several advantages in the synthesis and application of the porous structure, notably achieving drug release in the colon for the model drug IND. First, this study created porous pectin particles using a natural polymer without any changes through a straightforward spray drying process. Since this technique is rapid, continuous, reproducible, and one-step, it is attractive both in laboratories and in the industrial setting. Thus, it shows significant promise for developing materials on a large-scale in the future. Second, the predominant drug release mechanism from porous pectin particles is Fickian diffusion, which is different from the combination of erosion and diffusion mechanism observed for nonporous particles. Thus, the porous structures of pectin appear to increase the specific surface area, which promotes a rapid drug release by shortening the diffusion path length to the media. According to the release profile, even porous P-IND-0.5-Af and P-IND-0-Af pectin particles had almost the same loading content; however, the release rate of P-IND-0.5-Af was twice as fast as that of P-IND-0-Af. Third, the rapid release rates can be controlled by varying the porous structure of pectin particles with different $CaCO_3$ NPs concentrations. As the $CaCO_3$ NPs concentration increased from P-IND-0.5-Af to P-IND-12-Af, the drug release rate also increased by up to three times. We perceive that these porous pectin particles will receive enormous attention for drug capture and release, and will be useful in many related fields as a specific region targeted drug delivery systems.

5

Conclusions and Future Perspectives

In recent advancements within the field of material science and biotechnology, the synthesis of porous particles has garnered significant attention due to their vast potential in various applications, including drug delivery systems, environmental remediation, and biochemical adsorption. Among the diverse range of materials being explored, pectin - a naturally derived polysaccharide - has emerged as a promising candidate due to its biocompatibility, biodegradability, and versatile functionalization capabilities. This study presented the synthesis of meso-/macroporous pectin particles employing a aerosol technique with the template assistance. The results indicated that controlling the concentration of the template can manipulate the physical properties of the particles, such as their specific surface area. With the favorable specific surface area of the porous structure combined with the biological activity of pectin, the porous pectin particles have demonstrated potential in protein adsorption with good accessibility and the ability to control rapid drug release. The highlighted conclusions are given as follow.

1. This thesis outlines the creation of meso-/macroporous pectin particles through a template-assisted spray-drying approach, employing PMMA and $CaCO_3$ as templates.

The study verifies the successful synthesis of porous pectin structures via Fourier-transform infrared spectroscopy (FT-IR) and zeta potential measurements, confirming that the pectin's intrinsic properties remain unaltered. The investigation further highlights how the initial droplet size in the spray-drying process affects the particles' morphology and dimensions. Specifically, PMMA templates yield wrinkled particles (PPT-P) with sizes ranging from 5 to 8 µm as the template/pectin mass ratio increases from 1 to 4. Conversely, using $CaCO_3$ templates produces spherical particles (PPT-C), with only minor size variations from 3 to 4 µm under the same conditions. The porous structure enhances the surface area values significantly compared to non-template-based pectin particles, particularly evident at a template/pectin ratio of 4, where PPT-C exhibits a superior surface area.

2. Further exploration into the effects of varying $CaCO_3$ to pectin weight ratios demonstrates a notable increase in specific surface area and total pore volume, attributed to enhanced pore formation. $CaCO_3$ also contributes calcium ions post-template removal, stabilizing the porous structure through the egg-box model. The resulting porous pectin particles using the weight ratio of $CaCO_3$ to pectin of 12 exhibit a remarkable increase in specific surface area value, making them highly effective for protein adsorption due to their abundant binding sites and interconnected pore network.

3. The research also delves into the synthesis of indomethacin-loaded porous pectin particles, emphasizing the efficiency of $CaCO_3$ nanoparticles as templates. This method not only retains the natural polymer's characteristics but also facilitates rapid, scalable, and reproducible material production. It is highlighted that the porous structures significantly increase the specific surface area, promoting swift drug release through Fickian diffusion - a contrast to the combined erosion and diffusion mechanism observed in nonporous particles. The study shows that adjusting the concentration of $CaCO_3$ nanoparticles can control the drug release rate, underscoring the potential of porous pectin particles in targeted drug delivery systems.

Overall, this comprehensive study demonstrates the versatility and potential of porous pectin particles synthesized through a template-assisted spray-drying method.

These findings suggest promising applications in drug delivery systems, protein and antibody purification, virus capture, and environmental micro- and nanoplastics recovery. The synthesis process, grounded in sustainability and scalability, presents a promising avenue for future industrial application and further research into the controlled release of active ingredients from porous pectin particles.

In addition, the precise control and regulation of pore size, along with the integration of interconnected pores, are of paramount importance for industrial applications. Accurate manipulation of pore dimensions is crucial for optimizing the surface area and enhancing the material functionality in various processes. Interconnected pore networks facilitate efficient mass transport, which is essential for applications such as catalysis, adsorption, and drug delivery. The ability to tailor pore size distribution and connectivity ensures that materials can meet specific performance criteria, thereby improving the efficacy and reliability of industrial processes. This meticulous control over porosity parameters not only enhances the physical properties of materials but also broadens its applicability across diverse industrial sectors.

A

SI: Synthesis of Porous Pectin Particles by a Template-Assisted Spray Drying

A.1 Precursor properties and droplet sizes

In this study, density (ρ) was calculated from the weight of 10.0 mL of each precursor solution and viscosity (η) was measured using an Ostwald viscometer (AS ONE Corporation, Japan). A Tantec FACE CBVP-Z automatic surface tensiometer (Kyowa Interface Science Co., Ltd., Japan) was used to measure the surface tension (σ) of the precursors to be fed into the spray dryer. The temperature of the laboratory room where experiments were performed was set to 20 °C. All measurements were carried out in triplicate to minimize error.

Table A.1: Properties of the precursors before spray drying (determined using Equation 2.1 in the main text).*

Sample	Density ρ (kg m^{-3})	Viscosity $\eta \times 10^{-3}$ (kg m^{-1}s^{-1})	Surface tension σ (kg s^{-2})	Droplet size D_d (μm)
PPT-0	1012.4 ± 7.2	7.3 ± 0.2	0.0572 ± 7.57	30.2 ± 0.2
PPT-C-4	1023.6 ± 12.7	14.5 ± 0.8	0.0590 ± 3.61	30.8 ± 0.2
PPT-P-4	991.1 ± 5.9	8.3 ± 0.3	0.0619 ± 4.58	33.4 ± 0.1

[*] Q_L (liquid flow rate) = 5.0×10^{-8} m^3 s^{-1}; Q_A (carrier gas flow rate) = 9.92×10^{-5} m^3 s^{-1}.

B

SI: Protein Adsorption Capacity of Porous Pectin Particles

B.1 SEM images of pectin-$CaCO_3$ composite particles

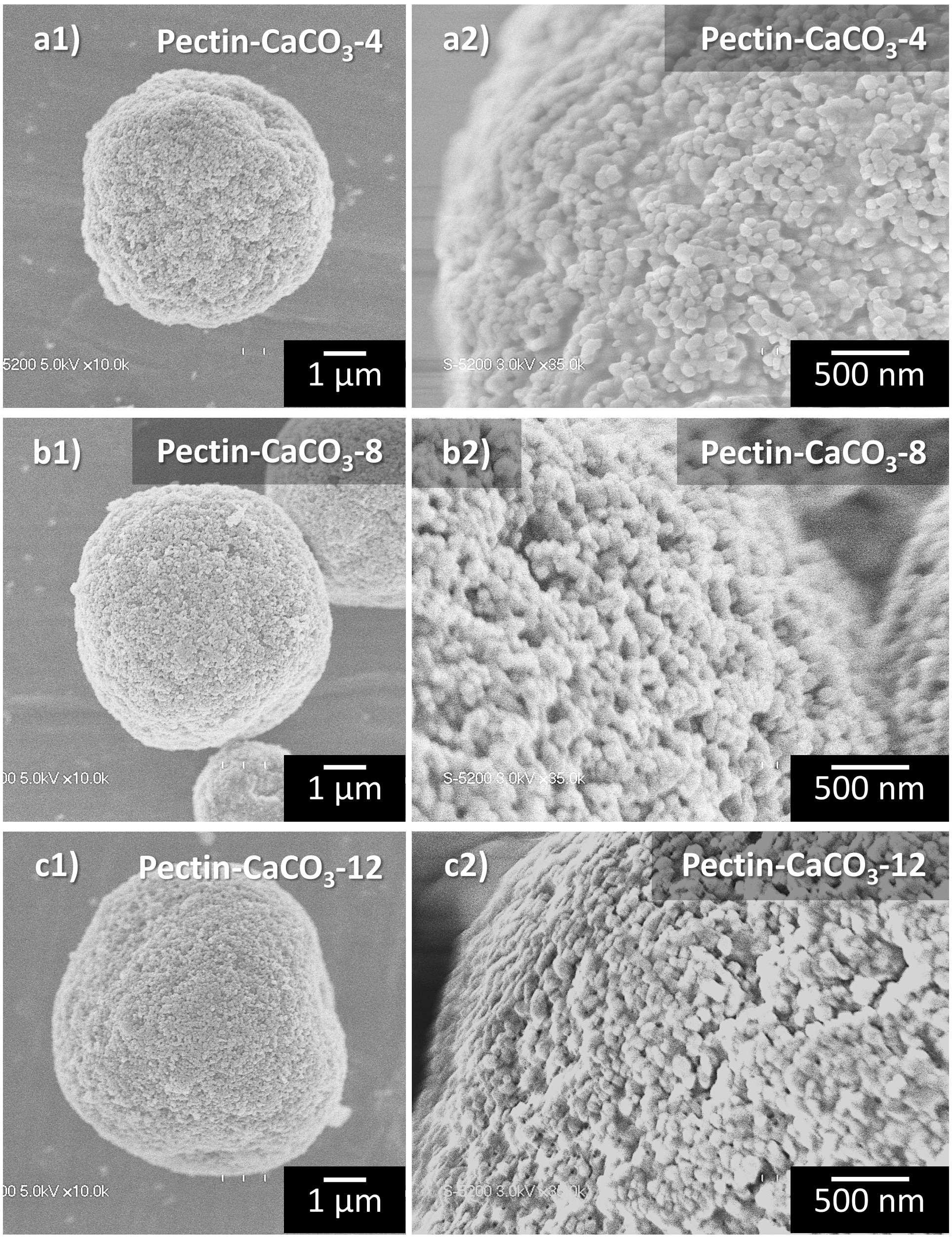

Figure B.1: SEM images of pectin-$CaCO_3$ composite particles before removing $CaCO_3$ template with weight ratios of $CaCO_3$ to pectin of (a1)–(a2) 4, (b1)–(b2) 8, and (c1)–(c2) 12. (a1), (b1), and (c1) are at magnification of ×10.0k and (a2), (b2), and (c2) are at magnification of ×35.0k.

B.2 FT-IR spectra

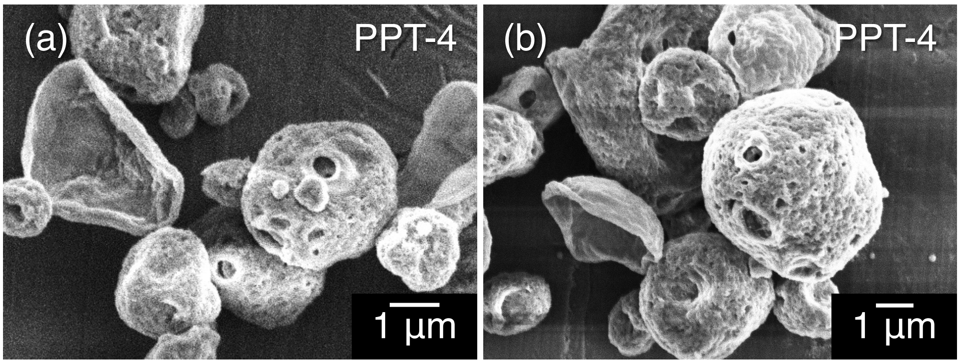

Figure B.2: SEM images of particles after using HCl to remove $CaCO_3$ template.

B.3 SEM images of particles using HCl to remove $CaCO_3$ templates

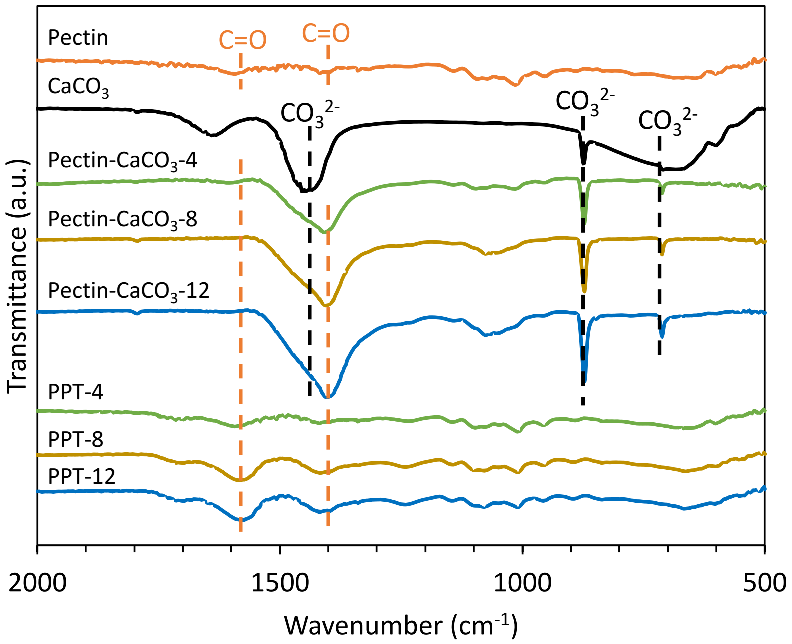

Figure B.3: FT-IR spectra of pectin, $CaCO_3$, pectin-$CaCO_3$ composite (before etching), and porous pectin particles (after etching).

B.4 Number of pores per unit sample surface area

The number of pores on the surface was counted based on SEM images for the same square micrometer of sample surface area. 300 particles observed in SEM images were used to count the number of pores. The results showed that when the $CaCO_3$ concentrations were increased from 4, 8, and 12 wt.%, the average number of pores per square micrometer increased from 32, 65, and 108, respectively.

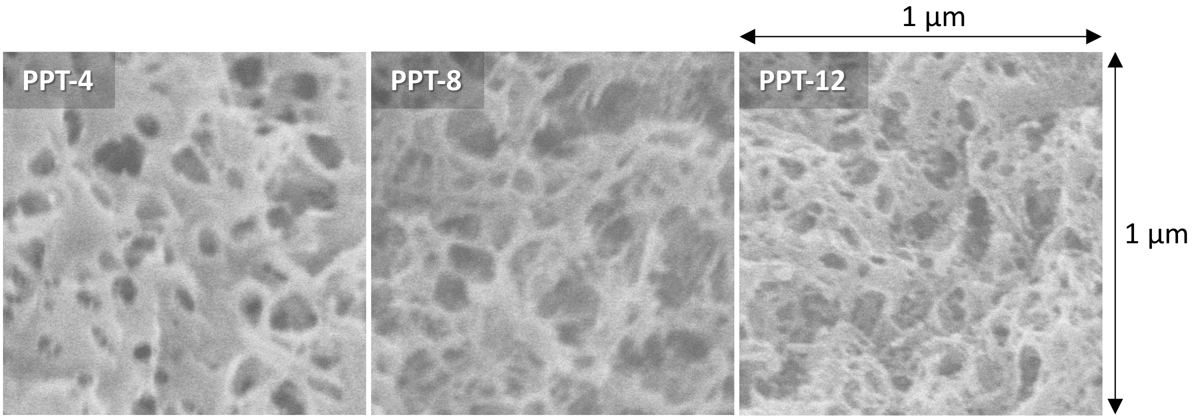

Average number of pores: 32

Average number of pores: 65

Average number of pores: 108

Figure B.4: Average number of pores per square micrometer.

B.5 Illustration of the egg-box model for pectin and calcium ions

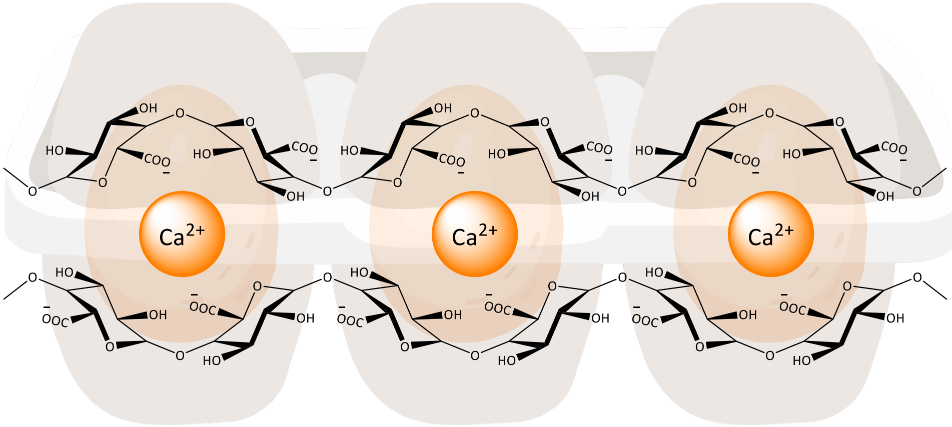

Figure B.5: Egg-box model for pectin and calcium ions.

B.6 Solubility of the porous pectin particles

B.6.1 Theory

A series of standard solutions of pectin was prepared. The absorbance of the standard solutions was measured and used to construct a calibration curve. Following Beer's Law, the slope and intercept of that line provided the relationship between the absorbance A and the concentration C:

$$A = \text{slope} \times C + \text{intercept} \tag{B.1}$$

An unknown (saturated) solution was then analyzed. Using the slope and intercept values (Equation B.1) and the absorbance of the unknown solution A_u, the concentration C_u was calculated by

$$C_u = \frac{A_u - \text{intercept}}{\text{slope}} \tag{B.2}$$

B.6.2 Calibration curve

A known concentration of pectin in DI water (stock solution) was prepared. The absorbance of the stock solution at the maximal wavelength was measured with an UV–Vis spectrophotometer (UV-2450, Shimadzu, Japan). Seven diluted solutions of the stock solution were prepared. Dilution was performed with DI water. A plot of the concentration versus the absorbance was constructed to yield a straight line (Figure B.6a). The values of the slope and intercept were calculated from this plot. The R^2 value was also determined, and the equation of the line was obtained for further assessment of the concentration of the saturated solution.

B.6.3 Concentration of the saturated solution

A saturated solution of macroporous pectin particles in DI water was prepared by dissolving the particles in a specific amount of DI water. To achieve the maximum solubility of the particles, the solution was stirred at 25 °C for 30 min. Once the particles attained the solubility limit, the saturated solution was centrifuged at 15,000 rpm for 10 min to obtain the clear supernatant. The absorbance of the saturated supernatant was measured. The concentration of the supernatant was calculated by Equation B.2, where the *slope* and *intercept* values were taken from the calibration curve previously constructed from Equation B.1. A_u is the measured absorbance of the saturated solution and C_u is the concentration of the saturated solution of pectin (mg mL^{-1}). The solubility of pectin is reported in percentage of dissolved particles in water (%).

B.6.4 Results

The results of the solubility of non-porous and porous pectin at 25 °C are shown in Figure B.6b. For the PPT-0 non-porous sample, the solubility showed that 97.0% of this sample was easily dissolved in water. It is reasonable that the solubility of this sample in water was extremely high, which agreed with a previous report, suggesting that pectin was soluble in water without the need for specific processing procedures.[206] However, the solubility of the PPT-4 porous sample was significantly lower. The data showed that only about 6.6% of the sample dissolved in water, which was 15 times lower than the nonporous sample. This improvement can be attributed to the egg-box model from the calcium ions formed after removing the template and pectin (Figure B.6c).[99]

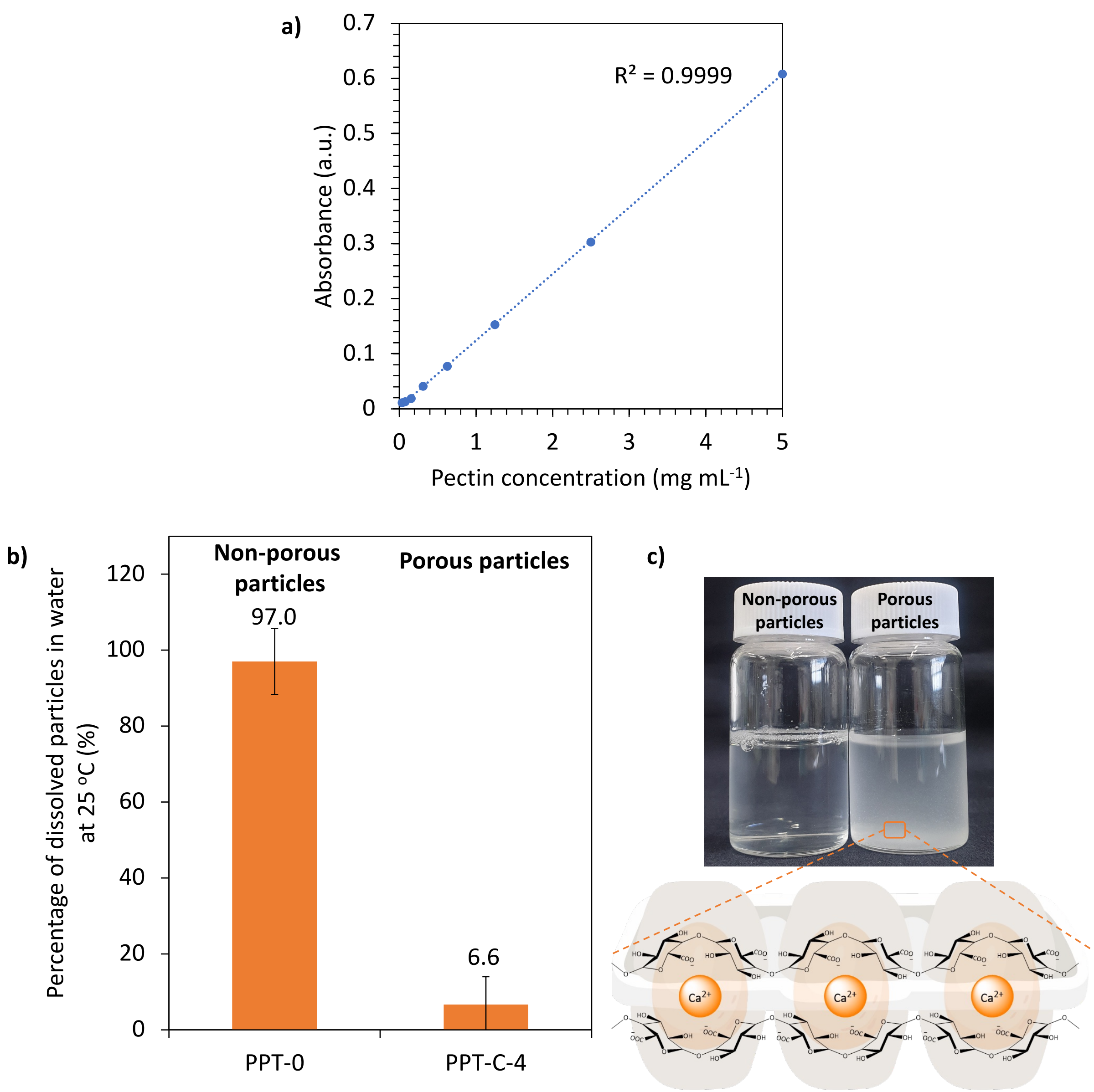

Figure B.6: (a) Pectin calibration curve at 270 nm. (b) Percentages of the PPT-0 and PPT-C-4 samples dissolved in water at 25 °C. (c) Image of non-porous particle PPT-0 and porous particle PPT-4 in water at 25 °C.

B.7 Determination of calcium ion contents in porous pectin particles by ICP–AES method

Inductively coupled plasma – atomic emission spectrometry (ICP–AES; ICPE–9820, Shimadzu Corporation, Kyoto, Japan) was used to measure calcium ion contents of porous pectin particles. 2.0 mg of porous pectin samples were completely dissolved in 10 mL nitric acid, and then ultrapure water was added to make 50 mL solutions. The calcium ion content was measured at 393.366 nm after the sample solution had been diluted 100–fold. Calibration curves were produced from 0 to 0.5 mg L^{-1} of calcium ions using standard solution (1000 mg L^{-1}; Kanto Chemical. Co. Inc., Tokyo, Japan). The weight percentage of calcium ion in the sample is determined from the measured calcium ion content and the initial sample content.

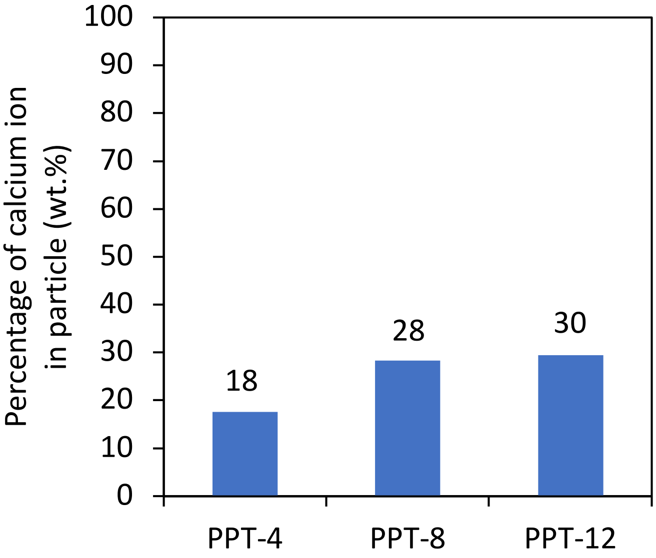

Figure B.7: Calcium ion contents of porous pectin particles PPT-4, PPT-8, and PPT-12.

B.8 Cross-sectional SEM images of pectin-$CaCO_3$ composite particle

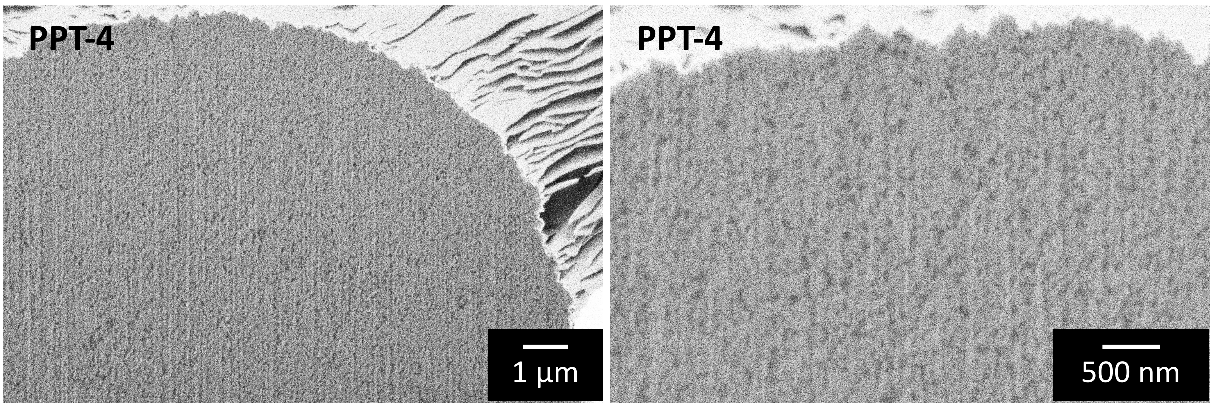

Figure B.8: Cross-sectional SEM images of pectin-$CaCO_3$-4 composite particle.

B.9 Calibration curve of the lysozyme concentration versus the absorbance

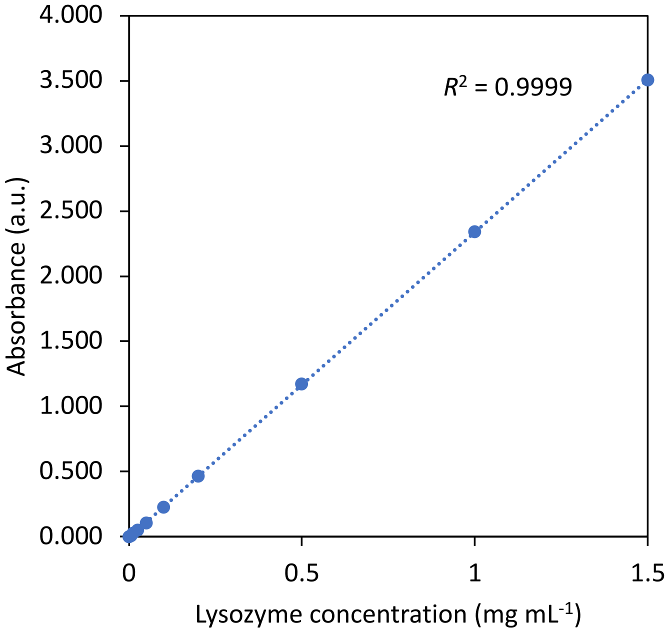

Figure B.9: Lysozyme calibration curve at 281 nm.

B.10 Calcium ion contents release in the media during the adsorption process

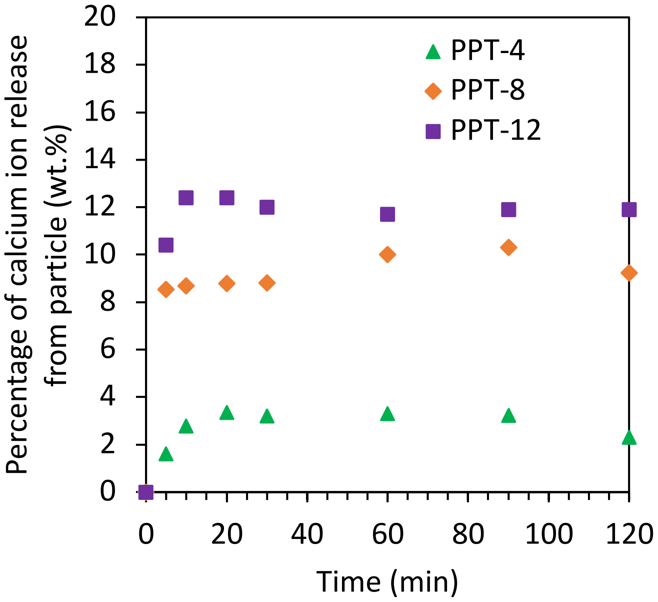

Figure B.10: Weight percentage of calcium ion release in the media as a function of time during the adsorption process.

B.11 Adsorption kinetic models

One of the most commonly used equations for adsorption on solid adsorbents is the pseudo-first-order rate equation:[207]

$$\ln(Q_e - Q_t) = \ln Q_e - k_1 t \tag{B.3}$$

where k_1 is the pseudo-first-order rate constant, and Qe and Qt are the adsorbed amounts (mg g^{-1}) at equilibrium and time t, respectively. The pseudo-first-order rate constant k_1 and equilibrium capacity Q_e can be determined from the slope and intercept of the plot of $\ln(Q_e - Q_t)$ versus t.

The linear form of the pseudo-second-order model used in this work is[208]

$$\frac{t}{Q_t} = \frac{1}{k_2 Q_e^2} + \frac{1}{Q_e} t \tag{B.4}$$

where k_2 is the pseudo-second-order rate constant of sorption (g mg^{-1} min^{-1}). The rate constant k_2 and equilibrium capacity Q_e can be calculated from the intercept and slope of the plot of t/Q_t versus t, respectively. If the pseudo-second-order model fits the experimental data, the plot gives a linear relationship, from which k_2 can be obtained.

The diffusion model proposed by Weber and Morris assists in better understanding of the transport stages of the adsorption process when adsorbate molecules move from the bulk to the solid surface.[209] The model equation is given by

$$Q_t = k_d t^{0.5} + l \tag{B.5}$$

where k_d is the intraparticle diffusion rate constant (mg g^{-1} min$^{-0.5}$) and l is the boundary layer thickness. The plot of Q_t versus $t_{0.5}$ usually occurs in two or more stages. The first stage is called the external surface adsorption or instantaneous adsorption stage. In this stage, there is an abrupt increase. The second stage indicates the slow adsorption step, where the rate is macropore and intraparticle-diffusion controlled.

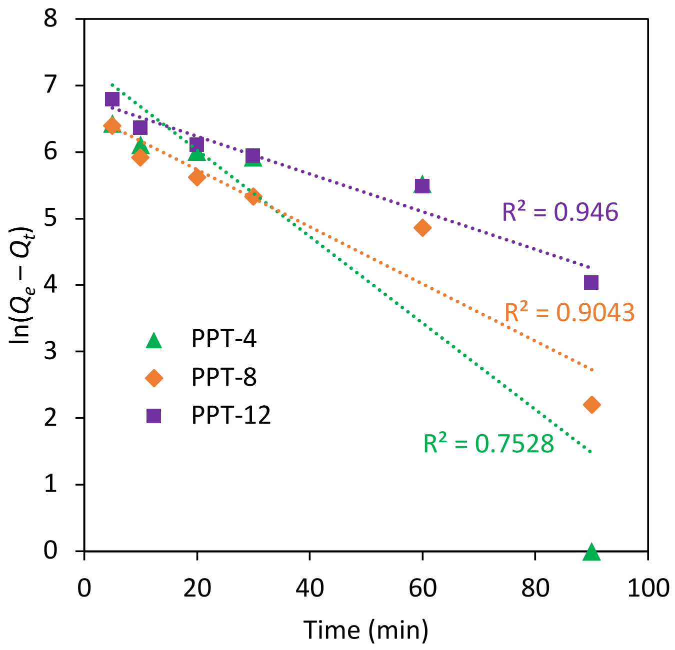

Figure B.11: Pseudo-first-order kinetic model plots for PPT-4, PPT-8, and PPT-12.

B.12 Relationship of adsorption capacity, specific surface area, and macropore volume of porous pectin particles

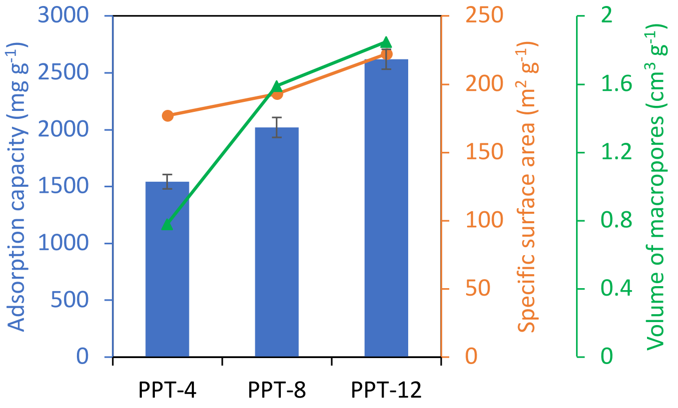

Figure B.12: Relationship of adsorption capacity, specific surface area, and macropore volume of porous pectin particles at different weight ratios of $CaCO_3$ to pectin of 4, 8, and 12.

B.13 Langmuir, Freundlich, and Temkin isotherms for lysozyme adsorption on PPT-12

The Langmuir isotherm assumes that adsorption occurs at a finite specific number of binding sites on the surface. This process is typically referred to as homogeneous adsorption and is applicable to biosorbents, whereby constant enthalpy and sorption activation energy are extracted from each molecule. The Langmuir equation is expressed as[210,211]

$$Q_e = \frac{Q_{\max} k_L C_e}{1 + k_L C_e} \tag{B.6}$$

The linear form of the Langmuir isotherm was used to prove that the Langmuir isotherm fitted the experimental data well:

$$\frac{C_e}{Q_e} = \frac{1}{k_L Q_{\max}} + \frac{C_e}{Q_{\max}} \tag{B.7}$$

where C_e is the equilibrium concentration of the protein in solution (mg L^{-1}), Q_e is the equilibrium amount of the protein adsorbed on the adsorbent (mg g^{-1}), Q_{max} is the maximum adsorption capacity of the adsorbent (mg g^{-1}), and k_L is the Langmuir isotherm association constant (mL mg^{-1}). The Langmuir isotherm model parameters (Q_{max} and k_L) calculated from the slope and intercept of the C_e versus C_e/Q_e plot shown in Figure B.13a are given in Table B.1.

The Freundlich isotherm assumes heterogeneous surface energies, and the energies become more heterogeneous as the value of the slope approaches zero. The Freundlich equation is generally expressed as[212]

$$Q_e = k_F C_e^{\frac{1}{n}} \tag{B.8}$$

It can be linearly expressed as

$$\ln Q_e = \ln k_F + \frac{1}{n} \ln C_e \tag{B.9}$$

where k_F is the Freundlich isotherm constant [(mg g^{-1})(mL mg^{-1})$^{1/n}$] and n is the adsorption intensity, which can be obtained from the intercept and slope of the ln C_e versus ln Q_e plot shown in Figure B.13b.

The Temkin isotherm assumes indirect interactions between the adsorbent and adsorbate molecules in the adsorption isotherms. The Temkin isotherm is expressed by the following equation:[213]

$$Q_e = \frac{RT}{b_T} \ln A_T + \frac{RT}{b_T} \ln C_e \tag{B.10}$$

where R is the gas constant (8.314 J mol^{-1} K^{-1}), T is the absolute temperature (K), and b_T is related to the heat of adsorption (J mol^{-1}). The plot of ln C_e versus Q_e (Figure B.13c) was used to calculate the Temkin isotherm parameters A_T and b_T (Table B.1).

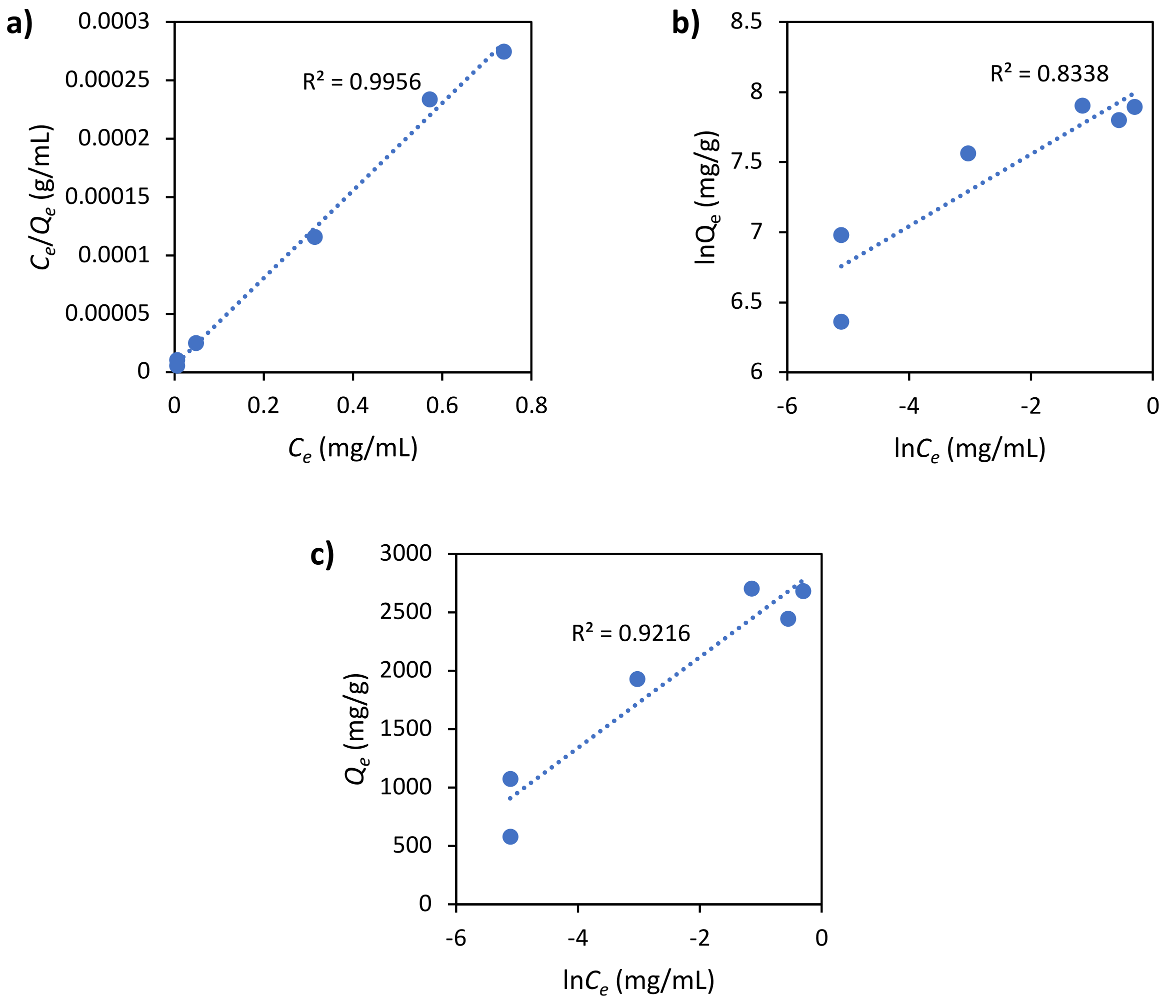

Figure B.13: (a) Langmuir, (b) Freundlich, and (c) Temkin isotherms for lysozyme adsorption on PPT-12 at 25 °C.

Table B.1: Langmuir, Freundlich, and Temkin isotherm model parameters for PPT-12.

Isotherm model	Parameter	
Langmuir isotherm	k_L (mL mg^{-1})	66.3
	$Q_m ax$ (mg g^{-1})	2666
	R^2	0.9956
Freundlich isotherm	k_F [(mg g^{-1})(mL mg^{-1})$^{1/\mathrm{n}}$]	3210.4
	N	3.9
	R^2	0.8338
Temkin isotherm	A_T (mL g^{-1})	1724.9
	b_T (J mol^{-1})	6.4
	R^2	0.9216

B.14 Surface packing density of the lysozyme

The used lysozyme in this research has a molecular weight (MW) of 16000 g mol^{-1}. From the molecular weight of lysozyme, adsorption capacity, and specific surface area, the number of lysozyme molecules per unit surface area (packing density of lysozyme) was calculated by the following formula.

The number of lysozyme molecules [molecule nm^2]

$$= \frac{\text{Adsorption capacity [g-lysozyme g-pectin}^{-1}]}{\text{Specific surface areas of pectin particles [nm}^2\text{ g-pectin}^{-1}]} \times \frac{1}{\text{MW of lysozyme [g mol}^{-1}]} \times 6.02 \times 10^{23}\ [\text{molecule mol}^{-1}]$$

Applying the above formula to porous pectin particles PPT-12 that had the value of adsorption capacity of 2621 mg g^{-1}, and specific surface area of 222.3 m^2 g^{-1}, the number of lysozyme molecules was calculated as follow;

The number of lysozyme molecules

$$= \frac{2.621\ [\text{g-lysozyme g-pectin}^{-1}]}{222.3 \times 10^{18}\ [\text{nm}^2\text{ g-pectin}^{-1}]} \times \frac{1}{16000\ [\text{g mol}^{-1}]} \times 6.02 \times 10^{23}\ [\text{molecule mol}^{-1}]$$

$$= 0.4\ [\text{molecule nm}^2]$$

In porous pectin particles PPT-12, the results showed that there were 0.4 lysozyme molecule per square nanometer, which means there was about 1 lysozyme molecule per 3 nm^2 adsorbent.

C

SI: Porous Pectin Particles as a Colon Targeted Drug Delivery System

C.1 Calibration curve of absorbances versus IND concentrations

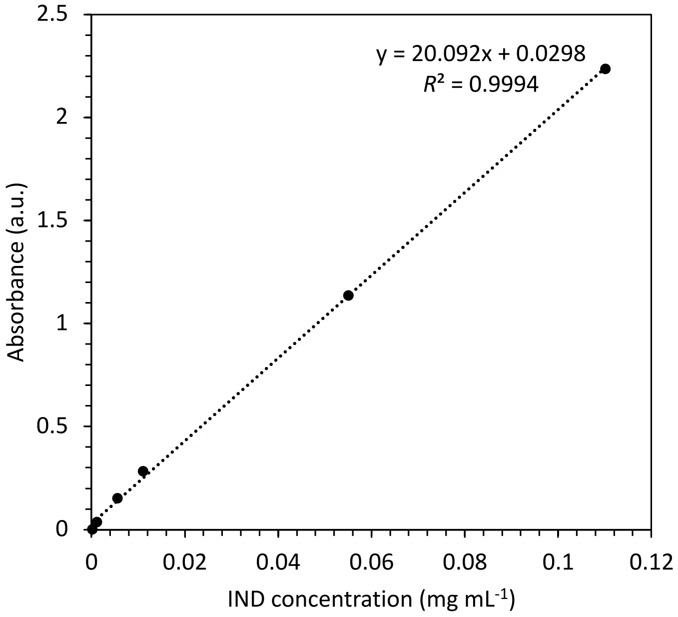

Figure C.1: The calibration curve of absorbances versus IND concentrations.

C.2 Number of mesopores and macropores per unit sample surface area

The number of mesopores and macropores (pore size over 50 nm) on the surface was counted based on SEM images for the same square micrometer of sample surface area. 300 particles observed in SEM images were used to count the number of pores. The results showed that when the $CaCO_3$ NPs concentrations were increased from 0.5, 1, and 12 wt.%, the average number of mesopores and macropores per square micrometer increased from 7, 16, and 110, respectively.

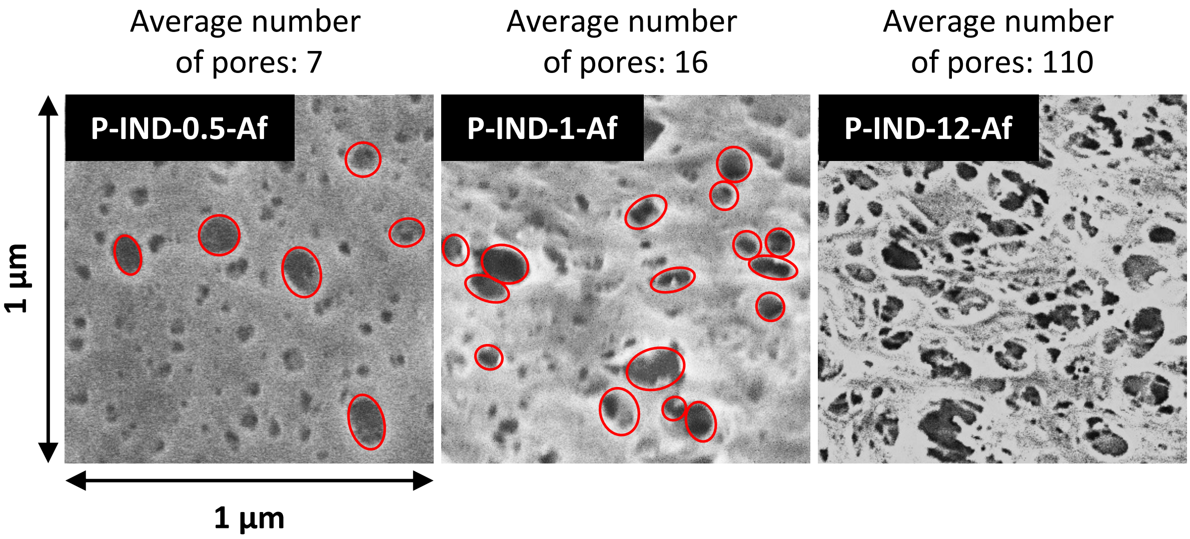

Figure C.2: Average number of mesopores and macropores (pore size over 50 nm) per square micrometer.

C.3 Particle size distribution, nitrogen adsorption – desorption, and pore size distribution

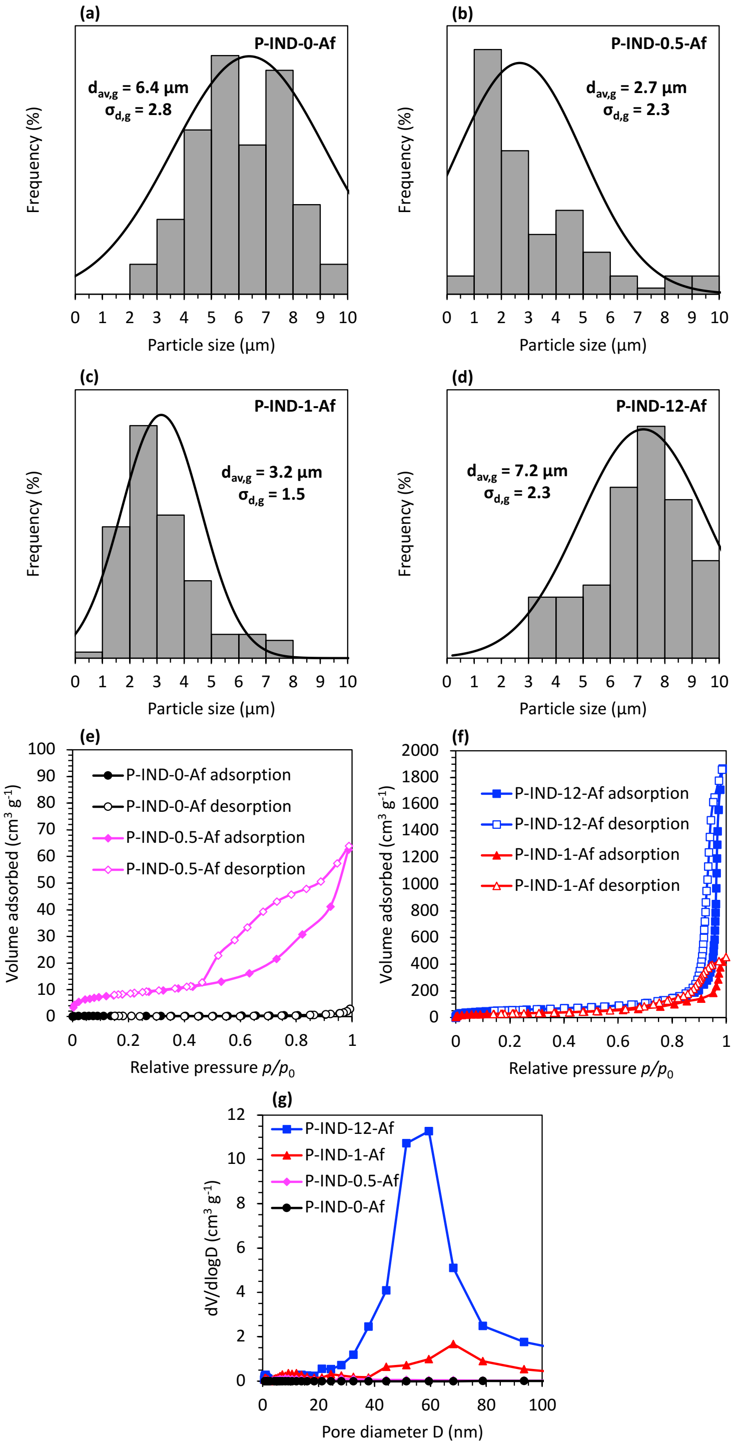

Figure C.3: Particle size distributions of (a) P-IND-0-Af, (b) P-IND-0.5-Af, (c) P-IND-1-Af, and (d) P-IND-12-Af. dav,g is the geometric mean, and σd,g is the geometric standard deviation of particles. (e), (f) Nitrogen adsorption – desorption isotherm, and (g) pore size distribution of IND-loaded pectin particles.

C.4 A suggested model of the interactions between IND and pectin

IND is a nonsteroidal anti-inflammatory medicine frequently used to treat inflammation-related fever, discomfort, and stiffness.[214] However, it is a challenge to load IND because it has negatively charged, similar to pectin in neutral media.[215] A suggested model of the interactions between IND and pectin in drug-loaded particles schematically depicted in Figure C.4 to better understand the binding between the drug and carrier. When IND is mixed with pectin, the intertwined network structure is formed through hydrogen bonding between IND and pectin. The hydrophobic CH-π effects provide another physically cross-linked network in addition to the aforementioned physical interactions. This interaction generally contains CH groups of the hydrophobic plaques in pectin and π electron density of aromatic compounds in IND. Thus, the IND drug is physically embedded via hydrogen bonding and hydrophobic CH-π effect during the formation of P-IND particles.

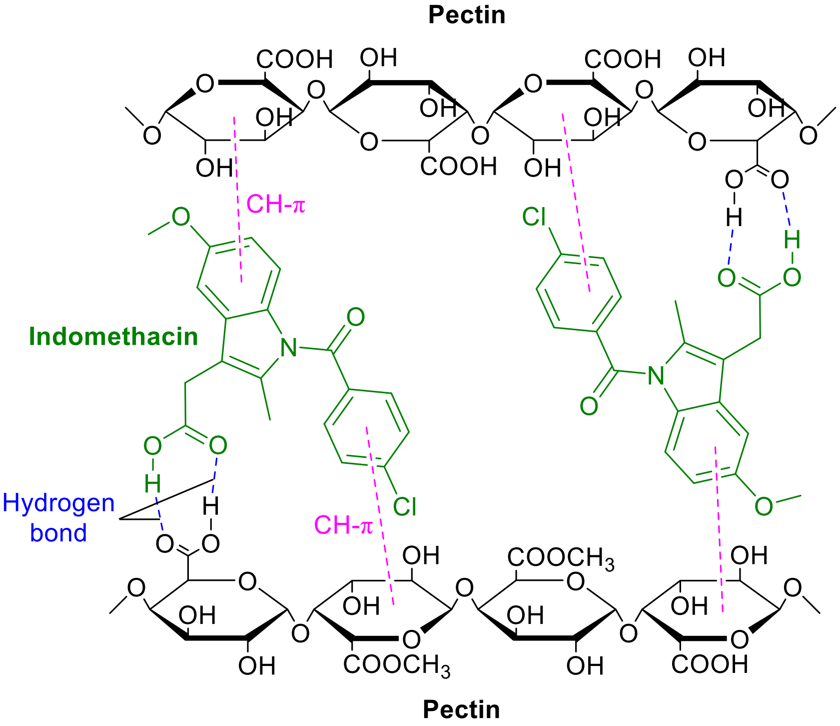

Figure C.4: Suggested model of the interactions between IND and pectin in drug-loaded particles.

C.5 XRD patterns of IND-loaded pectin particles

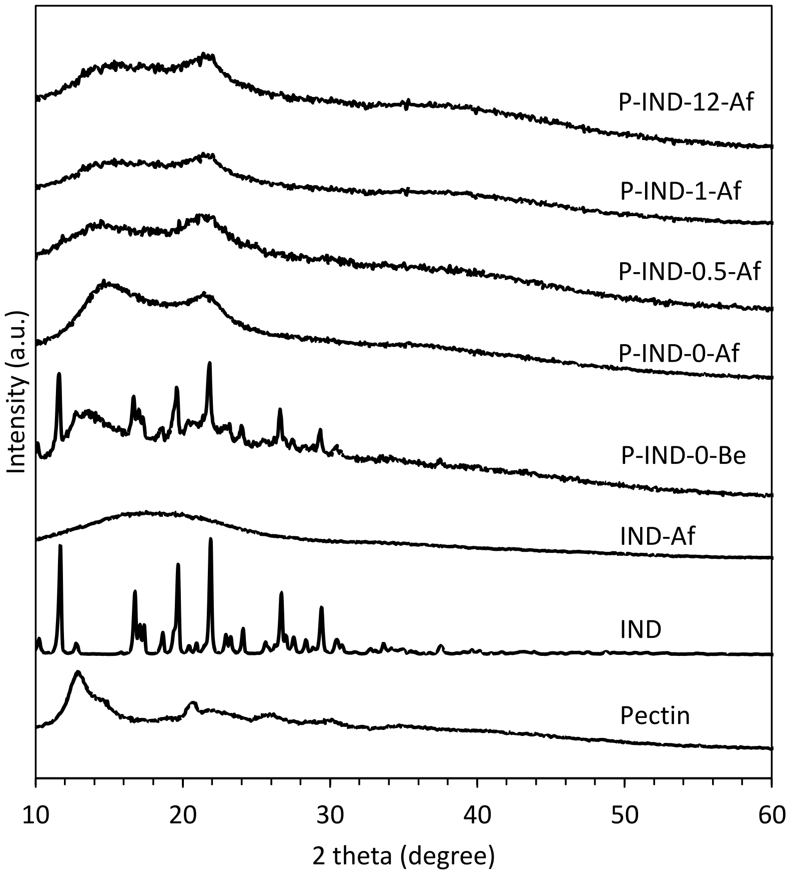

Figure C.5: XRD patterns of pectin, IND, and IND-loaded pectin particles.

C.6 Interaction of IND with $CaCO_3$

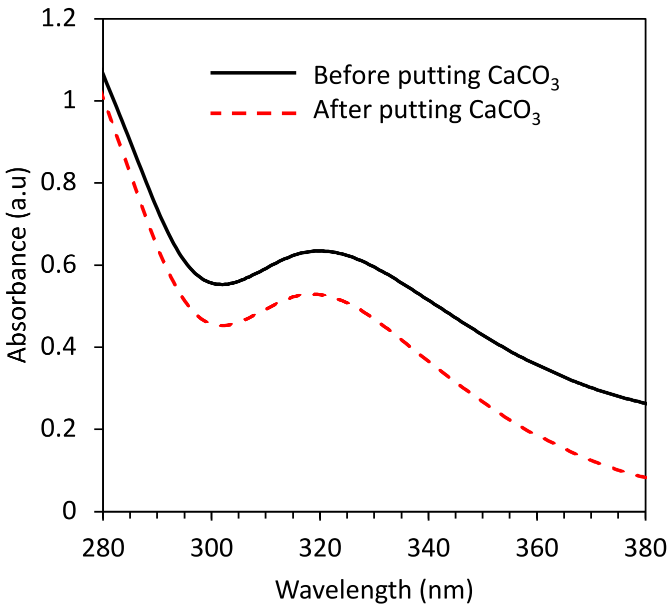

Figure C.6: The absorbance of IND before and after adding $CaCO_3$.

C.7 Release kinetic models

C.7.1 Zero-Order Model

To fit the mechanism of constant drug release from a drug delivery system, zero-order kinetic is used. The cumulative drug release is plotted against time in order to investigate the drug release kinetics data from the in vitro dissolution study.The slope of this model indicates the zero-order rate constant, and the plot's correlation coefficient will determine whether or not the drug release corresponds to zero-order kinetics.[216,217] Equation C.1 can be used to measure drug release from the dosage form in accordance with pharmacokinetics principles:

$$C_t = C_0 - k_0 t \tag{C.1}$$

where C_t is the concentration of drug in the release medium at time t, C_0 is the initial concentration of drug at time equal to zero, and k_0 is the zero-order rate constant in concentration per time units.

C.7.2 First-Order Model

The drug release in pharmaceutical dosage forms containing water-soluble drugs in porous matrices is analyzed using the first-order model.[216,217] Equation C.2 could represent the drug release that occurs following first-order kinetics:

$$\ln C_t = \ln C_0 - k_1 t \tag{C.2}$$

where, C_t is the concentration of drug released at time t, C_0 is the initial concentration of drug and k_1 is first order constant. In this model the graphical representation of the lnC_t versus time will be linear with a slope equal to k_1.

The dosage forms that adhere to this model include those that release the drug in a proportional manner to the quantity released per unit of time and contain a drug that is water-soluble.

C.7.3 Higuchi Model

Higuchi developed mathematical models in 1961 to investigate the release of drugs in a solid matrix that are water-soluble and sparingly soluble.[218] Equation C.3 describes the dissolution from a system with a homogeneous matrix:

$$C_t = k_H t^{0.5} \tag{C.3}$$

where C_t is the concentration of drug released in time t, k_H is the Higuchi dissolution constant. Higuchi describes drug release as a diffusion process founded in the Fick's law. For diffusion-controlled process a plot of C_t versus square root of time is linear with a slope equal to the Higuchi constant.

C.7.4 Korsmeyer-Peppas Model

Korsmeyer and Peppas introduced forth a simple equation describes the drug release from a polymeric system and decides which sort of dissolution, the equation can be represented by Equation 4.4 and Equation C.4:

$$\ln\left(\frac{C_t}{C_\infty}\right) = \ln k_{KP} + n \ln t \tag{C.4}$$

where C_t is the concentration of the drug in the release solution at time t; C_∞ is the equilibrium concentration of the drug in the release solution; t is the release time; k_{KP} is the kinetic rate constant; n is the release exponent. A graph of $\ln(C_t/C_\infty)$ against $\ln t$ was plotted to explore release kinetics. The slope, which gives n value, is used to classify different release mechanisms, as given in Table C.1.[219]

Table C.1: Different release mechanisms according to the release exponent n

Release exponent (n)	Drug transport mechanism	Drug release mechanism	Rate as a function of time
$n < 0.45$	Quasi-Fickian diffusion	Diffusion	t^n
$n = 0.45$	Fickian diffusion	Diffusion	$t^{0.5}$
$0.45 < n < 0.89$	Non-Fickian diffusion (anomalous)	Both erosion and diffusion	t^{n-1}
$n = 0.89$	Case II transport	Zero-order release	Time-independent
$n > 0.89$	Super case II transport	Degradation	t^{n-1}

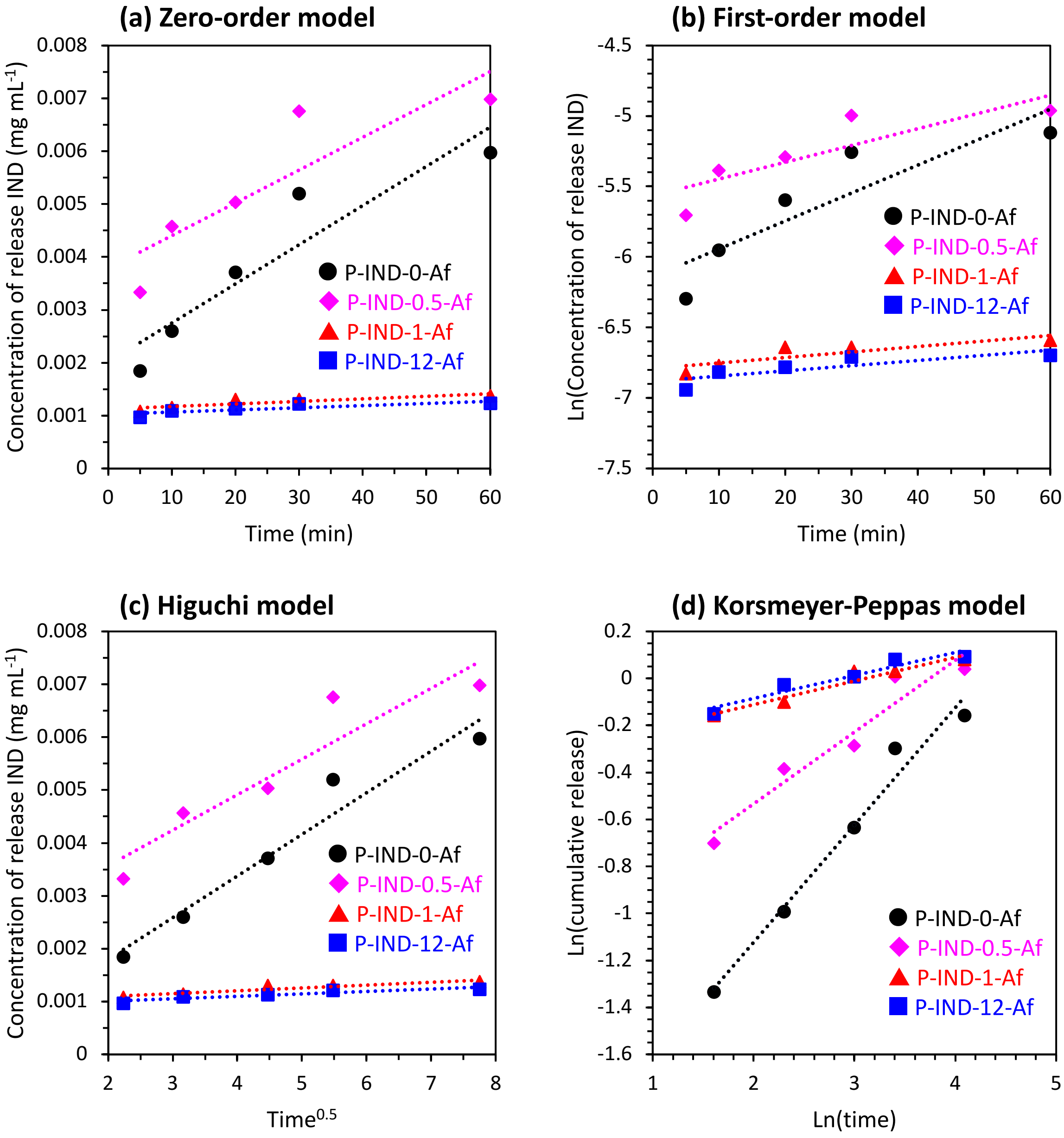

Figure C.7: Calcium ion contents of porous pectin particles PPT-4, PPT-8, and PPT-12.

References

[1] Joana T. Pinto, Eva Faulhammer, Johanna Dieplinger, Michael Dekner, Christian Makert, Marco Nieder, and Amrit Paudel. Progress in Spray-Drying of Protein Pharmaceuticals: Literature Analysis of Trends in Formulation and Process Attributes. *Drying Technology*, 39:1415–1446, 8 2021.

[2] Mani Ordoubadi, Florence K. A. Gregson, Omar Melhem, David Barona, Rachael E. H. Miles, Dexter D'Sa, Sandra Gracin, David Lechuga-Ballesteros, Jonathan P. Reid, Warren H. Finlay, and Reinhard Vehring. Multi-Solvent Microdroplet Evaporation: Modeling and Measurement of Spray-Drying Kinetics with Inhalable Pharmaceutics. *Pharmaceutical Research*, 36:100, 7 2019.

[3] Mercy Nani and Kiruba Krishnaswamy. Circular Economy for Food Industry Waste: Development and Characterization of Spray-Dried Acid Whey Encapsulated in Millet Matrix. *ACS Food Science & Technology*, 3:123–133, 1 2023.

[4] Songhua Wu, Xiaofei Xing, Dan Wang, Jianzheng Zhang, Junmei Chu, Chengcheng Yu, Zhiting Wei, Mingliang Hu, Xin Zhang, and Zhenxing Li. Highly Ordered Hierarchically Macroporous MIL-125 with High Specific Surface Area for Photocatalytic CO_2 Fixation. *ACS Sustainable Chemistry & Engineering*, 8:148–153, 1 2020.

[5] Yuxin Hu, Yingjun Qiao, Zhengwei Xie, Lin Li, Meizhen Qu, Wenjing Liu, and Gongchang Peng. Water-Soluble Polymer Assists Multisize Three-Dimensional Microspheres as a High-Performance Si Anode for Lithium-Ion Batteries. *ACS Applied Energy Materials*, 4:9673–9681, 2021.

[6] Xiangcheng Zhang, Yi Zhang, Zhikai Yu, Xiangru Wei, Winston Duo Wu, Xiaoning Wang, and Zhangxiong Wu. Facile Synthesis of Mesoporous Anatase/Rutile/Hematite Triple Heterojunctions for Superior Heterogeneous Photo-Fenton Catalysis. *Applied Catalysis B: Environmental*, 263:118335, 4 2020.

[7] Weili An, Peng He, Zongzhou Che, Chengmao Xiao, Eming Guo, Chunlei Pang, Xueqin He, Jianguo Ren, Guohui Yuan, Ning Du, Deren Yang, Dong-Liang Peng, and Qiaobao Zhang. Scalable Synthesis of Pore-Rich Si/C@C Core–Shell-Structured Microspheres for Practical Long-Life Lithium-Ion Battery Anodes. *ACS Applied Materials & Interfaces*, 14:10308–10318, 3 2022.

[8] Ana I. Bourbon, Letricia Barbosa-Pereira, António A. Vicente, Miguel A. Cerqueira, and Lorenzo Pastrana. Dehydration of Protein Lactoferrin-Glycomacropeptide Nanohydrogels. *Food Hydrocolloids*, 101:105550, 2020.

[9] Yuting Tang, Herbert B. Scher, and Tina Jeoh. Industrially Scalable Complex Coacervation Process to Microencapsulate Food Ingredients. *Innovative Food Science and Emerging Technologies*, 59:102257, 2020.

[10] Yilun Weng, Supun Ranaweera, Da Zou, Anna Cameron, Xiaojing Chen, Hao Song, and Chun-Xia Zhao. Alginate Particles for Enzyme Immobilization Using Spray Drying. *Journal of Agricultural and Food Chemistry*, 70:7139–7147, 6 2022.

[11] Filipa Guerreiro, Jorge F. Pontes, Ana M. Rosa da Costa, and Ana Grenha. Spray-Drying of Konjac Glucomannan to Produce Microparticles for an Application as Antitubercular Drug Carriers. *Powder Technology*, 342:246–252, 2019.

[12] Neema Pandey, Bhashkar Singh Bohra, Himani Tiwari, Mintu Pal, Pushpa Bhakuni Negi, Anirban Dandapat, S. P.S. Mehta, and Nanda Gopal Sahoo. Development of Biodegradable Chitosan/Graphene Oxide Nanocomposite via Spray Drying Method for Drug Loading and Delivery Application. *Journal of Drug Delivery Science and Technology*, 74:103555, 2022.

[13] Archana Mishra, Vipul K. Pandey, Bhavani S. Shankar, and Jose S. Melo. Spray Drying as an Efficient Route for Synthesis of Silica Nanoparticles-Sodium Alginate Biohybrid Drug Carrier of Doxorubicin. *Colloids and Surfaces B: Biointerfaces*, 197:111445, 2021.

[14] Bence Sipos, Ildikó Csóka, Rita Ambrus, Zsuzsanna Schelz, István Zupkó, György Tibor Balogh, and Gábor Katona. Spray-dried indomethacin-loaded polymeric micelles for the improvement of intestinal drug release and permeability. *European Journal of Pharmaceutical Sciences*, 174:106200, 2022.

[15] Pu Wang, Zhongti Sun, Hui Liu, Zhi Wen Gao, Jianguo Hu, Wan Jian Yin, Qingqing Ke, and Hugh Lu Zhu. Strategic synthesis of sponge-like structured SiO_x@C@CoO multifunctional composites for high-performance and stable lithium-ion batteries. *Journal of Materials Chemistry A*, 9:18440–18453, 2021.

[16] Wenyang Zhou, Qinghuang Lian, Xiaokai Huang, Weiqiang Ding, Chunhai Jiang, Zhimin Zou, and Xiaodong Su. Introducing SiC/C dual-interface on porous silicon anode by a conventional exothermic displacement reaction for improved cycle performance. *Journal of Power Sources*, 508:230326, 2021.

[17] Canliang Ma, Zairan Wang, Yun Zhao, Yong Li, and Jing Shi. A novel raspberry-like yolk-shell structured Si/C micro/nano-spheres as high-performance anode materials for lithium-ion batteries. *Journal of Alloys and Compounds*, 844:156201, 2020.

[18] Bin Xiao, Wen Hai Zhang, Hai Feng Xia, Zhi Teng Wang, Lin Bo Tang, Chang Sheng An, Zhen Jiang He, Hui Tong, and Jun Chao Zheng. $V_2(PO_4)O$/C@CNT hollow spheres with a core-shell structure as a high performance anode material for lithium-ion batteries. *Materials Chemistry Frontiers*, 3:456–463, 2019.

[19] Guihong Mao, Fangming Xiao, Liming Zeng, Renheng Tang, Jian Li, Qing Zhou, and Ying Wang. Improvement of cycle performance of the high nickel cathode

material $LiNi_{0.88}Co_{0.07}Al_{0.05}O_2$ for lithium-ion batteries by the spray drying of V_2O_5. *Journal of Alloys and Compounds*, 892:162161, 2022.

[20] Yi De Tsai, Jeng Ywan Shih, Ying Jeng James Li, Tai Feng Hung, Li Fan Hsu, Sayee Kannan Ramaraj, Rajan Jose, Chelladurai Karuppiah, and Chun Chen Yang. Effect of Single-Walled Carbon Nanotube Sub-carbon Additives and Graphene Oxide Coating for Enhancing the 5 V $LiNi_{0.5}Mn_{1.5}O_4$ Cathode Material Performance in Lithium-Ion Batteries. *ACS Sustainable Chemistry and Engineering*, 10:16709–16724, 2022.

[21] Guifang Zhang, Lantian Ren, Dianbo Ruan, Yu Sun, Jiarui Chen, and Zhiqiang Shi. Green and efficient synthesis of $LiNi_{0.8}Co_{0.1}Mn_{0.1}O_2$ cathode material with outstanding electrochemical performance by spray drying method. *Ionics*, 27:3231–3237, 2021.

[22] Xiaoming Xie, Baichao Zhang, Guorong Hu, Ke Du, Jiahui Wu, Yongzhi Wang, Zhanggen Gan, Ju Fan, Haodong Su, Yanbing Cao, and Zhongdong Peng. A new route for green synthesis of $LiFe_{0.25}Mn_{0.75}PO_4$/C@rGO material for lithium ion batteries. *Journal of Alloys and Compounds*, 853:157106, 2021.

[23] Zhenfei Li, Xin Ren, Yi Zheng, Weichao Tian, Liwei An, Jiachen Sun, Ruqian Ding, Lizhi Wen, and Guangchuan Liang. Effect of Ti doping on $LiFePO_4$/C cathode material with enhanced low-temperature electrochemical performance. *Ionics*, 26:1599–1609, 2020.

[24] Binhua Huang, Dongqing Liu, Lihan Zhang, Kun Qian, Kai Zhou, Xingke Cai, Feiyu Kang, and Baohua Li. An Efficient Synthetic Method to Prepare High-Performance Ni-rich $LiNi_{0.8}Co_{0.1}Mn_{0.1}O_2$ for Lithium-Ion Batteries. *ACS Applied Energy Materials*, 2:7403–7411, 2019.

[25] Hao Sun, Guilan Li, Anding Xu, Zhiguang Xu, and Songping Wu. Sulfur-doped hollow soft-balled mesoporous carbon particles as ultra-fast, durable hosts for potassium storage. *Journal of Alloys and Compounds*, 906:164311, 2022.

[26] Xiao Dong He, Jia Ying Liao, Ting Chen, Li Ming Zhang, Xiang Ding, Jun Ru Wang, Shuo Wang, Zhao Yin Wen, and Chun Hua Chen. Spray drying derived wrinkled pea-shaped carbon-matrixed KVP_2O_7 as a cathode material for potassium-ion batteries. *Journal of Alloys and Compounds*, 884:161126, 2021.

[27] Zhuang Hu, Ruijie Zhang, Changling Fan, Xunlin Liu, Peng Gao, Weihua Zhang, Zhixiao Liu, Shaochang Han, Jinshui Liu, and Jilei Liu. Synergistic Effect, Structural and Morphology Evolution, and Doping Mechanism of Spherical Br-Doped $Na_3V_2(PO_4)_2F_3/C$ toward Enhanced Sodium Storage. *Small*, 18:2201719, 2022.

[28] Gabriel Rodrigues de Almeida Neto, Cesar Augusto Gonçalves Beatrice, and Luiz Antonio Pessan. Spray-dried composite microparticles of polyetherimide and $LaNi_5$ as a versatile material for hydrogen storage applications. *International Journal of Hydrogen Energy*, 47:16996–17009, 2022.

[29] Young Hwan Kim, Byung Hoon Park, Yeon Jun Choi, Geon Woo Lee, Hyun Kyung Kim, and Kwang Bum Kim. Compact graphene powders with high volumetric capacitance: Microspherical assembly of graphene via surface modification using cyanamide. *Energy Storage Materials*, 24:351–361, 2020.

[30] Aadithya Jeyaranjan, Tamil Selvan Sakthivel, Craig J. Neal, and Sudipta Seal. Scalable ternary hierarchical microspheres composed of $PANI/rGO/CeO_2$ for high performance supercapacitor applications. *Carbon*, 151:192–202, 2019.

[31] Yilun Huang, Yunkai Shi, Qianming Gong, Mouyi Weng, Yuyao Li, Jianning Gan, Dazhi Wang, Yang Shao, Ming Zhao, Daming Zhuang, Ji Liang, Feng Pan, Hongwei Zhu, and Cewen Nan. Scalable preparation of hierarchical porous activated carbon/graphene composites for high-performance supercapacitors. *Journal of Materials Chemistry A*, 7:10058–10066, 2019.

[32] Gaofeng Zhu, Yang Jin, and Mingqiao Ge. Efficiently Enhanced Fenton-Like Reaction via $CuO@\gamma\text{-}Al_2O_3$ Particles for the Catalytic Hydrogen Peroxide Degrada-

tion of Polyvinyl Alcohol, Rhodamine-B, and Reactive red X-3B over a Wide pH Range. *Water, Air, & Soil Pollution*, 233:229, 7 2022.

[33] Bjarne Kreitz, Aurina Martínez Arias, Jan Martin, Alfred Weber, and Thomas Turek. Spray-Dried Ni Catalysts with Tailored Properties for CO_2 Methanation. *Catalysts*, 10:1410, 12 2020.

[34] Dingcai Wu, Fei Xu, Bin Sun, Ruowen Fu, Hongkun He, and Krzysztof Matyjaszewski. Design and Preparation of Porous Polymers. *Chemical Reviews*, 112:3959–4015, 7 2012.

[35] Xin Du and Junhui He. Fine-Tuning of Silica Nanosphere Structure by Simple Regulation of the Volume Ratio of Cosolvents. *Langmuir*, 26:10057–10062, 6 2010.

[36] Qi Lei, Jimin Guo, Achraf Noureddine, Aixia Wang, Stefan Wuttke, C. Jeffrey Brinker, and Wei Zhu. Sol–Gel-Based Advanced Porous Silica Materials for Biomedical Applications. *Advanced Functional Materials*, 30:1909539, 10 2020.

[37] Haiping Jia, Xiaolin Li, Junhua Song, Xin Zhang, Langli Luo, Yang He, Binsong Li, Yun Cai, Shenyang Hu, Xingcheng Xiao, Chongmin Wang, Kevin M. Rosso, Ran Yi, Rajankumar Patel, and Ji-Guang Zhang. Hierarchical porous silicon structures with extraordinary mechanical strength as high-performance lithium-ion battery anodes. *Nature Communications*, 11:1474, 3 2020.

[38] Soon Eon Bae, Jun Sik Son, Kwideok Park, and Dong Keun Han. Fabrication of covered porous PLGA microspheres using hydrogen peroxide for controlled drug delivery and regenerative medicine. *Journal of Controlled Release*, 133:37–43, 1 2009.

[39] Yi Wei, Yuxia Wang, Huixia Zhang, Weiqing Zhou, and Guanghui Ma. A novel strategy for the preparation of porous microspheres and its application in peptide drug loading. *Journal of Colloid and Interface Science*, 478:46–53, 9 2016.

[40] Miaomiao Zhou, Lan Shen, Xiao Lin, Yanlong Hong, and Yi Feng. Design and pharmaceutical applications of porous particles. *RSC Advances*, 7:39490–39501, 2017.

[41] Jarno Salonen, Ann M. Kaukonen, Jouni Hirvonen, and Vesa-Pekka Lehto. Mesoporous Silicon in Drug Delivery Applications. *Journal of Pharmaceutical Sciences*, 97:632–653, 2 2008.

[42] Annie M. Rahmatika, Weilin Yuan, Aditya F. Arif, Ratna Balgis, Keita Miyajima, Gopinathan M. Anilkumar, Kikuo Okuyama, and Takashi Ogi. Energy-Efficient Templating Method for the Industrial Production of Porous Carbon Particles by a Spray Pyrolysis Process Using Poly(methyl methacrylate). *Industrial & Engineering Chemistry Research*, 57:11335–11341, 8 2018.

[43] Asep Bayu Dani Nandiyanto, Takashi Ogi, Wei-Ning Wang, Leon Gradon, and Kikuo Okuyama. Template-assisted spray-drying method for the fabrication of porous particles with tunable structures. *Advanced Powder Technology*, 30:2908–2924, 12 2019.

[44] Asep Suhendi, Asep Bayu Dani Nandiyanto, Muhammad Miftahul Munir, Takashi Ogi, Leon Gradon, and Kikuo Okuyama. Self-Assembly of Colloidal Nanoparticles Inside Charged Droplets during Spray-Drying in the Fabrication of Nanostructured Particles. *Langmuir*, 29:13152–13161, 10 2013.

[45] Annie M. Rahmatika, Youhei Toyoda, Tue T. Nguyen, Yohsuke Goi, Takeo Kitamura, Yuko Morita, Kazunori Kume, and Takashi Ogi. Cellulose Nanofiber and Magnetic Nanoparticles as Building Blocks Constructing Biomass-Based Porous Structured Particles and Their Protein Adsorption Performance. *ACS Sustainable Chemistry & Engineering*, 8:18686–18695, 12 2020.

[46] Takashi Ogi, Asep Bayu Dani Nandiyanto, and Kikuo Okuyama. Nanostructuring strategies in functional fine-particle synthesis towards resource and energy saving applications. *Advanced Powder Technology*, 25:3–17, 1 2014.

[47] Phong Hoai Le, Yasuhiko Kitamoto, Shunki Yamashita, Kiet Le Anh Cao, Tomoyuki Hirano, Tareq W. M. Amen, Nao Tsunoji, and Takashi Ogi. Macropore-Size Engineering toward Enhancing the Catalytic Performance of CO Oxidation over Three-Way Catalyst Particles. *ACS Applied Materials & Interfaces*, 15:54073–54084, 11 2023.

[48] Chang Liu, Jiajing Yu, Junyang You, Zhihua Wang, Meiling Zhang, Lei Shi, and Xupin Zhuang. Cellulose/Chitosan Composite Sponge for Efficient Protein Adsorption. *Industrial and Engineering Chemistry Research*, 60:9159–9166, 6 2021.

[49] Liangzhi Qiao, Qincong Li, Jiao Xie, and Kaifeng Du. Multi-size optimization of macroporous cellulose beads as protein anion exchangers: Effects of macropore size, protein size, and ligand length. *Journal of Chromatography A*, 1702:464068, 2023.

[50] Zhang Peian, Jia Haifeng, Gong Peijie, Ehsan Sadeghnezhad, Pang Qianqian, Dong Tianyu, Li Teng, Jin Huanchun, and Fang Jinggui. Chitosan induces jasmonic acid production leading to resistance of ripened fruit against Botrytis cinerea infection. *Food Chemistry*, 337:127772, 2 2021.

[51] Karlmarx G K Periyasamy, Hui Zuo, and Siyuan He. Flexible printed circuit board magnetic micromirror for laser marking/engraving. *Journal of Micromechanics and Microengineering*, 29:085001, 8 2019.

[52] Thomas G. Barclay, Candace Minhthu Day, Nikolai Petrovsky, and Sanjay Garg. Review of polysaccharide particle-based functional drug delivery. *Carbohydrate Polymers*, 221:94–112, 10 2019.

[53] Ankur Vaidya, Shweta Jain, Ram K. Agrawal, and Sanjay K. Jain. Pectin–metronidazole prodrug bearing microspheres for colon targeting. *Journal of Saudi Chemical Society*, 19:257–264, 5 2015.

[54] Hyun-Jong Cho, Dahlkyun Oh, and Dae-Duk Kim. Polysaccharides-based spray-dried microspheres for maintained stability and controlled release of protein. *Journal of Pharmaceutical Investigation*, 42:83–88, 4 2012.

[55] Zonghua Liu, Yanpeng Jiao, Yifei Wang, Changren Zhou, and Ziyong Zhang. Polysaccharides-based nanoparticles as drug delivery systems. *Advanced Drug Delivery Reviews*, 60:1650–1662, 12 2008.

[56] Tianxin Miao, Junqing Wang, Yun Zeng, Gang Liu, and Xiaoyuan Chen. Polysaccharide-Based Controlled Release Systems for Therapeutics Delivery and Tissue Engineering: From Bench to Bedside. *Advanced Science*, 5:1700513, 4 2018.

[57] Ana P. Almeida, Soraya Rodríguez-Rojo, Ana Teresa Serra, Helder Vila-Real, Ana Luisa Simplicio, Ivone Delgadilho, Sara Beirão da Costa, Luisa Beirão da Costa, Isabel D. Nogueira, and Catarina M.M. Duarte. Microencapsulation of oregano essential oil in starch-based materials using supercritical fluid technology. *Innovative Food Science & Emerging Technologies*, 20:140–145, 10 2013.

[58] Ke Luo, Hazzel Joy Adra, and Young-Rok Kim. Preparation of starch-based drug delivery system through the self-assembly of short chain glucans and control of its release property. *Carbohydrate Polymers*, 243:116385, 9 2020.

[59] Mehwish Abid, Muhammad Naveed, Iqra Azeem, Amir Faisal, Muhammad Faizan Nazar, and Basit Yameen. Colon specific enzyme responsive oligoester crosslinked dextran nanoparticles for controlled release of 5-fluorouracil. *International Journal of Pharmaceutics*, 586:119605, 2020.

[60] Amanda K. Peterson, David Gene Morgan, and Sara E. Skrabalak. Aerosol Synthesis of Porous Particles Using Simple Salts as a Pore Template. *Langmuir*, 26:8804–8809, 6 2010.

[61] Praveen Sher, Ganesh Ingavle amd Surendra Ponrathnam, and Atmaram P. Pawar. Low density porous carrier: Drug adsorption and release study by re-

sponse surface methodology using different solvents. *International Journal of Pharmaceutics*, 331:72–83, 2 2007.

[62] Won Hyuk Suh, Ah Ram Jang, Yoo-Hun Suh, and Kenneth S. Suslick. Porous, Hollow, and Ball-in-Ball Metal Oxide Microspheres: Preparation, Endocytosis, and Cytotoxicity. *Advanced Materials*, 18:1832–1837, 7 2006.

[63] Xiao-Yu Yang, Li-Hua Chen, Yu Li, Joanna Claire Rooke, Clément Sanchez, and Bao-Lian Su. Hierarchically porous materials: synthesis strategies and structure design. *Chemical Society Reviews*, 46:481–558, 2017.

[64] Victor Malgras, Joel Henzie, Toshiaki Takei, and Yusuke Yamauchi. Stable Blue Luminescent $CsPbBr_3$ Perovskite Nanocrystals Confined in Mesoporous Thin Films. *Angewandte Chemie International Edition*, 57:8881–8885, 7 2018.

[65] Bo Jiang, Yanna Guo, Jeonghun Kim, Andrew E. Whitten, Kathleen Wood, Kenya Kani, Alan E. Rowan, Joel Henzie, and Yusuke Yamauchi. Mesoporous Metallic Iridium Nanosheets. *Journal of the American Chemical Society*, 140:12434–12441, 10 2018.

[66] G. Collins, M. Blömker, M. Osiak, J. D. Holmes, M. Bredol, and C. O'Dwyer. Three-Dimensionally Ordered Hierarchically Porous Tin Dioxide Inverse Opals and Immobilization of Palladium Nanoparticles for Catalytic Applications. *Chemistry of Materials*, 25:4312–4320, 11 2013.

[67] Meiling Chen, Rui Xiong, Xin Cui, Qi Wang, and Xiaowang Liu. SiO_2-Encompassed Co@N-Doped Porous Carbon Assemblies as Recyclable Catalysts for Efficient Hydrolysis of Ammonia Borane. *Langmuir*, 35:671–677, 1 2019.

[68] Shan Liu, Zhu-Yin Sui, Tian-Xiong Wang, Hang-Yu Zhou, Yu-Wen Liu, and Bao-Hang Han. Tuning Both Surface Chemistry and Porous Properties of Polymer-Derived Porous Carbons for High-Performance Gas Adsorption. *Langmuir*, 35:7650–7658, 6 2019.

[69] Jing Wei, Dandan Zhou, Zhenkun Sun, Yonghui Deng, Yongyao Xia, and Dongyuan Zhao. A Controllable Synthesis of Rich Nitrogen-Doped Ordered Mesoporous Carbon for CO_2 Capture and Supercapacitors. *Advanced Functional Materials*, 23:2322–2328, 5 2013.

[70] Tian-Yi Ma, Hui Li, An-Na Tang, and Zhong-Yong Yuan. Ordered, Mesoporous Metal Phosphonate Materials with Microporous Crystalline Walls for Selective Separation Techniques. *Small*, 7:1827–1837, 7 2011.

[71] Junko Konishi, Koji Fujita, Satoshi Oiwa, Kazuki Nakanishi, and Kazuyuki Hirao. Crystalline ZrO_2 Monoliths with Well-Defined Macropores and Mesostructured Skeletons Prepared by Combining the Alkoxy-Derived Sol–Gel Process Accompanied by Phase Separation and the Solvothermal Process. *Chemistry of Materials*, 20:2165–2173, 3 2008.

[72] Qiang Zhao, Mingjie Yin, A. Ping Zhang, Simon Prescher, Markus Antonietti, and Jiayin Yuan. Hierarchically Structured Nanoporous Poly(Ionic Liquid) Membranes: Facile Preparation and Application in Fiber-Optic pH Sensing. *Journal of the American Chemical Society*, 135:5549–5552, 4 2013.

[73] Jun Kuang, Luqi Liu, Yun Gao, Ding Zhou, Zhuo Chen, Baohang Han, and Zhong Zhang. A hierarchically structured graphene foam and its potential as a large-scale strain-gauge sensor. *Nanoscale*, 5:12171, 2013.

[74] Wei Hu, Feifei Xie, Yuquan Li, Zhengchen Wu, Ke Tian, Miao Wang, Likun Pan, and Lei Li. Hierarchically Porous Carbon Derived from PolyHIPE for Supercapacitor and Deionization Applications. *Langmuir*, 33:13364–13375, 11 2017.

[75] Ruili Liu, Li Wan, Shaoqing Liu, Lixia Pan, Dongqing Wu, and Dongyuan Zhao. An Interface-Induced Co-Assembly Approach Towards Ordered Mesoporous Carbon/Graphene Aerogel for High-Performance Supercapacitors. *Advanced Functional Materials*, 25:526–533, 1 2015.

[76] Wen He, Dandan Min, Xudong Zhang, Yang Zhang, Zhiying Bi, and Yuanzheng Yue. Hierarchically Nanoporous Bioactive Glasses for High Efficiency Immobilization of Enzymes. *Advanced Functional Materials*, 24:2206–2215, 4 2014.

[77] Jiafu Shi, Chen Yang, Shaohua Zhang, Xiaoli Wang, Zhongyi Jiang, Wenyan Zhang, Xiaokai Song, Qinghong Ai, and Chunyong Tian. Polydopamine Microcapsules with Different Wall Structures Prepared by a Template-Mediated Method for Enzyme Immobilization. *ACS Applied Materials & Interfaces*, 5:9991–9997, 10 2013.

[78] Jalal Poostforooshan, Sabrina Belbekhouche, Masoom Shaban, Vanessa Alphonse, Damien Habert, Noureddine Bousserrhine, José Courty, and Alfred P. Weber. Aerosol-Assisted Synthesis of Tailor-Made Hollow Mesoporous Silica Microspheres for Controlled Release of Antibacterial and Anticancer Agents. *ACS Applied Materials & Interfaces*, 12:6885–6898, 2 2020.

[79] Annie M. Rahmatika, Yohsuke Goi, Takeo Kitamura, Yuko Morita, Ferry Iskandar, and Takashi Ogi. Silica-supported carboxylated cellulose nanofibers for effective lysozyme adsorption: Effect of macropore size. *Advanced Powder Technology*, 31:2932–2941, 7 2020.

[80] Christopher M. A. Parlett, Karen Wilson, and Adam F. Lee. Hierarchical porous materials: catalytic applications. *Chem. Soc. Rev.*, 42:3876–3893, 2013.

[81] Asep Bayu Dani Nandiyanto, Osi Arutanti, Takashi Ogi, Ferry Iskandar, Tae Oh Kim, and Kikuo Okuyama. Synthesis of spherical macroporous WO_3 particles and their high photocatalytic performance. *Chemical Engineering Science*, 101:523–532, 9 2013.

[82] Yuechang Wei, Peng Zhang, Jing Xiong, Qi Yu, Qiangqiang Wu, Zhen Zhao, and Jian Liu. SO_2-Tolerant Catalytic Removal of Soot Particles over 3D Ordered Macroporous Al_2O_3-Supported Binary Pt–Co Oxide Catalysts. *Environmental Science & Technology*, 54:6947–6956, 6 2020.

[83] Yinying Tao, Ernie X. Perez Almodovar, Giorgio Carta, Gisela Ferreira, and David Robbins. Adsorption kinetics of deamidated antibody variants on macroporous and dextran-grafted cation exchangers. III. Microscopic studies. *Journal of Chromatography A*, 1218:8027–8035, 11 2011.

[84] Ratna Balgis, Takashi Ogi, Wei-Ning Wang, Gopinathan M. Anilkumar, Sumihito Sago, and Kikuo Okuyama. Aerosol Synthesis of Self-Organized Nanostructured Hollow and Porous Carbon Particles Using a Dual Polymer System. *Langmuir*, 30:11257–11262, 9 2014.

[85] Hamidreza Arandiyan, Yuan Wang, Jason Scott, Sara Mesgari, Hongxing Dai, and Rose Amal. In Situ Exsolution of Bimetallic Rh–Ni Nanoalloys: a Highly Efficient Catalyst for CO_2 Methanation. *ACS Applied Materials & Interfaces*, 10:16352–16357, 5 2018.

[86] Mikrajuddin Abdullah, Ferry Iskandar, Shinji Shibamoto, Takashi Ogi, and Kikuo Okuyama. Preparation of oxide particles with ordered macropores by colloidal templating and spray pyrolysis. *Acta Materialia*, 52:5151–5156, 10 2004.

[87] Kui Shen, Lei Zhang, Xiaodong Chen, Lingmei Liu, Daliang Zhang, Yu Han, Junying Chen, Jilan Long, Rafael Luque, Yingwei Li, and Banglin Chen. Ordered macro-microporous metal-organic framework single crystals. *Science*, 359:206–210, 1 2018.

[88] Hao Wang, Zihao Qin, Yi Liu, Xiaoting Li, Jianfei Liu, Yongfeng Liu, Dongdong Huang, and Duolong Di. Design and preparation of porous polymer particles with polydopamine coating and selective enrichment for biomolecules. *RSC Advances*, 7:45311–45319, 2017.

[89] Peter Johnson and John Gareth Lloyd-Jones. *Drug Delivery Systems: Fundamentals and Techniques*. VCH, 1987.

[90] Peter J. Tarcha. *Polymers for Controlled Drug Delivery*. CRC Press, 1990.

[91] Ankur vaidya, Aviral Jain, Piush Khare, Ram K. Agrawal, and Sanjay K. Jain. Metronidazole loaded pectin microspheres for colon targeting. *Journal of Pharmaceutical Sciences*, 98:4229–4236, 11 2009.

[92] T.W Wong, H.Y Lee, L.W Chan, and P.W.S Heng. Drug release properties of pectinate microspheres prepared by emulsification method. *International Journal of Pharmaceutics*, 242:233–237, 8 2002.

[93] Federica Bigucci, Barbara Luppi, Libera Monaco, Teresa Cerchiara, and Vittorio Zecchi. Pectin-based microspheres for colon-specific delivery of vancomycin. *Journal of Pharmacy and Pharmacology*, 61:41–46, 2008.

[94] Chang-Moon Lee, Dong-Woon Kim, Hyun-Chul Lee, and Ki-Young Lee. Pectin microspheres for oral colon delivery: Preparation using spray drying method andin vitro release of indomethacin. *Biotechnology and Bioprocess Engineering*, 9:191–195, 6 2004.

[95] Kiet Le Anh Cao, Shuto Taniguchi, Tue Tri Nguyen, Aditya F. Arif, Ferry Iskandar, and Takashi Ogi. Precisely tailored synthesis of hexagonal hollow silica plate particles and their polymer nanocomposite films with low refractive index. *Journal of Colloid and Interface Science*, 571:378–386, 7 2020.

[96] Masayoshi Fuji, Takahiro Shin, Hideo Watanabe, and Takashi Takei. Shape-controlled hollow silica nanoparticles synthesized by an inorganic particle template method. *Advanced Powder Technology*, 23:562–565, 9 2012.

[97] Juan Diego Rodriguez-Blanco, Samuel Shaw, and Liane G. Benning. The kinetics and mechanisms of amorphous calcium carbonate (ACC) crystallization to calcite, viavaterite. *Nanoscale*, 3:265–271, 2011.

[98] Nidhi Joshi, Kamla Rawat, and H. B. Bohidar. Influence of Structure, Charge, and Concentration on the Pectin–Calcium–Surfactant Complexes. *The Journal of Physical Chemistry B*, 120:4249–4257, 5 2016.

[99] Ilse Fraeye, Thomas Duvetter, Eugénie Doungla, Ann Van Loey, and Marc Hendrickx. Fine-tuning the properties of pectin–calcium gels by control of pectin fine structure, gel composition and environmental conditions. *Trends in Food Science & Technology*, 21:219–228, 5 2010.

[100] Kiet Le Anh Cao, Aditya F. Arif, Kazuki Kamikubo, Takafumi Izawa, Hideharu Iwasaki, and Takashi Ogi. Controllable Synthesis of Carbon-Coated SiO_x Particles through a Simultaneous Reaction between the Hydrolysis–Condensation of Tetramethyl Orthosilicate and the Polymerization of 3-Aminophenol. *Langmuir*, 35:13681–13692, 10 2019.

[101] Matthias Thommes, Katsumi Kaneko, Alexander V. Neimark, James P. Olivier, Francisco Rodriguez-Reinoso, Jean Rouquerol, and Kenneth S.W. Sing. Physisorption of gases, with special reference to the evaluation of surface area and pore size distribution (IUPAC Technical Report). *Pure and Applied Chemistry*, 87:1051–1069, 10 2015.

[102] Utpalendu Kuila and Manika Prasad. Specific surface area and pore-size distribution in clays and shales. *Geophysical Prospecting*, 61:341–362, 3 2013.

[103] Asep Bayu Dani Nandiyanto, Asep Suhendi, Osi Arutanti, Takashi Ogi, and Kikuo Okuyama. Influences of Surface Charge, Size, and Concentration of Colloidal Nanoparticles on Fabrication of Self-Organized Porous Silica in Film and Particle Forms. *Langmuir*, 29:6262–6270, 5 2013.

[104] Asep Bayu Dani Nandiyanto, Asep Suhendi, Takashi Ogi, Ryohei Umemoto, and Kikuo Okuyama. Size- and charge-controllable polystyrene spheres for templates in the preparation of porous silica particles with tunable internal hole configurations. *Chemical Engineering Journal*, 256:421–430, 11 2014.

[105] Ferry Iskandar, Asep Bayu Dani Nandiyanto, W. Widiyastuti, Lee Sin Young, Kikuo Okuyama, and Leon Gradon. Production of morphology-controllable

porous hyaluronic acid particles using a spray-drying method. *Acta Biomaterialia*, 5:1027–1034, 5 2009.

[106] Kiet Le Anh Cao, Annie Mufyda Rahmatika, Yasuhiko Kitamoto, Mai Thanh Thi Nguyen, and Takashi Ogi. Controllable synthesis of spherical carbon particles transition from dense to hollow structure derived from Kraft lignin. *Journal of Colloid and Interface Science*, 589:252–263, 5 2021.

[107] Arthur H. Lefebvre and Vincent G. McDonell. *Atomization and Sprays*. CRC Press, 2017.

[108] Ferry Iskandar, Leon Gradon, and Kikuo Okuyama. Control of the morphology of nanostructured particles prepared by the spray drying of a nanoparticle sol. *Journal of Colloid and Interface Science*, 265:296–303, 9 2003.

[109] Ferry Iskandar, Soon-Gil Kim, Asep Bayu Dani Nandiyanto, Yutaka Kaihatsu, Takashi Ogi, and Kikuo Okuyama. Direct synthesis of hBN / MWCNT composite particles using spray pyrolysis. *Journal of Alloys and Compounds*, 471:166–171, 3 2009.

[110] Caitlin Smith. Striving for purity: Advances in protein purification. *Nature Methods*, 2:71–77, 2005.

[111] Gary Walsh. Biopharmaceutical benchmarks 2018. *Nature Biotechnology*, 36:1136–1145, 2018.

[112] J. Christopher Love, Kerry Routenberg Love, and Paul W. Barone. Enabling global access to high-quality biopharmaceuticals. *Current Opinion in Chemical Engineering*, 2:383–390, 2013.

[113] Jérémie Huynh, Ruben Palacio, Fariba Safizadeh, Grégory Lefèvre, Michael Descostes, Lilian Eloy, Nadia Guignard, Julie Rousseau, Sébastien Royer, Emmanuel Tertre, and Isabelle Batonneau-Gener. Adsorption of Uranium over NH_2-Functionalized Ordered Silica in Aqueous Solutions. *ACS Applied Materials & Interfaces*, 9:15672–15684, 5 2017.

[114] B. Xiao and K. M. Thomas. Competitive Adsorption of Aqueous Metal Ions on an Oxidized Nanoporous Activated Carbon. *Langmuir*, 20:4566–4578, 5 2004.

[115] Zhiguo Zhu, Hao Xu, Jingang Jiang, Haihong Wu, and Peng Wu. Hydrophobic Nanosized All-Silica Beta Zeolite: Efficient Synthesis and Adsorption Application. *ACS Applied Materials & Interfaces*, 9:27273–27283, 8 2017.

[116] Sarah Hudson, Jakki Cooney, and Edmond Magner. Proteins in Mesoporous Silicates. *Angewandte Chemie International Edition*, 47:8582–8594, 10 2008.

[117] Amit Katiyar, Santosh Yadav, Panagiotis G Smirniotis, and Neville G Pinto. Synthesis of ordered large pore SBA-15 spherical particles for adsorption of biomolecules. *Journal of Chromatography A*, 1122:13–20, 2006.

[118] Rongyue Zhang, Qiang Li, Yang Gao, Juan Li, Yongdong Huang, Cui Song, Weiqing Zhou, Guanghui Ma, and Zhiguo Su. Hydrophilic modification gigaporous resins with poly(ethylenimine) for high-throughput proteins ion-exchange chromatography. *Journal of Chromatography A*, 1343:109–118, 2014.

[119] Qiuxia Fu, Yang Si, Cheng Duan, Zishuo Yan, Lifang Liu, Jianyong Yu, and Bin Ding. Highly Carboxylated, Cellular Structured, and Underwater Superelastic Nanofibrous Aerogels for Efficient Protein Separation. *Advanced Functional Materials*, 29:1808234, 3 2019.

[120] Liangzhi Qiao, Su Su Lei, and Kaifeng Du. High-surface-area interconnected macroporous nanofibrous cellulose microspheres: a versatile platform for large capacity and high-throughput protein separation. *Cellulose*, 28:2125–2136, 2021.

[121] Liangshen Zhao, Shasha Li, Wenhui Wang, Yinghong Wang, and Kaifeng Du. Preparation and characterization of highly porous cellulose-agarose composite chromatographic microspheres for enhanced selective separation of histidine-rich proteins. *Journal of Chromatography A*, 1637:461831, 2021.

[122] Weixia Xu, Pengjin Ge, Boning Niu, Xiaokun Zhang, Jie Liu, and Jingjing Xie. Macroporous silica nanoparticles for delivering Bcl2-function converting peptide

to treat multidrug resistant-cancer cells. *Journal of Colloid and Interface Science*, 527:141–150, 2018.

[123] Ok-Hee Kim, Yong-Hun Cho, Soon Hyung Kang, Hee-Young Park, Minhyoung Kim, Ju Wan Lim, Dong Young Chung, Myeong Jae Lee, Heeman Choe, and Yung-Eun Sung. Ordered macroporous platinum electrode and enhanced mass transfer in fuel cells using inverse opal structure. *Nature Communications*, 4:2473, 2013.

[124] Baizeng Fang, Jung Ho Kim, Min-Sik Kim, and Jong-Sung Yu. Hierarchical Nanostructured Carbons with Meso–Macroporosity: Design, Characterization, and Applications. *Accounts of Chemical Research*, 46:1397–1406, 7 2013.

[125] Zichao Li, Huarong Liu, Lai Zeng, Hewen Liu, Song Yang, and Yanmei Wang. Preparation of High Internal Water-Phase Double Emulsions Stabilized by a Single Anionic Surfactant for Fabricating Interconnecting Porous Polymer Microspheres. *Langmuir*, 30:12154–12163, 10 2014.

[126] Xiang-Ming Na, Fei Gao, Li-Ye Zhang, Zhi-Guo Su, and Guang-Hui Ma. Biodegradable Microcapsules Prepared by Self-Healing of Porous Microspheres. *ACS Macro Letters*, 1:697–700, 6 2012.

[127] Yifan Li, Shensheng Chen, Serkan Demirci, Shiyi Qin, Zihao Xu, Emily Olson, Fei Liu, Devin Palm, Xin Yong, and Shan Jiang. Morphology evolution of Janus dumbbell nanoparticles in seeded emulsion polymerization. *Journal of Colloid and Interface Science*, 543:34–42, 2019.

[128] Qiong Tian, Xiaojing Yu, Lifeng Zhang, and Demei Yu. Monodisperse raspberry-like multihollow polymer/Ag nanocomposite microspheres for rapid catalytic degradation of methylene blue. *Journal of Colloid and Interface Science*, 491:294–304, 2017.

[129] Chao Huang, Yu Cheng, Zewen Gao, Hanbing Zhang, and Jie Wei. Portable label-free inverse opal photonic hydrogel particles serve as facile pesticides colorimetric monitoring. *Sensors and Actuators B: Chemical*, 273:1705–1712, 2018.

[130] Jeong-Hui Park, Cheol-Min Han, Eun-Jung Lee, and Hae-Won Kim. Preparation of highly monodispersed porous-channeled poly(caprolactone) microspheres by a microfluidic system. *Materials Letters*, 181:92–98, 2016.

[131] Ranjith Kumar Kankala, Jia Zhao, Chen-Guang Liu, Xiao-Jie Song, Da-Yun Yang, Kai Zhu, Shi-Bin Wang, Yu Shrike Zhang, and Ai-Zheng Chen. Highly Porous Microcarriers for Minimally Invasive *In Situ* Skeletal Muscle Cell Delivery. *Small*, 15:1901397, 6 2019.

[132] Ileana-Alexandra Pavel, Sofia F Prazeres, Gemma Montalvo, Carmen García Ruiz, Vincent Nicolas, Alain Celzard, François Dehez, Laetitia Canabady-Rochelle, Nadia Canilho, and Andreea Pasc. Effect of Meso vs Macro Size of Hierarchical Porous Silica on the Adsorption and Activity of Immobilized β-Galactosidase. *Langmuir*, 33:3333–3340, 4 2017.

[133] Zhenkun Sun, Yonghui Deng, Jing Wei, Dong Gu, Bo Tu, and Dongyuan Zhao. Hierarchically Ordered Macro-/Mesoporous Silica Monolith: Tuning Macropore Entrance Size for Size-Selective Adsorption of Proteins. *Chemistry of Materials*, 23:2176–2184, 4 2011.

[134] Ratna Balgis, W. Widiyastuti, Takashi Ogi, and Kikuo Okuyama. Enhanced Electrocatalytic Activity of Pt/3D Hierarchical Bimodal Macroporous Carbon Nanospheres. *ACS Applied Materials & Interfaces*, 9:23792–23799, 7 2017.

[135] Kiet Le Anh Cao, Annie Mufyda Rahmatika, Yasuhiko Kitamoto, Mai Thanh Thi Nguyen, and Takashi Ogi. Controllable synthesis of spherical carbon particles transition from dense to hollow structure derived from Kraft lignin. *Journal of Colloid and Interface Science*, 589:252–263, 2021.

[136] Chaochao Cao, Jingwen Yang, Kun Fu, Qinghong Zhai, Zheng Zhou, Jiawei Ji, Yuanhui Ma, Min Zhou, Yanming Xue, and Chengchun Tang. Hierarchically porous boron nitride foams for multifunctional bulk adsorbents. *Chemical Engineering Journal*, 422:129896, 2021.

[137] Tue Tri Nguyen, Annie M. Rahmatika, Masato Miyauchi, Kiet Le Anh Cao, and Takashi Ogi. Synthesis of High Specific Surface Area Macroporous Pectin Particles by Template-Assisted Spray Drying. *Langmuir*, 37:4256–4266, 4 2021.

[138] Isabelle Braccini and Serge Pérez. Molecular basis of Ca^{2+}-induced gelation in alginates and pectins: The egg-box model revisited. *Biomacromolecules*, 2:1089–1096, 12 2001.

[139] Irit Ventura, Joanna Jammal, and Havazelet Bianco-Peled. Insights into the nanostructure of low-methoxyl pectin-calcium gels. *Carbohydrate Polymers*, 97:650–658, 2013.

[140] Xiaoxi Qi, Senay Simsek, Bingcan Chen, and Jiajia Rao. Alginate-based double-network hydrogel improves the viability of encapsulated probiotics during simulated sequential gastrointestinal digestion: Effect of biopolymer type and concentrations. *International Journal of Biological Macromolecules*, 165:1675–1685, 2020.

[141] Jing Zhang, Satoshi Ohara, Mitsuo Umetsu, Takashi Naka, Yoshiharu Hatakeyama, and Tadafumi Adschiri. Colloidal Ceria Nanocrystals: A Tailor-Made Crystal Morphology in Supercritical Water. *Advanced Materials*, 19:203–206, 1 2007.

[142] Christophe Jung, Johanna Kirstein, Barbara Platschek, Thomas Bein, Michael Budde, Irmgard Frank, Klaus Müllen, Jens Michaelis, and Christoph Bräuchle. Diffusion of Oriented Single Molecules with Switchable Mobility in Networks of Long Unidimensional Nanochannels. *Journal of the American Chemical Society*, 130:1638–1648, 2 2008.

[143] Zili Ma, Matthias Klimpel, Serhiy Budnyk, Anna Rokicińska, Piotr Kuśtrowski, Richard Dronskowski, Aji P Mathew, Tetyana Budnyak, and Adam Slabon. Combining Electrocatalysts and Biobased Adsorbents for Sustainable Denitrification. *ACS Sustainable Chemistry & Engineering*, 9:3658–3667, 3 2021.

[144] Kairuo Xu, Myriam M Ouberai, and Mark E Welland. A comprehensive study of lysozyme adsorption using dual polarization interferometry and quartz crystal microbalance with dissipation. *Biomaterials*, 34:1461–1470, 2013.

[145] Myriam M Ouberai, Kairuo Xu, and Mark E Welland. Effect of the interplay between protein and surface on the properties of adsorbed protein layers. *Biomaterials*, 35:6157–6163, 2014.

[146] Mohammadmahdi Rabieizadeh, Seyed Mohammadreza Kashefimofrad, and Fereshteh Naeimpoor. Monolithic molecularly imprinted cryogel for lysozyme recognition. *Journal of Separation Science*, 37:2983–2990, 10 2014.

[147] Gulay Bayramoglu, V Cengiz Ozalp, Meltem Yilmaz, Ulku Guler, Bekir Salih, and M Yakup Arica. Lysozyme specific aptamer immobilized MCM-41 silicate for single-step purification and quartz crystal microbalance (QCM)-based determination of lysozyme from chicken egg white. *Microporous and Mesoporous Materials*, 207:95–104, 2015.

[148] Guoqing Zhang, Qing Cao, Na Li, Kean Li, and Feng Liu. Tris(hydroxymethyl)aminomethane-modified magnetic microspheres for rapid affinity purification of lysozyme. *Talanta*, 83:1515–1520, 2011.

[149] Federico J Wolman, Guillermo J Copello, Andrea M Mebert, Alexandra M Targovnik, María V Miranda, Agustín A Navarro del Cañizo, Luis E Díaz, and Osvaldo Cascone. Egg white lysozyme purification with a chitin–silica-based affinity chromatographic matrix. *European Food Research and Technology*, 231:181–188, 2010.

[150] Dandan Shao, Keke Xu, Xiaojie Song, Jianhua Hu, Wuli Yang, and Changchun Wang. Effective adsorption and separation of lysozyme with PAA-modified Fe_3O_4@silica core/shell microspheres. *Journal of Colloid and Interface Science*, 336:526–532, 2009.

[151] Tina Chakrabarty, Mahendra Kumar, and Vinod K Shahi. pH Responsive Hybrid Zwitterionomer for Protein Separation: Smart Nanostructured Adsorbent. *Industrial & Engineering Chemistry Research*, 51:3015–3022, 2 2012.

[152] Thayyath S. Anirudhan and Priya Senan. Adsorptive potential of sulfonated poly(glycidylmethacrylate)-grafted cellulose for separation of lysozyme from aqueous phase: Mass transfer analysis, kinetic and equilibrium profiles. *Colloids and Surfaces A: Physicochemical and Engineering Aspects*, 377:156–166, 2011.

[153] Zhonghong Li, Miao Cao, Wengang Zhang, Lizhi Liu, Jianlong Wang, Wupeng Ge, Yahong Yuan, Tianli Yue, Ronghua Li, and William W Yu. Affinity adsorption of lysozyme with Reactive Red 120 modified magnetic chitosan microspheres. *Food Chemistry*, 145:749–755, 2014.

[154] Yasuhiko Kitamoto, Kiet Le Anh Cao, Phong Hoai Le, Oktaviardi Bityasmawan Abdillah, Ferry Iskandar, and Takashi Ogi. A Sustainable Approach for Preparing Porous Carbon Spheres Derived from Kraft Lignin and Sodium Hydroxide as Highly Packed Thin Film Electrode Materials. *Langmuir*, 38:3540–3552, 3 2022.

[155] Kiet Le Anh Cao, Ferry Iskandar, Eishi Tanabe, and Takashi Ogi. Recent advances in the fabrication and functionalization of nanostructured carbon spheres for energy storage applications. *KONA Powder and Particle Journal*, 40:197–218, 2023.

[156] Morteza Saffari, Amirali Ebrahimi, and Timothy Langrish. A novel formulation for solubility and content uniformity enhancement of poorly water-soluble drugs using highly-porous mannitol. *European Journal of Pharmaceutical Sciences*, 83:52–61, 2016.

[157] Qingxia Lin, Wei Li, Di Liu, Mengyuan Zhao, Xuerui Zhu, Weiwei Li, Longfeng Wang, Tiesong Zheng, and Jianlin Li. Porous Silicon Carrier Delivery System for Curcumin: Preparation, Characterization, and Cytotoxicity in Vitro. *ACS Applied Bio Materials*, 2:1041–1049, 3 2019.

[158] Marzieh Heidari Nia, Roya Koshani, Jose G. Munguia-Lopez, Ali Reza Kiasat, Joseph M. Kinsella, and Theo G.M. Van De Ven. Biotemplated Hollow Mesoporous Silica Particles as Efficient Carriers for Drug Delivery. *ACS Applied Bio Materials*, 4:4201–4214, 5 2021.

[159] Xiaojia Liu, Xi Pan, Mingze Sun, Dandan Xu, Xiuzhen Tang, Xiaohui Yan, Dekai Zhou, and Xing Ma. Importance of Robust and Reliable Nanochannel Sealing for Enhancing Drug Delivery Efficacy of Hollow Mesoporous Nanocontainer. *ACS Applied Bio Materials*, 3:1434–1443, 3 2020.

[160] M. Jelvehgari, M. R. Siahi-Shadbad, S. Azarmi, Gary P. Martin, and Ali Nokhodchi. The microsponge delivery system of benzoyl peroxide: Preparation, characterization and release studies. *International Journal of Pharmaceutics*, 308:124–132, 2006.

[161] Tue Tri Nguyen, Masato Miyauchi, Annie M. Rahmatika, Kiet Le Anh Cao, Eishi Tanabe, and Takashi Ogi. Enhanced Protein Adsorption Capacity of Macroporous Pectin Particles with High Specific Surface Area and an Interconnected Pore Network. *ACS Applied Materials and Interfaces*, 14:14435–14446, 3 2022.

[162] Annie M. Rahmatika, Youhei Toyoda, Tue Tri Nguyen, Kiet Le Anh Cao, Tomoyuki Hirano, Takeo Kitamura, Yohsuke Goi, Yuko Morita, and Takashi Ogi. Effects of Solvent Polarity on Nanostructure Formation of Spray-Dried TEMPO-Oxidized Cellulose Nanofiber Particles. *ACS Applied Polymer Materials*, 4:6700–6709, 9 2022.

[163] Tue Tri Nguyen, Youhei Toyoda, Nur Syakirah Nabilah Saipul Bahri, Annie M. Rahmatika, Kiet Le Anh Cao, Tomoyuki Hirano, Katsuo Takahashi, Yohsuke Goi,

Yuko Morita, Mai Watanabe, and Takashi Ogi. Tuning of water resistance and protein adsorption capacity of porous cellulose nanofiber particles prepared by spray drying with cross-linking reaction. *Journal of Colloid and Interface Science*, 630:134–143, 1 2023.

[164] Phong Hoai Le, Yasuhiko Kitamoto, Kiet Le Anh Cao, Tomoyuki Hirano, Eishi Tanabe, and Takashi Ogi. Synthesis of macroporous three-way catalysts via template-assisted spray process for enhancing mass transfer in gas adsorption. *Advanced Powder Technology*, 33:103581, 2022.

[165] Kalpesh Vaghasiya, Eupa Ray, Ankur Sharma, Om Prakash Katare, and Rahul Kumar Verma. Matrix Metalloproteinase-Responsive Mesoporous Silica Nanoparticles Cloaked with Cleavable Protein for ”self-Actuating” On-Demand Controlled Drug Delivery for Cancer Therapy. *ACS Applied Bio Materials*, 3:4987–4999, 8 2020.

[166] Yu Jin Oh, Jangwook Lee, Ji Young Seo, Taiyoun Rhim, Sang Heon Kim, Ho Joo Yoon, and Kuen Yong Lee. Preparation of budesonide-loaded porous PLGA microparticles and their therapeutic efficacy in a murine asthma model. *Journal of Controlled Release*, 150:56–62, 2011.

[167] Beibei Zhao, Jing Du, Yayuan Zhang, Zhengbiao Gu, Zhaofeng Li, Li Cheng, Caiming Li, and Yan Hong. Polysaccharide-coated porous starch-based oral carrier for paclitaxel: Adsorption and sustained release in colon. *Carbohydrate Polymers*, 291:119571, 2022.

[168] Khorshid Kamguyan, Anders Meyer Torp, Juliane Fjelrad Christfort, Priscila R. Guerra, Tine Rask Licht, Line Hagner Nielsen, Kinga Zor, and Anja Boisen. Colon-Specific Delivery of Bioactive Agents Using Genipin-Cross-Linked Chitosan Coated Microcontainers. *ACS Applied Bio Materials*, 4:752–762, 1 2021.

[169] Nilesh Kulkarni, Priti Jain, Amol Shindikar, Pravin Suryawanshi, and Nanasaheb Thorat. Advances in the colon-targeted chitosan based multiunit drug delivery

systems for the treatment of inflammatory bowel disease. *Carbohydrate Polymers*, 288:119351, 2022.

[170] Niranjan G. Kotla, Rajbir Singh, Becca V. Baby, Swetha Rasala, Jawad Rasool, Sean O. Hynes, Darrell Martin, Laurence J. Egan, Praveen K. Vemula, Venkatakrishna R. Jala, Yury Rochev, and Abhay Pandit. Inflammation-specific targeted carriers for local drug delivery to inflammatory bowel disease. *Biomaterials*, 281:121364, 2022.

[171] Hicheme Hadji and Kawthar Bouchemal. Advances in the treatment of inflammatory bowel disease: Focus on polysaccharide nanoparticulate drug delivery systems. *Advanced Drug Delivery Reviews*, 181:114101, 2022.

[172] Zahra Vaezi, Hamid Asadzadeh Aghdaei, Mosslim Sedghi, Reza Mahdavian, Maryam Molakarimi, Naimeh Hashemi, and Hossein Naderi-Manesh. Hemoglobin bio-adhesive nanoparticles as a colon-specific delivery system for sustained release of 5-aminosalicylic acid in the effective treatment of inflammatory bowel disease. *International Journal of Pharmaceutics*, 616:121531, 2022.

[173] Rosaria Ciriminna, Alexandra Fidalgo, Antonino Scurria, Laura M. Ilharco, and Mario Pagliaro. Pectin: New science and forthcoming applications of the most valued hydrocolloid. *Food Hydrocolloids*, 127:107483, 2022.

[174] Sophie Groult and Tatiana Budtova. Tuning structure and properties of pectin aerogels. *European Polymer Journal*, 108:250–261, 2018.

[175] Lin Shu Liu, Marshall L. Fishman, Joseph Kost, and Kevin B. Hicks. Pectin-based systems for colon-specific drug delivery via oral route. *Biomaterials*, 24:3333–3343, 2003.

[176] Ifra Mirza and Sampa Saha. Biocompatible Anisotropic Polymeric Particles: Synthesis, Characterization, and Biomedical Applications. *ACS Applied Bio Materials*, 3:8241–8270, 12 2020.

[177] Sophie Groult, Sytze Buwalda, and Tatiana Budtova. Pectin hydrogels, aerogels, cryogels and xerogels: Influence of drying on structural and release properties. *European Polymer Journal*, 149:110386, 2021.

[178] Sophie Groult, Sytze Buwalda, and Tatiana Budtova. Tuning bio-aerogel properties for controlling theophylline delivery. Part 1: Pectin aerogels. *Materials Science and Engineering C*, 126:112148, 2021.

[179] Gang Chun Zhang, Hong Liang Lin, and Shan Yang Lin. Thermal analysis and FTIR spectral curve-fitting investigation of formation mechanism and stability of indomethacin-saccharin cocrystals via solid-state grinding process. *Journal of Pharmaceutical and Biomedical Analysis*, 66:162–169, 2012.

[180] Suraj Koirala, Biplab Roy, Pritam Guha, Ravi Bhattarai, Manish Sapkota, Prasant Nahak, Gourab Karmakar, Amit Kumar Mandal, Anoop Kumar, and Amiya Kumar Panda. Effect of double tailed cationic surfactants on the physicochemical behavior of hybrid vesicles. *RSC Advances*, 6:13786–13796, 2016.

[181] Daniela Atanasova, Desislava Staneva, and Ivo Grabchev. Modified with chitosan cotton fabric for control release of indomethacin. *IOP Conference Series: Materials Science and Engineering*, 1188:012004, 2021.

[182] Behzad Soltani, Hafezeh Nabipour, and Navid Ahmadi Nasab. Fabrication, controlled release, and kinetic studies of indomethacin—layered zinc hydroxide nanohybrid and its effect on the viability of HFFF2. *Journal of Dispersion Science and Technology*, 39:1200–1207, 2018.

[183] Xiaoda Yuan, Tian Xiang Xiang, Bradley D. Anderson, and Eric J. Munson. Hydrogen Bonding Interactions in Amorphous Indomethacin and Its Amorphous Solid Dispersions with Poly(vinylpyrrolidone) and Poly(vinylpyrrolidone-co-vinyl acetate) Studied Using ^{13}C Solid-State NMR. *Molecular Pharmaceutics*, 12:4518–4528, 12 2015.

[184] Paula González Seligra, Carolina Medina Jaramillo, Lucía Famá, and Silvia Goyanes. Biodegradable and non-retrogradable eco-films based on starch-glycerol with citric acid as crosslinking agent. *Carbohydrate Polymers*, 138:66–74, 2016.

[185] Simon Bates, George Zografi, David Engers, Kenneth Morris, Kieran Crowley, and Ann Newman. Analysis of amorphous and nanocrystalline solids from their X-ray diffraction patterns. *Pharmaceutical Research*, 23:2333–2349, 2006.

[186] Tomaž Einfal, Odon Planinšek, and Klemen Hrovat. Methods of amorphization and investigation of the amorphous state. *Acta Pharmaceutica*, 63:305–334, 2013.

[187] Yuta Hatanaka, Hiromasa Uchiyama, Kazunori Kadota, and Yuichi Tozuka. Designing amorphous formulations of polyphenols with naringin by spray-drying for enhanced solubility and permeability. *Advanced Powder Technology*, 33:103627, 11 2022.

[188] Navneet Sharma, Parshotam Madan, and Senshang Lin. Effect of process and formulation variables on the preparation of parenteral paclitaxel-loaded biodegradable polymeric nanoparticles: A co-surfactant study. *Asian Journal of Pharmaceutical Sciences*, 11:404–416, 2016.

[189] Xiangrong Song, Yu Zhao, Shixiang Hou, Fangyuan Xu, Rongli Zhao, Junyao He, Zheng Cai, Yuanbo Li, and Qiuhong Chen. Dual agents loaded PLGA nanoparticles: Systematic study of particle size and drug entrapment efficiency. *European Journal of Pharmaceutics and Biopharmaceutics*, 69:445–453, 2008.

[190] Faraj Atassi and Stephen R. Byrn. General trends in the desolvation behavior of calcium salts. *Pharmaceutical Research*, 23:2405–2412, 2006.

[191] Abderrahim Bennis, Jean-Jacques Serrano, and Farid Bennis. Calcium salt of indomethacin pentahydrate and its preparation, 2004.

[192] Nalinkanth G. Veerabadran, Ronald R. Price, and Yuri M. Lvov. Clay Nanotubes for Encapsulation and Sustained Release of Drugs. *Nano*, 02:115–120, 4 2007.

[193] Ghanashyam Acharya, Crystal S. Shin, Kumar Vedantham, Matthew McDermott, Thomas Rish, Keith Hansen, Yourong Fu, and Kinam Park. A study of drug release from homogeneous PLGA microstructures. *Journal of Controlled Release*, 146:201–206, 2010.

[194] Shu ya Wang, Yu jie Meng, Jun Li, Jin peng Liu, Zun qi Liu, and De qiang Li. A novel and simple oral colon-specific drug delivery system based on the pectin/modified nano-carbon sphere nanocomposite gel films. *International Journal of Biological Macromolecules*, 157:170–176, 2020.

[195] Satoshi Nogami, Hiromasa Uchiyama, Kazunori Kadota, and Yuichi Tozuka. Design of a pH-responsive oral gel formulation based on the matrix systems of gelatin/hydroxypropyl methylcellulose phthalate for controlled drug release. *International Journal of Pharmaceutics*, 592:120047, 2021.

[196] Satoshi Nogami, Kazunori Kadota, Hiromasa Uchiyama, Hiroshi Arima-Osonoi, Mitsuhiro Shibayama, and Yuichi Tozuka. Evaluation of the rheological and rupture properties of gelatin-based hydrogels blended with polymers to determine their drug diffusion behavior. *Polymer Journal*, 54:1477–1487, 2022.

[197] Richard W. Korsmeyer, Robert Gurny, Eric Doelker, Pierre Buri, and Nikolaos A. Peppas. Mechanisms of solute release from porous hydrophilic polymers. *International Journal of Pharmaceutics*, 15:25–35, 1983.

[198] Himadri Sekhar Samanta and Samit Kumar Ray. Effect of pectin and attapulgite filler on swelling, network parameters and controlled release of diltiazem hydrochloride from polyacrylic copolymer gel. *International Journal of Biological Macromolecules*, 190:978–988, 2021.

[199] Péter Veres, Mónika Kéri, István Bányai, István Lázár, István Fábián, Concepción Domingo, and József Kalmár. Mechanism of drug release from silica-gelatin aerogel—Relationship between matrix structure and release kinetics. *Colloids and Surfaces B: Biointerfaces*, 152:229–237, 2017.

[200] Philip L. Ritger and Nikolaos A. Peppas. A simple equation for description of solute release II. Fickian and anomalous release from swellable devices. *Journal of Controlled Release*, 5:37–42, 1987.

[201] Chandrashekar Raman, Cory Berkland, Kyekyoon Kim, and Daniel W. Pack. Modeling small-molecule release from PLG microspheres: Effects of polymer degradation and nonuniform drug distribution. *Journal of Controlled Release*, 103:149–158, 2005.

[202] Yusuke Tanetsugu, Tatsuaki Tagami, Takayuki Terukina, Takaya Ogawa, Masato Ohta, and Tetsuya Ozeki. Development of a sustainable release system for a ranibizumab biosimilar using poly(lactic-co-glycolic acid) biodegradable polymer-based microparticles as a platform. *Biological and Pharmaceutical Bulletin*, 40:145–150, 2017.

[203] Nazila Kamaly, Basit Yameen, Jun Wu, and Omid C. Farokhzad. Degradable controlled-release polymers and polymeric nanoparticles: Mechanisms of controlling drug release. *Chemical Reviews*, 116:2602–2663, 2 2016.

[204] Susanne Fredenberg, Marie Wahlgren, Mats Reslow, and Anders Axelsson. The mechanisms of drug release in poly(lactic-co-glycolic acid)-based drug delivery systems - A review. *International Journal of Pharmaceutics*, 415:34–52, 2011.

[205] Daniel J Hines and David L Kaplan. Poly (lactic-co-glycolic) acid− controlled-release systems: experimental and modeling insights. *Critical Reviews™ in Therapeutic Drug Carrier Systems*, 30, 2013.

[206] James N. BeMiller. *An Introduction to Pectins: Structure and Properties*, chapter 1, pages 2–12.

[207] Stan Lagergren. *Zur theorie der sogenannten adsorption geloster stoffe*. Kungliga Svenska Vetenskapsakademiens Handlingar, 1898.

[208] Yuh-Shan Ho and Gordon McKay. Pseudo-second order model for sorption processes. *Process biochemistry*, 34:451–465, 1999.

[209] Walter J. Weber Jr. and Morris J. Carrell. Kinetics of Adsorption on Carbon from Solution. *Journal of the Sanitary Engineering Division*, 89:31–59, 4 1963.

[210] Thomas W. Weber and Ranjit K. Chakravorti. Pore and solid diffusion models for fixed-bed adsorbers. *AIChE Journal*, 20:228–238, 3 1974.

[211] Robert A. Latour. The Langmuir isotherm: A commonly applied but misleading approach for the analysis of protein adsorption behavior. *Journal of Biomedical Materials Research - Part A*, 103:949–958, 3 2015.

[212] F. Haghseresht and G. Q. Lu. Adsorption characteristics of phenolic compounds onto coal-reject-derived adsorbents. *Energy and Fuels*, 12:1100–1107, 11 1998.

[213] Mirghasem Hosseini, Stijn F.L. Mertens, Mohammed Ghorbani, and Mohammed R. Arshadi. Asymmetrical Schiff bases as inhibitors of mild steel corrosion in sulphuric acid media. *Materials Chemistry and Physics*, 78:800–808, 2003.

[214] Sylvia Lucas. The Pharmacology of Indomethacin. *Headache*, 56:436–446, 2 2016.

[215] Jacob Bouman, Peter Belton, Paul Venema, Erik Van Der Linden, Renko De Vries, and Sheng Qi. Controlled Release from Zein Matrices: Interplay of Drug Hydrophobicity and pH. *Pharmaceutical Research*, 33:673–685, 2016.

[216] Suvakanta Dash, Padala Narasimha Murthy, Lilakanta Nath, and Prasanta Chowdhury. Kinetic modeling on drug release from controlled drug delivery systems. *Acta Poloniae Pharmaceutica - Drug Research*, 67:217–223, 2010.

[217] Himankar Baishya. Application of Mathematical Models in Drug Release Kinetics of Carbidopa and Levodopa ER Tablets. *Journal of Developing Drugs*, 06:1–8, 2017.

[218] Juergen Siepmann and Nicholas A Peppas. Higuchi equation: Derivation, applications, use and misuse. *International journal of pharmaceutics*, 418:6–12, 2011.

[219] M Padmaa Paarakh, Preethy Ani Jose, CM Setty, and G. V. Peterchristoper. Release kinetics–concepts and applications. *International Journal of Pharmacy Research & Technology*, 8:12–20, 2018.

List of publications

Peer-review papers:

1. K. L. A. Cao, S. Taniguchi, **T. T. Nguyen**, A. F. Arif, F. Iskandar, T. Ogi*, Precisely Tailored Synthesis of Hexagonal Hollow Silica Plate Particles and their Polymer Nanocomposite Films with Low Refractive Index, *Journal of Colloid and Interface Science*, 571, 378-386, (2020). DOI: 10.1016/j.jcis.2020.03.064
2. A. M. Rahmatika, Y. Toyoda, **T. T. Nguyen**, Y. Goi, T. Kitamura, Y. Morita, K. Kume, T. Ogi*, Cellulose Nanofiber and Magnetic Nanoparticles as Building Blocks Constructing Biomass-based Porous Structured Particles and their Protein Adsorption Performance, *ACS Sustainable Chemistry & Engineering*, 8 (50) 18686-18695, (2020). DOI: 10.1021/acssuschemeng.0c07542
3. **T. T. Nguyen**, A. M. Rahmatika, M. Miyauchi, K. L. A. Cao, T. Ogi*, Synthesis of High Specific Surface Area Macroporous Pectin Particles by a Template-Assisted Spray Drying, *Langmuir*, 37 (14) 4256-4266, (2021). DOI: 10.1021/acs.langmuir.1c00232
4. **T. T. Nguyen**, M. Miyauchi, A. M. Rahmatika, K. L. A. Cao, E. Tanabe, T. Ogi*, Enhanced Protein Adsorption Capacity of Macroporous Pectin Particles with High Specific Surface Area and an Interconnected Pore Network, *ACS Applied Materials & Interfaces*, 14 (12) 14435-14446, (2022). DOI: 10.1021/acsami.1c22307
5. A. M. Rahmatika, Y. Toyoda, **T. T. Nguyen**, K. L. A. Cao, T. Hirano, T. Kitamura, Y. Goi, Y. Morita, T. Ogi*, Effects of Solvent Polarity on Nanostructure Formation of Spray-Dried TEMPO-Oxidized Cellulose Nanofiber Particles, *ACS Applied Polymer Materials*, 4 (9) 6700–6709, (2022) (Ac2022/8/4, Pb2022/8/17), DOI: 10.1021/acsapm.2c01063

6. **T. T. Nguyen**, Y. Toyoda, N. S. N. S. Bahri, A. M. Rahmatika, K. L. A. Cao, T. Hirano, K. Takahashi, Y. Goi, Y. Morita, M. Watanabe, and T. Ogi*, Tuning of Water Resistance and Protein Adsorption Capacity of Porous Cellulose Nanofiber Particles Prepared by Spray Drying with Cross-Linking Reaction, *Journal of Colloid and Interface Science*, 630 134-143 (2023). DOI: 10.1016/j.jcis.2022.10.078

7. **T. T. Nguyen**, N. S. N. S. Bahri, A. M. Rahmatika, K. L. A. Cao, T. Hirano, T. Ogi*, Rapid Indomethacin Release from Porous Pectin Particles as a Colon Targeted Drug Delivery System, *ACS Applied Bio Materials*, 6 (7) 2725-2737 (2023). DOI:10.1021/acsabm.3c00218

8. N. S. N. S. Bahri, **T. T. Nguyen**, T. Hirano, K. Matsumoto, M. Watanabe, Y. Morita, T. Ogi*, Enhancing water stability of nanostructured cellulose nanofiber particle through the application of oxazoline cross-linker, *Advanced Powder Technology*, 34 (12) 104241 (2023), DOI: 10.1016/j.apt.2023.104241

9. N. S. N. S. Bahri, **T. T. Nguyen**, K. Matsumoto, M. Watanabe, Y. Morita, E. L. Septiani, K. L. A. Cao, T. Hirano, T. Ogi*, Controlling the Magnetic Responsiveness of Cellulose Nanofiber Particles Embedded with Iron Oxide Nanoparticles, *ACS Applied Bio Materials*, 7 (5) 3227–3237 (2024), DOI: 10.1021/acsabm.4c00213

10. **T. T. Nguyen**, T. Hirano, R. N. Chamida, E. L. Septiani, N. T. Nguyen, T. Ogi*, Porous Pectin Particle Formation Utilizing Spray Drying with a Three-Fluid Nozzle, *Powder Technology*, 440, 119782 (2024), DOI: 10.1016/j.powtec.2024.119782